



University of Zagreb  
Faculty of Science  
Department of Physics

Marta Fatović

# **VARIABLE SOURCES IN LARGE OPTICAL SKY SURVEYS**

DOCTORAL DISSERTATION

Zagreb, 2024



University of Zagreb  
Faculty of Science  
Department of Physics

Marta Fatović

# **Variable sources in large optical sky surveys**

DOCTORAL THESIS

Supervisor:  
dr. sc. Lovro Palaversa

Zagreb, 2024



Sveučilište u Zagrebu  
Prirodoslovno-matematički fakultet  
Fizički odsjek

Marta Fatović

**Promjenjivi izvori u velikim optičkim  
pregledima neba**

DOKTORSKI RAD

Mentor:  
dr. sc. Lovro Palaversa

Zagreb, 2024

# Supervisor information

Dr. Lovro Palaversa began his scientific career at the Astronomical Observatory of the University of Geneva (Switzerland) as a Ph.D. student under the supervision of Dr. Laurent Eyer. During his doctoral studies, he focused on the discovery and classification of various types of variable and transient astrophysical sources, as well as observational astrophysics (photometry and spectroscopy). After completing his Ph.D., he moved on to a postdoctoral position at the Institute of Astronomy at the University of Cambridge (UK), where, under the guidance of Dr. Dafydd W. Evans, he worked on topics related to the photometric calibration of the European Space Agency's Gaia mission. In early 2019, he joined the Ruđer Bošković Institute and founded a group focusing on research related to large sky surveys in the optical part of the spectrum, with a particular emphasis on variable astrophysical objects. He is an active member of the Gaia Data Processing and Analysis Consortium and the Vera C. Rubin Legacy Survey of Space and Time Science Collaborations.



# Acknowledgements

Thank you to my two biggest supporters: my mom Rajka, and my sister Ivona. You have stood by me every step of this crazy journey, always providing everything I needed. I could not have made it without your love and support.

To my aunts, uncle and cousins, thank you for the family gossip and bursts of laughter that kept me optimistic and reminded me of what truly matters in life.

Dear Luce and Mečka, your humor and positive outlook on life helped me see this through to the end. I am so lucky for having you in my life. Thank you to Tome, who, after 23 years, remains my true friend and someone I could always count on. Thanks to Jure and Vana for all the interesting discussions and great advice. And thanks to the choir "Zračni puhovi" for reminding me to find the positive in every situation.

To Boki and Ana Š., our Skype calls always made me laugh, even during the toughest times. I will always cherish our coffee dates, whether with cats, on an airplane, or in a conference room.

I am very grateful to my supervisor, Dr. Lovro Palaversa, for making this thesis possible. I am also thankful to Dr. Vibor Jelić and the entire Laboratory for astroparticle physics and astrophysics at RBI for their support and engaging lunchtime discussions on animal topics. A big thank you goes to Alex for being my office therapist during tough times. Special thanks to Lana, Ana, and Iva for being wonderful friends and colleagues.

I am deeply grateful to Dr. Dragana Ilić and Dr. Anđelka Kovačević for reminding me why I chose to become a scientist when I needed it most.

A big thank you to Mr. Marko Hum for his patience and support. He is truly a superhero to all the doctoral students.

Above all, I want to thank my grandmother (mojoj babi), who never quite understood what I do but always believed in me nonetheless. Thank you for always looking forward to my video calls. I will miss you forever. This thesis is dedicated to you.

# Abstract

This thesis studies periodic variability in large optical sky surveys, focusing on long-period variable sources. A primary challenge in studying these objects is accurately determining their periods. The first part of this thesis addresses this by introducing a set of filters to reliably identify periods of sources in the SDSS S82, which were previously classified as non-variable. Five quasars with plausible periodic variability were identified by applying several criteria to the light curves. These criteria included requiring at least 25 data points, matching periods in the SDSS *gri* filters within 0.1%, and ensuring good agreement with a simple sinusoidal model. Potential aliases were filtered out by requiring distinct periods and calculated uncertainties that were not multiples of one year. Additionally, Kuiper statistics were used to ensure no significant gaps or clustering of points in each phase light curve.

In the second part of this thesis, the focus is on one of the previously detected quasars with the shortest period of 278 days. This quasar is analyzed using new observations of MgII lines and archived SDSS spectra, providing three epochs of MgII observations. The key findings include the discovery that the newly observed MgII line exhibits a double-peaked profile that changes over time. By comparing synthetic magnitudes with photometric data as well as using the PoSKI model, which analyzes emission lines and light curves of candidate supermassive binary black holes (SMBBH), a correlation was found suggesting a closely orbiting SMBBH.

The latest release Gaia DR3, included light curves for all objects within a field centered on the Andromeda Galaxy. The final scientific part of this thesis focuses on identifying Mira stars in the M31 galaxy and determining their periods. For the first time, a period-luminosity (PL) relation for Mira variables in the M31 galaxy has been established using Gaia filters. This relation is compared with PL relations for multiple galaxies presented in other works, using 2MASS data. Although the method can be improved, the results are promising and lay the groundwork for future research utilizing Gaia's light curves for the entire sky.

Keywords: long-period variability, red giants, active galactic nuclei, supermassive binary black hole, quasar, light curve, MgII spectral line

# Prošireni sažetak

Periodički promjenjivi izvori su oni izvori čiji se sjaj mijenja u pravilnim vremenskim intervalima. Oni su znanstveno zanimljivi jer omogućuju procjenu udaljenosti do drugih galaksija. Za razliku od mjerenja ravn alom, ne možemo izravno mjeriti udaljenosti u svemiru. Stoga su astronomi razvili niz metoda poznatih kao kozmička ljestvica udaljenosti za njihovu procjenu. Jedna od ključnih metoda u astrofizici je korištenje period-sjaj (PL, od engl. period-luminosity) relacije za mjerenje udaljenosti zvijezda. Henrietta Swan Leavitt otkrila je ovu važnu vezu tijekom svog istraživanja, pronasavši blisku povezanost između sjaja promjenjivih zvijezda i logaritma njihovog perioda pulsacije (Leavitt, 1908; Leavitt & Pickering, 1912). Jednostavnije rečeno, zvijezde s dužim periodima pulsacije su sjajnije, što je i prikazano u PL relaciji:

$$M = a \cdot \log(P) + b. \quad (1)$$

Koncept se temelji na procjeni PL relacija za objekte s dobro poznatim udaljenostima, koje se zatim koriste za procjenu udaljenosti udaljenijih objekata.

Promjenjivi izvori obično se analiziraju pomoću krivulja sjaja (LC, od engl. light curve), koje prikazuju promjene toka ili magnitude izvora tijekom vremena, dok je za izvore s periodičnom varijabilnošću korisnije koristiti fazne krivulje sjaja (PLC, od engl. phased light curve), koje prikazuju promjene u odnosu na fazu, određenu jednadžbom:

$$\phi = \frac{t}{P} - \text{int}\left(\frac{t}{P}\right), \quad (2)$$

gdje  $t$  predstavlja vrijeme promatranja, a  $P$  period izvora.

Trenutno je pronađeno stotine vrsta i podvrsta promjenjivih zvijezda s raznolikim fizičkim i kemijskim svojstvima (Samus et al., 2017). Ova teza istražuje periodične promjene opažene u galaktičkim i vangalaktičkim izvorima koristeći postojeće optičke preglede neba. Glavni fokus je na dugoperiodičnoj promjenjivosti, posebno kod crvenih divova (RG, od engl. red giants) i periodički promjenjivih aktivnih galaktičkih jezgri (AGN, od engl. active galactic nuclei). Ove vrste izvora dosad su bile relativno slabo istražene zbog izazova povezanih s potrebnim

opažanjima. Međutim, nedavni tehnološki napreci u pregledima neba omogućili su učinkovitije proučavanje ovih dugoperiodičnih izvora, što je dovelo do povećanog interesa i istraživanja u ovom području.

## Crveni divovi

Kada zvijezde potroše svoje zalihe vodika i prestanu s fuzijom u jezgri, napuštaju glavni niz. One malih i srednjih mase tada se šire i hlade, postajući crveni divovi. Zvijezde asimptotskog divovskog ogranka (AGB, engl. Asymptotic Giant Branch) imaju jezgre bogate ugljikom i kisikom, dok helij i vodik sagorijevaju u okolnim ljuskama. Ova teza fokusira se na proučavanje crvenih divova, posebno Mira zvijezda koje karakteriziraju velike amplitude i dugi periodi.

## Aktivne galaktičke jezgre

Aktivne galaktičke jezgre (AGN) su iznimno sjajna područja u središtima određenih galaksija, napajana akrecijom materije na supermasivnu crnu rupu. AGN-ovi se ističu svojom zračenjem u različitim područjima elektromagnetskog spektra uključujući radio, optičke, ultraljubičaste, rendgenske i gama zrake.

AGN-ovi se sastoje od nekoliko komponenti: supermasivne crne rupe u sredini, akrecijskog diska, brzo rotirajućih oblaka plina koji stvaraju široke emisijske linije (BLR, od engl. broad line region), sporije rotirajućih oblaka plina koji stvaraju uske emisijske linije (NLR, od engl. narrow line region), torusa prašine te ponekad relativističkih mlazova (engl. jet) čestica.

Svi AGN-ovi pokazuju promjenjivo ponašanje koje je uglavnom stohastičke prirode, što znači da pokazuju nepredvidljive promjene u emisiji na različitim valnim duljinama. Osim stohastičkih promjena, neki AGN-ovi pokazuju periodično ponašanje. Objašnjenja za periodično ponašanje uključuju astrofizičke fenomene poput precesije radio mlazova, nagnutih ili deformiranih akrecijskih diskova, događaja plimnog raspada zvijezda te dvojnih sustava supermasivnih crnih rupa (SMBBH, od engl. supermassive binary black hole). Tehnološki napredak značajno je poboljšao razumijevanje ovog ponašanja, što ga čini jednim od glavnih tema ove teze.

## Otkrivanje dugoperiodične promjenjivosti u SDSS Stripe 82 katalogu standardnih zvijezda

Budući da su promjenjivi izvori od velike važnosti za astronomiju, ključno je pouzdano odrediti njihove periode. Prva od tri znanstvene teme ove teze usmjerena je na rješavanje ovog problema

uvođenjem niza metoda filtriranja za prepoznavanje pravih kandidata za dugoperiodične izvore unutar uzorka za kojeg se smatralo da sadrži samo standardne zvijezde. Unatoč nepristranom pretraživanju, očekivalo se da će konačni uzorak uglavnom sadržavati izvore s dugim periodom i malim amplitudama.

Primarni fokus ovog rada bio je na osiguravanju čistoće konačnog uzorka, stavljajući ovaj aspekt ispred potpunosti. Kako bi se to postiglo, primijenjen je rigorozan pristup filtriranju, sastavljen od niza preciznih statističkih koraka.

## Metode

Prvotno je razmatran uzorak od 1 001 592 krivulje sjaja. Nakon filtriranja mjerenja s vjerojatno pogrešnom fotometrijom, odabran je podskup od 143 505 svjetlosnih krivulja s najmanje 25 epoha. Mjerenja su isključena ako je njihova SDSS *gri* magnituda bila izvan raspona od 11 do 23 mag, ako su imala nerealno male fotometrijske pogreške (manje od 0,0001 mag) ili ako su fotometrijske pogreške bile veće od 0,2 mag.

Za računanje perioda korištena je implementacija Lomb-Scargle periodograma iz *astropy* (vidi Poglavlje 3.1.1). Metoda *autopower* određivala je razmak mreže (engl. grid), smanjujući računalnu složenost. Ulazne frekvencije bile su  $f_{min} = 1/600$  dana<sup>-1</sup> i  $f_{max} = 1/2$  dana<sup>-1</sup>. Periodogrami su računati za *gri* SDSS filtre s dodatnom sistemskom fotometrijskom pogreškom od 0,01 mag radi sprječavanja nerealno malih pogrešaka. Zadržani su periodi s tri najistaknutija vrha u periodogramu, omogućujući bolju procjenu aliasinga. Od devet izračunatih perioda po izvoru, izvori s najmanje jednim zajedničkim periodom u sva tri *gri* filtra (tolerancija 0,1%) odabrani su kao uvjerljivo periodični. To je rezultiralo s 1,078 izvora i 2,135 odgovarajućih perioda.

Kako bi se procijenilo slaganje podataka s jednostavnim sinusoidalnim modelom, primijenjena je  $\chi^2$  metoda. Ovim filtriranjem dobivena su 342 izvora s 601 odgovarajućim periodom.

U uzorku od 342 izvora s 601 periodom, uočeni su brojni ponavljajući periodi koji su isključeni ako su bili unutar raspona od 0,1 dan, jer se vjerojatno radi o aliasima. Za detaljniju analizu dugih perioda zadržani su samo objekti s periodima dužim od 100 dana, što je ostavilo 45 jedinstvenih objekata s 58 pripadajućih perioda.

Glavni cilj ovog rada bio je dobiti čisti uzorak izvora s dugim periodima, što je zahtijevalo da fazna krivulja sjaja bude bez praznina i grupiranja podataka. Svaki potencijalni kandidat morao je imati ravnomjerno raspoređena opažanja u fazi, a krivulje sjaja s grupiranim opažanjima bile su označene kao lažno pozitivne i isključene iz daljnje analize. Primjenom Kuiperove statistike, za daljnju analizu izdvojeno je 28 izvora s 33 odgovarajuća perioda.

Periodi su morali biti usklađeni s onima generiranim MC metodom objašnjenom u Sekciji 3.1.3 unutar pripadajućeg raspona ( $|P - P_{\text{gatspy}}| < \sigma_P$ ). To je uzorak suzilo na 9 izvora s ukupno 10 različitih perioda.

Kao posljednji filtar, ova jednačba je korištena je za detekciju perioda koji bi mogli biti uzrokovani s jednogodišnjim aliasima:

$$P_a = 365 \pm \frac{k}{n} \cdot 365; \quad k = 1, 2; \quad n = 1, 2, 3, 4, 5. \quad (3)$$

Ako je izračunati period  $P$  bio unutar raspona  $P \pm \sigma_P$  (365 dana), smatrao se aliasom vezanim za jednogodišnji ciklus. Primjena ovog kriterija filtriranja smanjila je uzorak na 5 izvora sa 6 pripadajućih perioda.

Dodatne provjere su provedene kako bi se isključila mogućnost očitih pogrešaka. Analizom SDSS slika za pet identificiranih izvora potvrđeno je da niti jedan kandidat nije bio podložan efektima spajanja (engl. blending). Istraživanje je prošireno na baze podataka drugih pregleda, uključujući ZTF DR11 i PS1, kako bi se analizirale krivulje sjaja u različitim vremenima. Ova metoda potvrdila je promjenjivost u barem jednom filtru za svaki dodatni pregled, što je značajno smanjilo mogućnost da su originalni SDSS podaci bili pogrešni ili da su otkrivene periodičke promjene rezultat slučajnih fluktuacija.

## Rezultati

Kako bi se bolje razumjele karakteristike pet konačnih izvora, provedena je pretraga njihovih spektara u SDSS DR16 online bazi podataka. Otkriveno je da svih pet kandidata ima spektre koji su u skladu sa spektrom kvazara, a ne zvijezda kako je očekivano.

Značajne nepouzdanosti u ZTF fotometriji onemogućuju donošenje konačnih zaključaka za izvore s ID-ovima 10 i 25. Međutim, PS1 fotometrija potvrđuje promjenjivost u barem jednom filtru. Izvor ID 10, prikazan na Slici 4.5, ima najmanju amplitudu ( $A \sim 0.2$  mag) među svim konačnim kandidatima. Izvor ID 25, prikazan na Slici 4.8, ima dva odgovarajuća perioda koja zadovoljavaju kriterije odabira. Budući da ti periodi padaju unutar raspona navedenog u tablici 4.3 ( $|P_1 - P_2| < \sigma_P$ ), razumno je zaključiti da se radi o istom periodu od 300 dana.

Izvori ID 20 i 27, prikazani na Slici 4.6 i Slici 4.9, pokazuju čvrstu potvrdu periodičnosti potkrijepljenu podacima iz ZTF i PS1. Ove slike također pokazuju da ZTF amplitude ne isključuju SDSS model kao netočan. Posebno zanimljiv kvazar u ovom uzorku je ID 21 (Slika 4.7), koji ima period od  $P = 278$  dana. Osim optičke promjenjivosti otkrivene u ovom radu, ovaj izvor također ima Chandra X-ray potvrdu promjenjivosti (Evans et al., 2010). Za ovaj izvor provedena je dodatna analiza njegove periodičnosti korištenjem 2D hibridnog modela opisanog

u odjeljku 3.1.2. Primjenom 2D hibridne metode dobiven je period od  $278.36_{-25.21}^{+57.34}$  dana sa značajnošću iznad 99%.

## Zaključak poglavlja

Razumijevanje uzroka periodičnosti ovih kandidata nije moguće bez dodatnih podataka. Zato je izdvojen jedan kvazar (ID=21) s periodom od 278 dana, čija periodičnost nije isključena pomoću ZTF i PS1, a pokazivao je i promjenjivost u X-ray dijelu elektromagnetskog spektra. Kako bi se dodatno istražila priroda ove periodičnosti, dobiveni su novi spektri ovog izvora kroz dva nova opažanja s Gemini GMOS-S i Magellan LDSS3. Ovaj dio istraživanja detaljno je opisan u sljedećem znanstvenom dijelu teze.

## Složena vremenska evolucija MgII linije u SDSS J2320+0024: Tragovi za dvojni sustav supermasivnih crnih rupa na udaljenosti manjoj od jednog parseka?

U prethodnom poglavlju predstavljeno je pet kandidata za kvazare s periodičnom promjenjivošću. Različita moguća objašnjenja za ovaj fenomen razmotrena su u odjeljku 1.5.2, a kandidat s najkraćim periodom od 278 dana odabran je za daljnje proučavanje kao prototip.

Analiza arhivskog SDSS spektra otkrila je složen, blago asimetričan profil široke MgII emisijske linije. Spektroskopsko praćenje provedeno je kako bi se zabilježila MgII emisijska linija pri maksimalnom sjaju, s ciljem detekcije mogućeg dvostrukog profila. Zbog slabosti izvora, korišteni su teleskopi klase od 8 metara za dobivanje visokokvalitetnih spektara. Važno je napomenuti da ovaj izvor nema odgovarajući radio signal te da nije detektiran u raznim radio pregledima neba, uključujući VLA FIRST Survey na 1.4 GHz, AT20G Survey na 20 GHz i VLA Sky Survey.

## Analiza i rezultati

Novi Gemini i Magellan spektri detaljnije su opisani u Odjeljku 2.2.2. Korištenjem reduciranih i kalibriranih podataka, kontinuum i Fe II emisijske linije su oduzeti pomoću Python alata za analizu AGN spektra (Fantasy, Ilić et al., 2023), kao u Popović et al. (2019). Spektar je pomaknut u vlastiti referentni sustav i analiziran u prostoru brzina, kako je opisano u Odjeljcima 3.3.2 i 3.3.3.

Profil MgII linije analiziran je pomoću niza lako mjerljivih veličina za opisivanje njegovih složenih promjena, kako je navedeno u Lewis et al. (2010). Razmak između dvaju uočenih vrhova promijenio se s  $1661 \text{ km s}^{-1}$  na  $1328 \text{ km s}^{-1}$ , a omjer toka crvenog i plavog vrha s  $0,893$  na  $0,973$  unutar mjesec dana između promatranja Gemini i Magellan. SDSS profil prikazuje jedan vrh koji odgovara položaju crvenog vrha u ostalim profilima. Također, postoji približno  $1000 \text{ km s}^{-1}$  razlika u punoj širini na pola maksimuma (FWHM, engl. full width half maximum), punoj širini na četvrtini maksimuma (FWQM, engl. full width quarter maximum) i iskrivljenosti/asimetriji između SDSS profila i novih spektara. Zanimljivo je da se iskrivljenost profila linije značajno promijenila za oko  $500 \text{ km s}^{-1}$  između Magellan i Gemini promatranja. Crveni vrh ostaje stabilan dok se plavi vrh pomiče, mijenjajući oblik MgII linijskog profila. Rezultati mjerenja vrhova navedeni su u Tablici 5.1.

Prva procjena ukupne mase sustava izračunata je iz širine MgII linije i kontinuuma na  $3000 \text{ \AA}$ , prema postupku opisanom u Odjeljku 3.3.4. Procijenjena masa sustava za sva tri spektra je  $M_{\bullet\bullet} \sim 10^9 M_{\odot}$ , što bi SDSS J2320+0024 činilo jednim od najmasivnijih poznatih SMBBH sustava s periodom manjim od godinu dana.

Razmak  $a$  crnih rupa u mogućem SMBBH sustavu izračunat je prema Liu et al. (2019):  $\frac{a^3}{t_{\text{orb}}^2} = \frac{GM}{4\pi^2}$ , gdje  $t_{\text{orb}} = \frac{P_{\text{obs}}}{1+z}$  predstavlja orbitalni period u vlastitom referentnom sustavu. Dobiiveni su razmaci na skali miliparseka. Formalne pogreške dobivene su kroz neovisna mjerenja kontinuuma.

Paket `rubin_sim` (Yoachim et al., 2023) korišten je za izračunavanje sintetičkih SDSS  $r$  magnituda iz Gemini, Magellan i SDSS spektra. Krivulja sjaja na slici 5.2 prikazuje kombinaciju promatrane i sintetičke fotometriju, postavljenu na sinusoidalni model. Sintetičke magnitude novih opažanja (Gemini i Magellan) su unutar 95% intervala pouzdanosti, ukazujući na periodičnu promjenjivost kvazara, dok SDSS sintetička magnituda pokazuje veće odstupanje. Do tog odstupanja je vjerojatno došlo zbog kalibracijske pogreške ili bljeska (engl. flare) AGN-a tijekom promatranja.

Na kraju, s obzirom na dramatičnu promjenu u profilu emisijske linije koja bi mogla ukazivati na složenu dinamiku unutar sustava, provedeno je modeliranje MgII linije u kontekstu SMBBH sustava koristeći model Popović, Simić, Kovačević, Ilić (PoSKI, Popović et al., 2021) opisan u Odjeljku 3.3.5. Na slici 5.3 prikazan je profil široke linije MgII prema modelu (puna linija) za epohe SDSS, Gemini i Magellan. Parametri ograničeni opažanjima istraženi su, pri čemu je ukupna masa sustava procijenjena na  $\log(M) \sim 8.3 M_{\odot}$ , omjer masa na  $q = 0.1$ , a razmak na  $0.0025 \text{ pc}$ . Svaka od supermasivnih crnih rupa sadrži akrecijski disk, dok BLR posjeduje samo manje masivna komponenta. Akrecijski diskovi osvjetljavaju zajednički BLR (cBLR, engl. circumbinary BLR), stvarajući stalni crveni vrh iz cBLR-a i pomični plavi vrh



iz BLR-a manje crne rupe. Sofisticiranije modeliranje omogućit će spektar visoke rezolucije i visokog omjera signal-šum (S/N, engl. signal-to-noise).

## Zaključak poglavlja

Rezultati modeliranja i opažanja dali su dosljedne vrijednosti za mase i razmake dviju komponenti. Odabir SMBBH modela temelji se na tri faktora. Prvo, dvojni model mora točno predviđeti promatrane značajke poput orbitalnih karakteristika i ukupne mase, nadalje model treba biti u skladu s različitim vrstama podataka uključujući fotometriju i spektroskopiju i konačno, statistička značajnost može favorizirati dvojni model. Za procjenu alternativnog objašnjenja opaženog ponašanja s jednom crnom rupom treba u analizu uključiti druge emisijske linije.

Ovaj slučaj se ističe zbog izraženih promjena u profilu MgII linije koje su također povezane s promjenjivosti predviđenoj krivuljom sjaja. Ako se potvrdi spektroskopijom drugih emisijskih linija, ovi rezultati bi mogli nagovijestiti potencijalne rezultate nadolazećih velikih optičkih pregleda, poput Legacy Survey in Space and Time (LSST) iz Vera Rubin Opservatorija. Očekuje se da će budući spektroskopski pregledi otkriti i analizirati takve masivne dvojne kvazare, što će biti ključno za određivanje učestalosti spajanja galaksija. Daljnja praćenja s velikim teleskopima i instrumentima visoke preciznosti su nužna za potvrdu prave prirode ovog izvora.

## Analiza perioda crvenih divova u galaksiji Andromeda

Mira zvijezde, podvrsta dugoperiodičnih izvora (LPV, engl. long period variables), nastaju tijekom evolucije zvijezda male i srednje mase. Njihove karakteristike uključujući sjaj, velike amplitude i periode od 10 do 1000 dana, čine ih lako uočljivima pa je zbog toga njihova PL relacija postala ključni alat za istraživanje LPV-a i njihove evolucije tijekom AGB faze.

Istraživanja Mira zvijezda u Magellanovim oblacima, koristeći podatke iz OGLE pregleda neba, pružila su značajne uvide u njihova svojstva i ponašanja (e.g., Soszyński et al., 2009b; Groenewegen, M. A. T. & Blommaert, J. A. D. L., 2005; Bhardwaj et al., 2019). Ova istraživanja uspostavila su pouzdane PL relacije koje su ključne za razumijevanje evolucije zvijezda i mjerenje udaljenosti u svemiru. Međutim, Mira zvijezde u galaksiji M31 i kalibracija njihovih PL relacija pomoću Gaia filtara ostaju neistražene.

Ovo poglavlje usredotočuje se na proučavanje dugoperiodičnog ponašanja Mira zvijezda promatranih u GAPS (Gaia Andromeda Photometric Surey) polju. Glavni ciljevi uključuju izoliranje Mira zvijezda, određivanje njihovih perioda i kalibriranje PL relacije korištenjem 2MASS i Gaia fotometrijskih podataka, te usporedbe s prethodnim istraživanjima.

## Podaci i metode

Podaci korišteni u ovom istraživanju opisani su u sekcijama 2.1.4 i 2.1.5. Prvi korak bio je identificirati galaksiju M31 koristeći Gaia GAPS podatke. Svi izvori s paralaksom manjom od 0.5 mas isključeni su kao pripadnici Mliječne staze. Preostali izvori morali su imati amplitudu promjenjivosti veću od 0.8 mag u G filtru, čime su uglavnom isključene ne-Mira zvijezde. Na slici 6.1 crvene točke predstavljaju izabrane izvore, sivi krug označava centar M31, a narančaste točke označavaju 400 najbližih izvora centru M31. Ovaj uzorak korišten je za izračun perioda i identificiranje potencijalnih Mira zvijezda.

Wesenheit magnituda za 2MASS i Gaia podatke izračunate su prema sljedećim formulama:

$$W_{J,K} = K - 0.686(J - K), \quad (4)$$

$$W_G = G - 1.9(BP - RP), \quad (5)$$

$$W_{BP,RP} = RP - 1.3(BP - RP). \quad (6)$$

Za izračun perioda korištena je *astropyjeva* implementacija Lomb-Scargle periodograma, koristeći samo G filter za izvore s više od 25 opažanja. Raspon perioda je definiran od 100 dana do promatranog vremenskog raspona, s razmakom mreže (engl. grid) od 10 minuta. Proces je smanjio početni broj od 400 kandidata na 209. Kako bi se eliminirali lažno-periodički izvori, oni sa sličnim periodima (unutar 0.5 dana) su isključeni, ostavljajući uzorak od 101 izvora. Konačna provjera ispravnosti perioda i tipa promjenjivosti obavljena je vizualnom procjenom krivulja sjaja, čime je uzorak smanjen na 25 izvora.

## Rezultati i diskusija

Uzorak od 25 kandidata uspoređen je s Gaia arhivom, što je rezultiralo s 8 podudaranja. Cilj je bio utvrditi koliko je kandidata već identificirano kao dugoperiodične zvijezde i usporediti periode s Gaia periodima. Istraživanje predstavljeno u ovoj tezi identificiralo je 17 novih dugoperiodičnih izvora, vjerojatno tipa Mira.

Sljedeći cilj bio je odrediti položaj tih izvora na PL relaciji. Svi izvori uspoređeni su s OGLE III Mira katalogom na slici 6.4, pokazavši da su 23 od 25 izvora vjerojatno O-bogate Mire, dok su preostala 2 C-bogate Mire. Konačni uzorak za ovo istraživanje sastoji se od 23 O-bogate Mire.

Od konačnih 23, samo 19 je detektirano u 2MASS 6X katalogu. Njihova PL relacija prikazana je na slici 6.5 i uspoređena s rezultatima iz Lebzelter, T. et al. (2019). Uzorak obuhvaća visoko- i srednjemasivne O-AGB zvijezde.

Sve PL relacije prikazane su na slici 6.6 i relativno su konzistentne. Opaženo je i blago neslaganje u odsječku na  $y$ -osi. Do takve razlike može doći zbog premalenog uzorka i identifikacije samo sjajnijih Mira zvijezda s dužim periodima u Gaia opažanjima, tj. promatranjem samo gornjeg dijela PL relacije.

## Zaključak poglavlja

Ovaj rad proučava dugoperiodično ponašanje Mira zvijezda opaženih u GAPS polju. Glavni ciljevi bili su izolirati Mira zvijezde, odrediti njihove periode i procijeniti njihovu usklađenost s PL relacijom koristeći 2MASS i po prvi put Gaia fotometrijske podatke.

Dobivene P-L relacije su:

$$J = (-3.3 \pm 0.6) + (-7.4 \pm 0.3)(\log_{10}(P) - 2.3), \quad (7)$$

$$H = (-3.7 \pm 0.5) + (-8.1 \pm 0.3)(\log_{10}(P) - 2.3), \quad (8)$$

$$K = (-4.2 \pm 0.3) + (-8.3 \pm 0.3)(\log_{10}(P) - 2.3), \quad (9)$$

$$W_{BP,RP} = (-4.5 \pm 0.6) + (-8.1 \pm 0.3)(\log_{10}(P) - 2.3), \quad (10)$$

$$W_{J,K} = (-4.7 \pm 0.6) + (-9.0 \pm 0.3)(\log_{10}(P) - 2.3). \quad (11)$$

Iako postoji prostor za poboljšanje analize koja se oslanja na vizualni pregled krivulja sjaja, rezultati su usporedivi s prethodnim radovima. Glavna motivacija za ovo istraživanje bila je testiranje GAPS podataka, s obzirom na to da će Gaia uskoro objaviti četvrto izdanje podataka (DR4), pružajući krivulje sjaja za cijelo nebo. Objavom istih za GAPS polje, dobiven je uvid u buduće mogućnosti s nadolazećim Gaia podacima.

## Sažetak teze i buduća istraživanja

Ova disertacija istražuje dugoperiodičnu promjenjivost u velikim optičkim pregledima neba. Periodički promjenjivi izvori ključni su za procjenu udaljenosti u svemiru. Osim toga, promatranje periodične promjenjivosti u AGN-ovima može pružiti uvid u mogućnost sustava dvojnih crnih rupa, čime se postavlja temelj za proučavanje gravitacijskih valova.

Glavni izazov u proučavanju promjenjivih izvora je točno određivanje njihovih perioda. U poglavlju 4 uvedene su metode filtracije za pouzdano određivanje perioda objekata prethodno klasificiranih kao nepromjenjivi. Identificirano je pet kvazara s mogućom periodičkom promjenjivošću u SDSS *ugriz* filtrima, pri čemu je kvazar s najkraćim periodom odabran za daljnje istraživanje. Buduća istraživanja će imati koristi od nadolazećih osjetljivih pregleda neba, po-

put Rubin Observatory Legacy Survey of Space and Time, koji će biti učinkovitiji u otkrivanju periodične promjenjivosti.

U poglavlju 5 analiziran je jedan od pet identificiranih kvazara koristeći nove MgII linije i arhivirane SDSS spektre, pružajući tri epohe MgII opažanja. Primjenom PoSKI modela utvrđena je povezanost između opaženog ponašanja i modeliranog sustava, sugerirajući prisutnost SMBBH u bliskoj orbiti. Za potvrdu SMBBH sustava potrebna su opsežna promatranja, uključujući daljnje spektroskopsko praćenje i fotometrijska opažanja. Promatranja radio emisije mogla bi pružiti jedinstvenu dijagnostiku okruženja SMBBH sustava.

Gaia satelit započeo je svoja znanstvena opažanja 2014. godine, značajna za proučavanje promjenjivih izvora jer Gaia mapira cijelo nebo. U poglavlju 6 identificirane su Mira zvijezde u M31 galaksiji i određeni su njihovi periodi. Po prvi put uspostavljena je PL relacija za Mire u M31 galaksiji koristeći Gaia filtre. Analiza periodičnosti Mira u M31 može se poboljšati uključivanjem čimbenika poput gibanja zvijezda u Andromedi, boje i svih triju Gaia filtera pri izračunu perioda. Gaia DR4 pružit će podatke o krivuljama sjaja za sve opažene izvore, omogućujući primjenu ove metode na druge galaksije.

**Ključne riječi:** dugoperiodična varijabilnost, crveni divovi, aktivne galaktičke jezgre, supermasivna binarna crna rupa, kvazar, krivulja sjaja, MgII spektralna linija

# Contents

<b>1</b>	<b>Introduction</b>	<b>1</b>
1.1	Variable sources . . . . .	1
1.1.1	Variability tree . . . . .	3
1.1.2	Why are periodic sources important? . . . . .	4
1.1.3	Intrinsically periodically variable stars . . . . .	9
1.2	Red Giants . . . . .	11
1.2.1	Summary of the low-mass star evolution after the main sequence . . . . .	11
1.2.2	Pulsation of Mira stars . . . . .	12
1.2.3	Red Giants as distance estimators . . . . .	14
1.3	Active Galactic Nuclei . . . . .	16
1.3.1	AGN components . . . . .	16
1.3.2	Types of AGNs . . . . .	17
1.3.3	The Unified Model of AGNs . . . . .	18
1.4	Impact of SMBH on Spectral Line Profiles . . . . .	19
1.4.1	SMBH Mass determination using broad lines . . . . .	19
1.5	Variability in AGNs . . . . .	22
1.5.1	Stochastic variability . . . . .	22
1.5.2	Periodic variability . . . . .	22
1.6	Multi-wavelength Observations in Astronomy . . . . .	24
1.6.1	Observations of Variable Stars . . . . .	24
1.6.2	Observations of Active Galactic Nuclei (AGNs) . . . . .	25
1.7	Thesis outline . . . . .	26
<b>2</b>	<b>Data</b>	<b>28</b>
2.1	Photometry . . . . .	28
2.1.1	SDSS Stripe 82 photometry . . . . .	32
2.1.2	ZTF photometry . . . . .	33
2.1.3	PS1 photometry . . . . .	33
2.1.4	Gaia photometry . . . . .	34
2.1.5	2MASS photometry . . . . .	34
2.2	Spectroscopy . . . . .	36
2.2.1	Spectroscopic observations . . . . .	36
2.2.2	Gemini and Magellan observations . . . . .	38
2.2.3	SDSS spectroscopy - eBOSS . . . . .	40

<b>3</b>	<b>Methods</b>	<b>41</b>
3.1	Period determination . . . . .	41
3.1.1	Lomb - Scargle periodogram . . . . .	41
3.1.2	2D Hybrid method . . . . .	43
3.1.3	Monte - Carlo simulations . . . . .	44
3.2	Statistical methods of filtering calculated periods . . . . .	45
3.2.1	$\chi^2$ and periodogram relation . . . . .	45
3.2.2	Phase distribution analysis and Kuiper statistics . . . . .	45
3.3	Analysis of the quasar spectra . . . . .	47
3.3.1	Data reduction and calibration . . . . .	47
3.3.2	Shifting Quasar Spectra to the Rest Frame . . . . .	48
3.3.3	Spectral Analysis in Velocity Space . . . . .	48
3.3.4	Mass estimation . . . . .	49
3.3.5	PoSki model . . . . .	49
3.3.6	Calculation of the synthetic magnitudes . . . . .	50
3.4	Calibration of Period-Luminosity relation . . . . .	51
<b>4</b>	<b>Detecting long - period variability in the SDSS Stripe 82 standards catalog</b>	<b>53</b>
4.1	Period calculation and filtering . . . . .	54
4.1.1	Number of data points . . . . .	54
4.1.2	Lomb-Scargle period agreement . . . . .	55
4.1.3	Agreement with the model . . . . .	55
4.1.4	Dealing with repeated periods and filtering out aliases . . . . .	55
4.1.5	Implementation of Kuiper metric . . . . .	57
4.1.6	Characterization of Sources . . . . .	57
4.1.7	Comparison with MC simulations . . . . .	59
4.1.8	Dealing with one-year period aliases . . . . .	59
4.1.9	Additional checks . . . . .	59
4.1.10	Summary of the filters used . . . . .	60
4.1.11	SDSS spectra of the final candidates . . . . .	61
4.2	Results . . . . .	62
4.2.1	Representative figures of final candidates . . . . .	62
4.2.2	Table of final candidates . . . . .	66
4.2.3	The results of Monte Carlo simulations . . . . .	68
4.3	Discussion . . . . .	69
4.4	Chapter summary and conclusions . . . . .	70
<b>5</b>	<b>Complex MgII Time Evolution in SDSS J2320+0024: Clues for a Subparsec Binary Supermassive Black Hole?</b>	<b>71</b>
5.1	Data and Analysis . . . . .	73
5.2	Results and Discussion . . . . .	74
5.2.1	PoSki model results . . . . .	77
5.3	Chapter summary and conclusions . . . . .	78

<b>6</b>	<b>Period analysis of Red Giant stars in Andromeda</b>	<b>80</b>
6.1	Data and Methods . . . . .	81
6.2	Results and discussion . . . . .	84
6.2.1	PL relation . . . . .	85
6.3	Chapter summary and conclusions . . . . .	91
<b>7</b>	<b>Thesis summary and outlook</b>	<b>92</b>
7.1	Summary of this Thesis . . . . .	92
7.2	Future work . . . . .	94
	<b>Appendix A Basic concepts</b>	<b>96</b>
	<b>References</b>	<b>98</b>

# List of Figures

1.1	Example of a light curve and a phased light curve of a variable star. . . . .	2
1.2	Variability tree. . . . .	3
1.3	An example of the cosmic distance ladder. . . . .	5
1.4	Parallax method. . . . .	6
1.5	An example of Period - Luminosity relation. . . . .	6
1.6	Hertzsprung-Russell diagram. . . . .	10
1.7	Fundamental mode and first overtone pulsations. . . . .	12
1.8	Cycle of a pulsating star. . . . .	14
1.9	Unified AGN model. . . . .	17
1.10	Impact of SMBH on Spectral Line Profiles. . . . .	20
2.3	The photometric data used in this thesis were obtained from these five surveys. . . . .	31
2.4	Gaia (E)DR3 passbands as produced by Coordination Unit 5 of the Gaia Data Processing and Analysis Consortium. . . . .	35
2.5	A simple scheme of a spectrograph. . . . .	37
2.6	The spectroscopic observations were conducted with these two telescopes. . . . .	39
2.7	Grating efficiency for R831. . . . .	39
3.1	Calibration procedure of PL relation. . . . .	51
4.1	Histogram of periods for 342 sources with 601 corresponding periods. . . . .	56
4.2	A typical example of a Lomb-Scargle periodogram for a candidate variable. . . . .	56
4.3	Color-magnitude and color-color diagrams for 28 candidates remaining after the Kuiper statistics filter. . . . .	58
4.4	SDSS spectra for 5 periodically variable sources. . . . .	61
4.5	ID = 10. . . . .	63
4.6	ID = 20. . . . .	63
4.7	ID = 21. . . . .	64
4.8	ID = 25. . . . .	64
4.9	ID = 27. . . . .	65
5.1	The normalized line profiles of the extracted MgII line. . . . .	75
5.2	Overlay the SDSS, ZTF, PS1, Gemini, and Magellan observations, and the sinusoidal fit. . . . .	76



5.3	The PoSKI model of MgII broad line for SDSS, Gemini and Magellan measurements. . . . .	76
6.1	Sample selected from the GAPS field. . . . .	83
6.2	An example of a good Mira candidate. . . . .	84
6.3	The comparison of the Gaia and periods calculated in this study. . . . .	86
6.4	The comparison of the OGLE III Miras and those from this work. . . . .	86
6.5	Comparison of the PL relations in Gaia and 2MASS from this work and Lebzelter, T. et al. (2019). . . . .	88
6.6	Comparison of the PL relations for different galaxies in JHK filters. . . . .	90

# List of Tables

4.1	The division of the sample in 4 subgroups. . . . .	58
4.2	Table of 5 long-period variability candidates. . . . .	67
4.3	Results of Monte Carlo simulations of the sample's periods. . . . .	68
5.1	Measured quantities from the broad MgII emission line. . . . .	79
6.1	The comparison of this work's PL relations with previous work. . . . .	89

# Chapter 1

## Introduction

This thesis explores the periodic variability observed in both galactic and extragalactic sources using existing optical sky surveys. The primary focus is on long-period variability, particularly in Red Giant stars and periodically changing Active Galactic Nuclei (AGN's). Recent technological advancements in sky surveys have made it possible to study these long-period sources more effectively, leading to increased interest and research in this field.

This chapter introduces variable sources and highlights their significance in modern astrophysics, emphasizing the motivation for future scientific investigations.

The fundamental concepts, including apparent and absolute magnitude, flux, luminosity, and others, are clarified in the Appendix A. This section serves as a supplementary resource, providing additional information on basic concepts.

### 1.1 Variable sources

To put it simply, variable sources are sources that exhibit changes in brightness over time. These changes may follow periodic patterns, as seen in well-known pulsating stars like for example Cepheids (e.g., Chiosi, 1990; Ripepi et al., 2023), they may be entirely unique, as observed in supernova explosions (e.g., Woosley & Weaver, 1986; Mösta et al., 2015), they may be stochastic, etc.

Variable sources are typically analyzed through their light curves (LC), which depict how the flux or magnitude of the source changes over time. An example of such a curve for a periodically variable star is illustrated in the top panel of Figure 1.1. When studying a source with periodic variability, it is often more practical to examine its phased light curve (PLC). This curve illustrates how the flux or magnitude of the source varies relative to its phase. The phase

is determined using the equation:

$$\phi = \frac{t}{P} - \text{int}\left(\frac{t}{P}\right), \quad (1.1)$$

where  $t$  represents the time of observations and  $P$  is the estimated period of the source. This approach is preferable because astronomical observations are typically not evenly spaced in time. Additionally, for sources with limited observations, folding the data into a PLC can simplify the determination of periodicity. An example of a PLC is given on the bottom panel in the Figure 1.1.

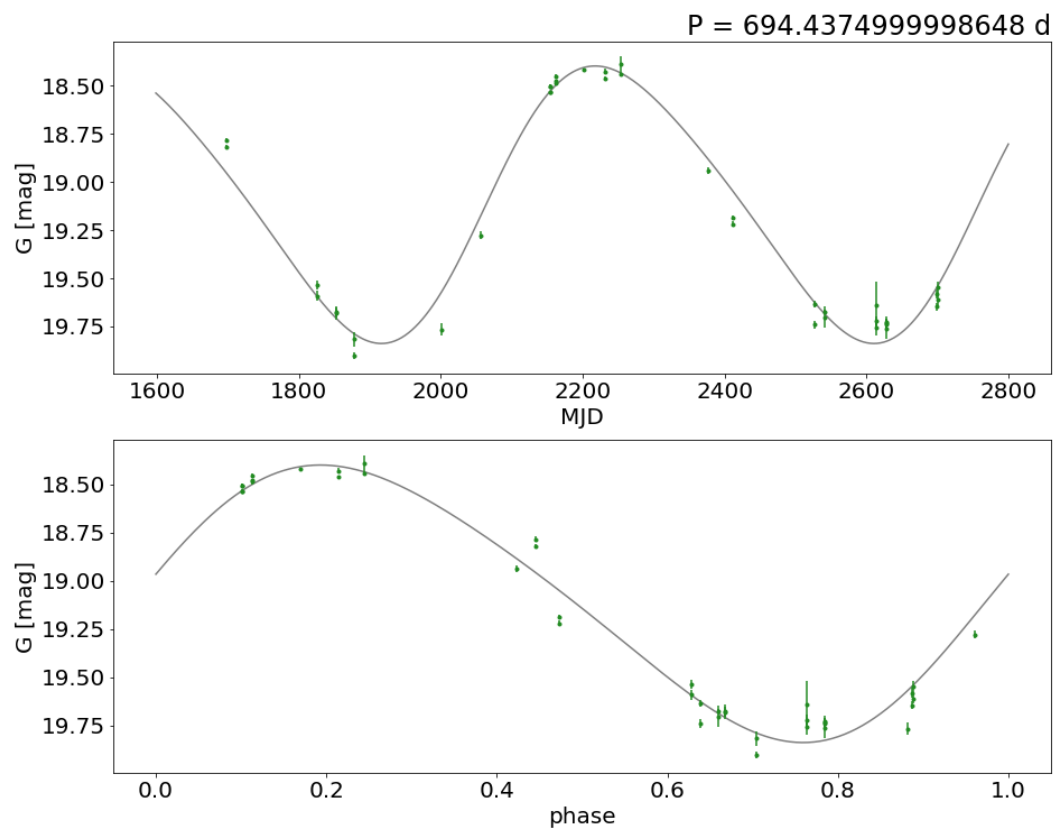


Figure 1.1: Example of a light curve and a phased light curve of a variable star in Gaia G filter.

Currently, hundreds of types and subtypes of variable stars have been identified (Samus et al., 2017) with diverse physical and chemical properties. However, it is important to note that variability is not exclusive to stars; various types of variable sources exist. These can be visually summarized in a figure known as the Variability Tree, which will be discussed in greater detail in the following section.



similar brightness change patterns.

Sources with periodic variations can have periods ranging from fractions of a second to hundreds of days, influenced by factors like their underlying physical mechanisms, mass, and age. While significant research has been conducted on these periodic sources, those with extremely long or short periods remain underexplored. This thesis aims to address this gap by focusing on sources with long-term periodicities. Such behavior is observed in various galactic and extragalactic sources. Galactic examples include long period variables (LPVs) such as red giant stars (detailed in Section 1.2), while extragalactic examples include active galactic nuclei (AGNs), discussed in Section 1.3.

Interest in periodic variables has grown since the early 20th century, when their periodic nature was first recognized as significant. The importance of these periodicities and their implications will be further detailed in the following sections.

### 1.1.2 Why are periodic sources important?

One of the greatest challenges in astronomy is determining the distance to celestial objects. As we can not directly measure these vast distances in the universe, a set of methods known as the cosmic distance ladder (CDL) (e.g., Gribbin, 1992; Greene & Cyr-Racine, 2022) was developed to estimate these distances. It includes various techniques used depending on the distance of the object being studied, as illustrated in Figure 1.3.

#### Parallax

For objects within our galaxy, a technique called parallax is employed. This method relies on the apparent shift in an object's position when observed from different locations as it is shown in the Figure 1.4. Long-term and repeated observations are necessary to measure a star's parallax by observing it at different times. This allows for detecting the apparent shift of a nearby star relative to distant background stars, which should be chosen far enough away so that their own motion is negligible compared to the nearby star's movement. Using the simple trigonometric formula:

$$\tan p = \frac{1}{d} \xrightarrow{\text{Taylor's expansion}} p \approx \frac{1}{d}, \quad (1.2)$$

where  $p$  is parallax and  $d$  is the distance from the Sun to the observed source. This approximation is accurate for small angles, where the tangent function can be simplified using the Taylor expansion. Currently, the uncertainty level in Gaia (E)DR3 data shows a median uncertainty in parallax and annual proper motion of about 0.02–0.03 mas for magnitudes  $G = 9–14$ , and around 0.5 mas for  $G = 20$  (Lindgren, L. et al., 2021). For parallax angles smaller than

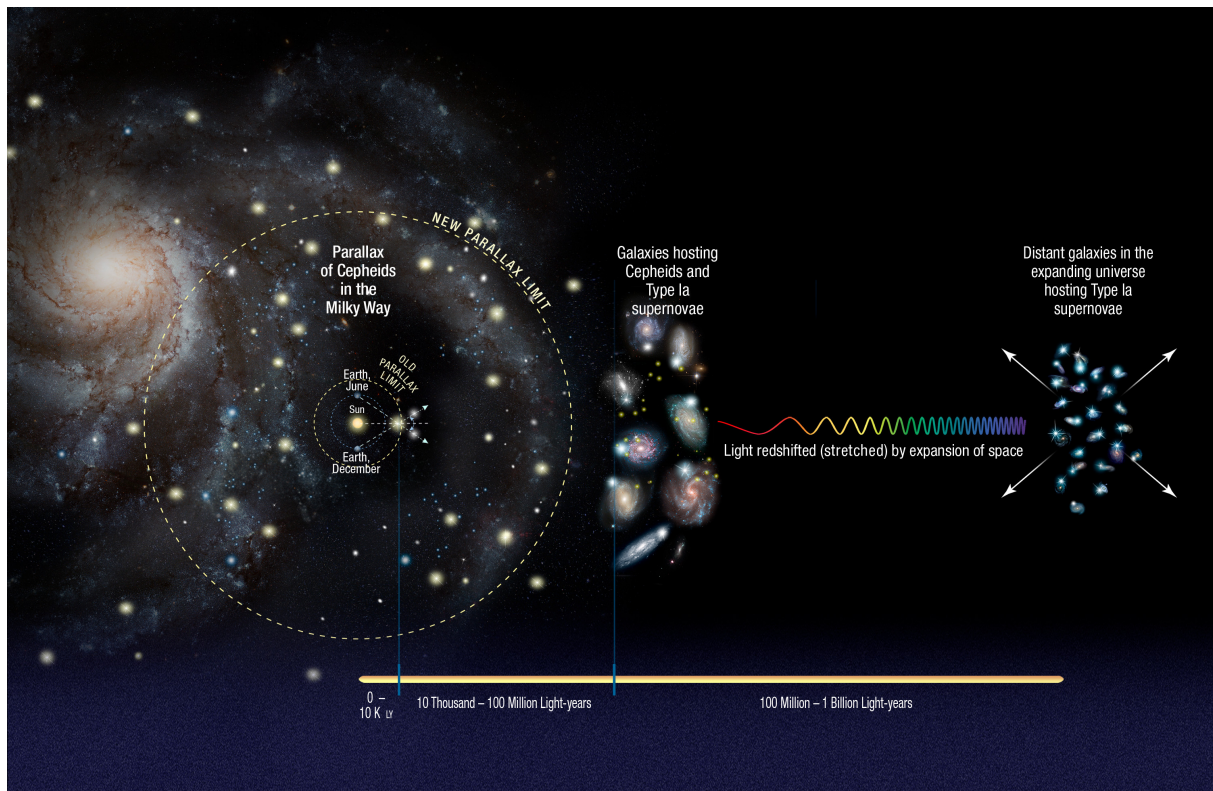


Figure 1.3: An example of the CDL to distances up to 1 billion light years. Credit: NASA, ESA, A. Feild (STScI), and A. Riess (STScI/JHU)

these values, which correspond to greater distances of about 160,000 light years (ly) for bright sources, other methods need to be used.

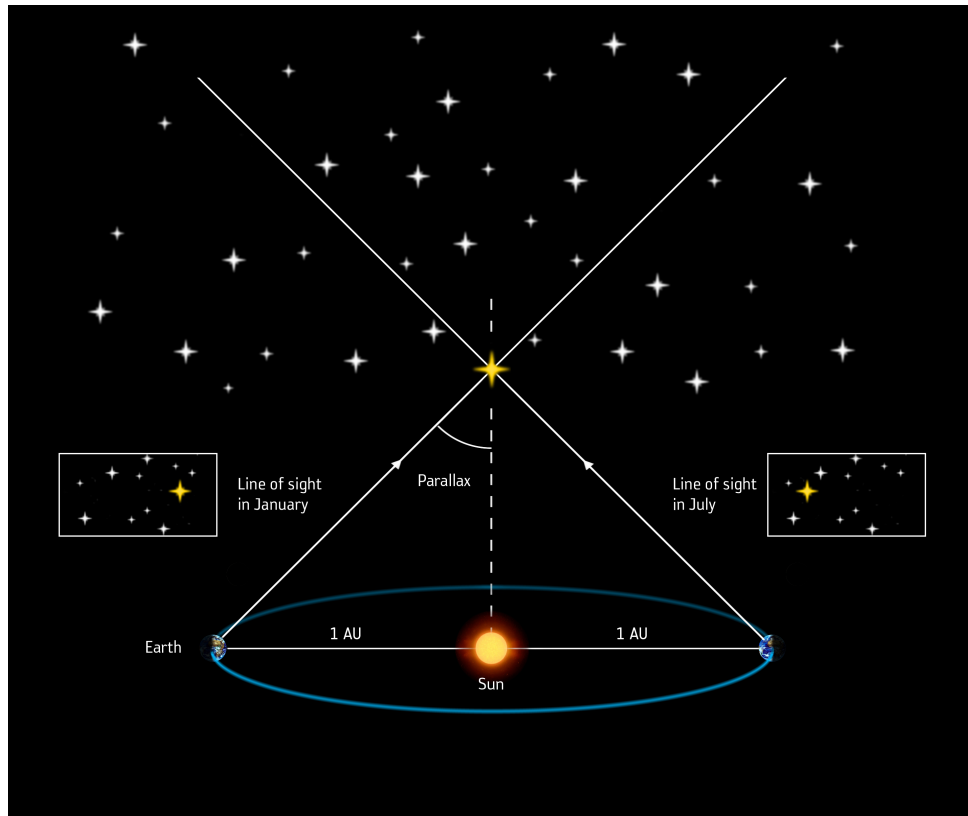


Figure 1.4: The graphical example of parallax method. Credit: ESA/ATG medialab

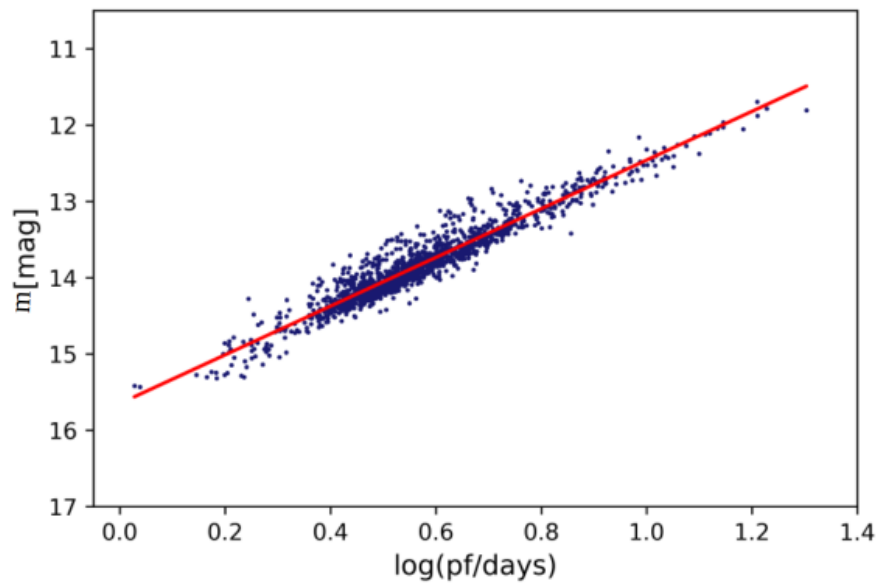


Figure 1.5: An example of the Period-Luminosity relation for Cepheid stars in the Large Magellanic Cloud (LMC), using the data from Gaia DR2.



### Period - Luminosity relation

In early 20th century, American astronomer Henrietta Swan Leavitt studied Cepheid variable stars in Small Magellanic Cloud (SMC). These stars are characterized as young and intrinsically variable, displaying regular radial pulsations. Their pulsation periods typically range from a few days to a few weeks, while their brightness varies from a few tenths of a magnitude to about two magnitudes.

Leavitt made a significant discovery during her research: she found a close correlation between the brightness of a Cepheid variable star and the logarithm of its pulsation period (Leavitt, 1908; Leavitt & Pickering, 1912). This implies that Cepheid stars with longer pulsation periods are brighter, indicating a clear relationship between the two variables called period - luminosity (PL) relation:

$$M = a \cdot \log(P) + b, \quad (1.3)$$

where  $M$  is the luminosity of the Cepheid variable star,  $P$  is the variation period, and  $a$  and  $b$  are coefficients which depend on the different types and chemical compositions of the stars and the photometric bandpasses of observation. An example of a PL relation is shown in Figure 1.5.

This relation made a significant impact on the distance estimations for galaxies that are up to 100 million ly away from the Sun and is still one of the most researched concepts in astronomy (e.g., Clementini et al., 2019; Trahin et al., 2021). It involves estimating the PL relations for objects with well-known distances, which are then used as reference points to estimate the distances to more distant objects.. The PL relation has later been proven effective in distance estimation for periodically variable stars other than Cepheids, such as RR Lyrae (e.g., Catelan et al., 2004; Clementini et al., 2019), Mira variables (e.g., Glass & Evans, 1981; Sanders, 2023) and other long-period variable stars (e.g., Mosser et al., 2013; Lebzelter et al., 2019).

There are several assumptions that have to be met while using PL relation as the method of distance estimation:

- *The calibrating set needs to be equal in properties to the set to which the distances are being determined to, or appropriate transformations should be known.* While it is assumed that stars share similar characteristics across galaxies, the actual composition and environmental conditions during their formation can vary. Therefore, the assumption that variable stars in the target galaxy are the same as those in the Milky Way may not be accurate, as these stars could have formed in different environments and have different chemical compositions (e.g., Kennicutt & Evans, 2012; Hasselquist et al., 2021).
- *The calibration is done using the same type of stars.* Some periodically variable sources share similar characteristics (see e.g., Figure 1.2). Different types of stars often occupy

distinct PL ridges and failing to account for this can result in inaccuracies in PL calibration.

- *The periods are correctly and precisely determined.* Determining the periods requires the application of rigorous statistical methods for calculation and filtering. In this thesis the procedure for this is in greater detail explained in Section 3.1. Additionally, the challenge is heightened by the variable stars that exhibit multiple periods (see e.g., Tabur et al., 2010; Soszyński et al., 2010, 2013). It is crucial to handle this aspect carefully, as these stars may correspond to multiple ridges of the PL relation.
- *The reddening and extinction are correctly taken into account.* Both reddening and extinction involve the interaction of light with interstellar dust. Reddening refers to the color shift towards the red end of the spectrum due to selective scattering or absorption of shorter-wavelength light, while extinction encompasses the overall reduction in the amount of light reaching us across all wavelengths due to various processes in a medium. There is a method that takes care of this problem - Wesenheit function (Madore, 1982). The correction includes the linear combination of the observed magnitudes at different wavelengths, with appropriate coefficients chosen to minimize the effects of extinction and reddening. The specific form of the function depends on the properties of the star being studied and the observational filters used (e.g., Caputo et al., 2000; Jordi et al., 2010a).

### **Determining distance after calibration of the PL relation**

The next rung on the CDL involves Type Ia supernovae (SNe Ia) originating from binary systems where a white dwarf accumulates material from its companion star. Ultimately, as the white dwarf approaches the Chandrasekhar mass limit (around  $1.44 M_{\odot}$ ), electron degeneracy pressure becomes inadequate, triggering a collapse and culminating in a supernova explosion. They are used as distance estimators primarily because they exhibit consistent peak luminosity. By observing the apparent brightness of a SN Ia in comparison to its known intrinsic luminosity (calibrated using, for example, Cepheids), it is possible to determine its distance from Earth up to about 1 billion ly.

Other methods for estimating distances include the Tully-Fisher relation, which links the rotation speed of spiral galaxies to their brightness and is effective up to 200 million light-years; Gravitational Lensing, which uses the bending of light by gravitational fields to measure distances up to several billion light-years; and the Cosmic Microwave Background (CMB), which is the afterglow of the Big Bang and reveals information about the early universe, reaching to

the edge of the observable universe. While there are additional distance estimation methods, all except parallax and PL calibration are not utilized in the research presented in this thesis and will not be described in detail.

### 1.1.3 Intrinsically periodically variable stars

Cepheids, RR Lyrae, Miras, and other stars that are used for calibrating the PL relation are intrinsically variable stars. Such changes occur due to various mechanisms related to the evolutionary stage of each star.

The development of a particular star can be understood from the Hertzsprung-Russell (HR) diagram, as shown in Figure 1.6. This diagram illustrates the luminosity of each star in relation to its surface temperature (or color). What stands out immediately is that the majority of stars align along a diagonal line referred to as the "main sequence". The subsequent evolution of a main sequence star depends on its initial mass, resulting in distinct trajectories. Cepheids and RR Lyrae stars typically originate from intermediate-mass main-sequence stars, progressing through various phases in their lifecycle. These stars demonstrate stability during their main-sequence phase, but as their evolution advances, they enter periods of instability, transforming into pulsating variable stars. These pulsations arise from periodic changes in the ionization of helium and hydrogen in the star's outer layers, leading to fluctuations in temperature and pressure. Mira stars, a specific type of red giant stars, undergo unique evolutionary and pulsating processes, which will be detailed in the following chapter. Other star types fall outside the scope of this thesis research and will not be explained in detail.

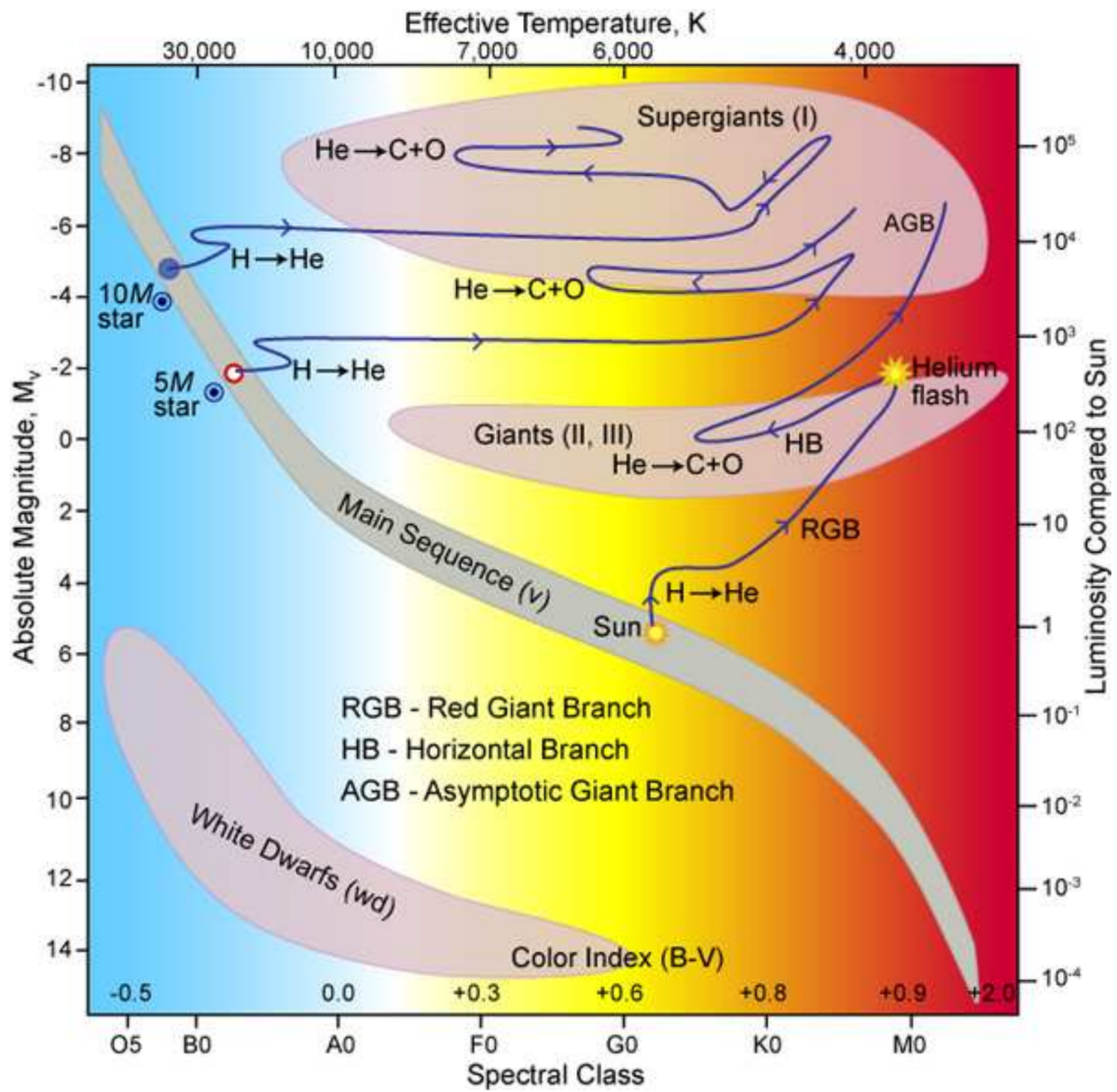


Figure 1.6: Hertzsprung-Russell diagram. Credit: Wiescher (2009)

## 1.2 Red Giants

During the main sequence phase, which constitutes the majority of a star's life, nuclear fusion occurs predominantly in the core, where hydrogen is burned. As stars exhaust their hydrogen supply, they leave the main sequence. Low- and intermediate-mass stars then expand and cool, becoming red giants. This process will be elaborated in later sections.

The giant region includes red giants and asymptotic giant branch (AGB) stars. AGB stars have carbon- and oxygen-rich cores, with helium and hydrogen burning in surrounding shells. This thesis will focus on the study of red giants, including AGB stars.

### 1.2.1 Summary of the low-mass star evolution after the main sequence

The low-mass star evolution after the main sequence presented in this section is explained using Kippenhahn et al. (2013) as the main reference. Stars with a mass less than  $2.3M_{\odot}$  undergo a significant transformation after using all the hydrogen in their core. During this stage, the hydrogen-burning shell surrounding the core causes helium to accumulate in the core. Because of the increase in the core's mass (He accumulation), it gradually contracts leading to a rise in core's temperature. Simultaneously, the outer envelope, abundant in hydrogen, expands and cools. Because of the cooling, the star becomes redder and because of the expanding - the star becomes larger and more luminous (see Figure 1.6).

Once the He core becomes massive enough, it collapses. This leads to helium ignition, accompanied by a sudden increase in luminosity, known as a helium flash. When helium ignites (at  $\sim 3 \cdot 10^8$  K), the cooling of the outer layers and the increase in luminosity cease, and such stars 'return' to the left side of the HR diagram (the so-called Horizontal Branch - HB, see Figure 1.6).

Once the core runs out of all the He, as a product of helium burning, C and O accumulate in the core. This core is surrounded by a shell of burning He and an inter-shell of He which is a product of the H-burning shell. During the next phase of evolution, the burning in the hydrogen shell stops, while the burning in the helium shell persists, supplying additional carbon and oxygen to the core. The star moves along the asymptotic giant branch (AGB) stage (see Figure 1.6). As the star expands, the luminosity increases.

Because of the burning of the He in the inter-shell, the H shell reheats and reignites which provides more He in the He shell. At this time, He shell is unstable and produces helium flashes which are known as thermal pulses. This pulse pushes the H shell outwards which then cools down. After the pulse is finished, H reignites and the whole process starts again.

These pulses happen on a scale of millions of years. Since these events take such a long

time, it is challenging to observe them (e.g. recent paper: Molnár et al., 2019) and use them to set PL relations. In simpler terms, they are not utilized for this purpose. Thermal pulses are just one aspect of the complex behavior stars exhibit in their later evolutionary stages. The following section will explain the periodic variations that are actually employed for establishing PL relations.

### 1.2.2 Pulsation of Mira stars

This section is written with Carroll & Ostlie (2017) as the main reference. The periodic variations observed in stars, which are measured and utilized to calibrate the PL relation, result from standing sound waves within the star's interior. These waves induce oscillations mostly in radial pulsation modes. The fundamental mode involves matter moving uniformly in the radial direction. Some stars exhibit pulsations in higher overtones of spherical harmonic functions. For example, in the first overtone (FO) the matter moves in the opposite direction. For the visual explanation, see Figure 1.7.

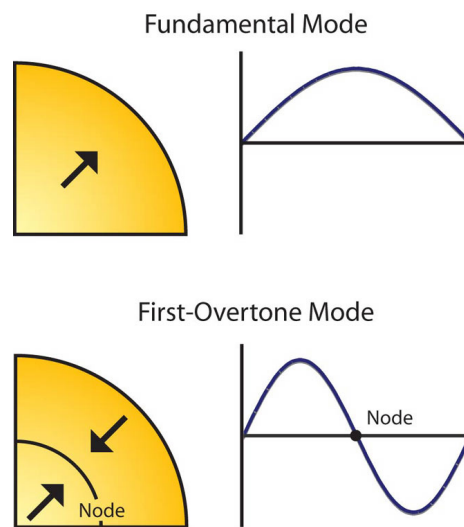


Figure 1.7: Visual representation of the stellar pulsation in fundamental mode and first overtone. Credit: [www.aavso.org](http://www.aavso.org)

The part of research described in this thesis dedicated to red giants specifically focuses on Mira stars, which are cool giant stars located near the tip of the AGB. These stars exhibit pulsations solely in the fundamental mode, as indicated by previous studies (Wood & Sebo, 1996a; Barthes, 2006). The pulsation periods of Mira stars can range from tenths to thousands of days. Notably, one key characteristic of their pulsations is the substantial amplitude observed in the visual (V) filter, approximately 2.5 magnitudes.

One of the early explanations for stellar pulsations was the so-called "epsilon mechanism". It was believed that changes in energy production in the star's core could cause observed oscillations. However, this was soon found to be insufficient. While changes in energy production within the star's core could potentially induce oscillations, further investigation revealed that additional factors and processes were at play. Specifically, the epsilon mechanism failed to adequately address the complex interplay between pressure, temperature, opacity, and energy transfer within stellar interiors that ultimately govern the pulsation behavior of stars.

Eddington then proposed the valve mechanism, today called by him. He suggested that if certain layers of a star became more opaque during compression, they could trap photons (energy). When these layers later became less opaque due to pressure changes, the trapped energy would be released, causing the outer layers to expand. However, this mechanism faced challenges because, according to Kramer's opacity law that connects opacity  $\kappa$ , temperature  $T$  and density of the gas  $\rho$ :

$$\kappa \propto \frac{\rho}{T^{3.5}}, \quad (1.4)$$

where  $\kappa$  decreases with increasing  $T$  during compression, contrary to what the Eddington valve requires.

It was discovered that for stars to pulsate, specific internal conditions are needed. Partial ionization zones were identified, where some energy during compression is used to ionize atoms rather than increase temperature. During expansion, energy is released as atoms recombine. This reduces the temperature dependence of opacity, aligning with Kramer's law, and creates conditions for photon trapping.

This process, known as the kappa ( $\kappa$ ) mechanism, is further supported by the gamma ( $\gamma$ ) mechanism. In partial ionization zones, heat from adjacent layers transfers to these zones, trapping even more energy.

Most stars have two main partial ionization zones. One zone involves ionized hydrogen (H II) and singly ionized helium (He II) at temperatures around 15,000 K. The other involves doubly ionized helium (He III) at temperatures around 40,000 K. Models show that the He II zone, found in deeper layers, is essential for the oscillations of variable stars along the instability strip.

The exact mechanisms for Mira-type variable stars are not yet fully understood, but they are also believed to involve the described  $\kappa$ -mechanism. This dynamic interplay between compression, ionization, and expansion governs the pulsation behavior observed in Mira stars and is shown in the Figure 1.8.

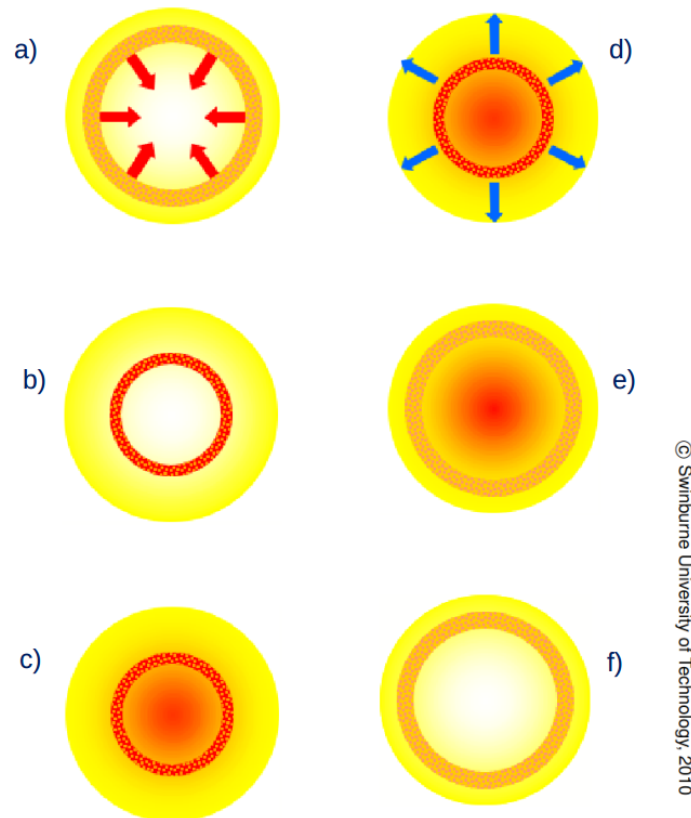


Figure 1.8: Cycle of a pulsating star. Here is the simple summary of the explained mechanism. a) During this phase of the pulsation cycle, a layer of material within the star collapses due to gravitational pull. b) This inward movement causes the layer to compress, resulting in increased temperature and opacity to light. c) As a consequence of heightened opacity, the diffusion of radiation through the layer decelerates, causing thermal energy to accumulate beneath it. d) The rising pressure underneath the layer pushes it outward. e) During its outward movement, the layer undergoes expansion, undergoes cooling, and exhibits increased transparency to radiation. f) With increased transparency, energy can escape from beneath the layer, causing a decrease in pressure below it. Credit: <http://astronomy.swin.edu.au/sao>

### 1.2.3 Red Giants as distance estimators

Periodically variable red giant stars possess qualities that make them valuable for distance estimation. They exceed RR Lyrae type variable stars in luminosity and can even rival long-period Cepheids, particularly among evolved AGB stars. Consequently, their photometry can be reliably obtained not only within the Milky Way and nearby satellite galaxies but also across the broader expanse of the Local Group. Red giants exhibit a wide distribution across various galactic structures (e.g., Javadi et al., 2011; Sakamoto et al., 2012), including disks, bulges, and haloes, unlike Cepheids, which are predominantly confined to crowded galactic disk regions. This widespread distribution makes red giants convenient tracers for studying diverse galactic



structures.

Additionally, red giants emit radiation predominantly at longer wavelengths compared to Cepheids and RR Lyrae stars. This characteristic makes them less susceptible to interstellar extinction, particularly when observed in the near-infrared part of the spectrum.

The current tension between the  $4\sigma$  and  $6\sigma$  measurements of the Hubble constant (e.g. Verde et al., 2019; Riess et al., 2022) reflects a significant discrepancy in the value of the universe's expansion rate. Measurements from the early universe, such as those derived from the Cosmic Microwave Background (CMB), suggest a lower Hubble constant, while local measurements, like those from supernovae and Cepheid variable stars, indicate a higher rate. This growing tension between the two sets of measurements, reaching up to  $6\sigma$ , suggests either a fundamental gap in our understanding of universe or the presence of new physics beyond the standard model. This is why additional estimations derived from independent methods are crucial for validation. Utilizing large ensembles of variable red giant stars provides an independent method for determining the Hubble constant, complementing existing approaches and enhancing the robustness of distance scale measurements.

Variability of AGB stars manifests through various pulsation modes, such as semi-regular variables (SRVs) and irregular variables (IRVs), each displaying unique traits and evolutionary paths. However, Miras stand out as a focal point due to their large amplitudes and consistent pulsation behavior. This motivated the focus on Miras for the research conducted in this thesis.

## 1.3 Active Galactic Nuclei

Active Galactic Nuclei (AGNs) are extremely luminous regions located at the centers of certain galaxies. These regions are powered by the accretion of matter onto a supermassive black hole. AGNs are distinguished by their extraordinary brightness across various wavelengths, including radio, optical, ultraviolet, X-ray, and gamma-ray. In this section, key references used were Antonucci (1993a); Peterson (1997); Netzer (2015) as they offer comprehensive overviews of AGNs and their components.

### 1.3.1 AGN components

Several components constitute AGN:

- **Supermassive Black Hole:** At the core of an AGN lies a supermassive black hole, with mass ranging from millions to billions of times the mass of the Sun. The gravitational pull of this black hole causes nearby matter to spiral inward.
- **Accretion Disk:** An accretion disk, a rotating disk of gas and dust, lies in the plane around the black hole. As material in the disk spirals inward, it heats up due to friction and gravitational forces. This heating causes the disk to emit radiation that closely follows a multi-temperature black body spectrum, with each region of the disk emitting as a black body at a different temperature. The innermost, hottest regions emit primarily in the ultraviolet range, while the outer, cooler regions emit more in the optical wavelengths. As a result, the overall emission typically peaks in the optical or ultraviolet wavelengths, depending on the black hole's mass and accretion rate. The accretion disk is the primary source of continuum emission in AGNs, with observed luminosities ranging from  $10^{42}$  -  $10^{46}$  erg/s.
- **Broad Line Region (BLR):** Closer to the black hole, fast-moving clouds of gas emit broad emission lines with widths typically ranging from 1000 to 10000 km/s. This region is known as the Broad Line Region. The high velocities of these clouds result in the broadening of spectral lines, a key signature of AGN.
- **Narrow Line Region (NLR):** Farther from the black hole, slower-moving clouds of gas emit narrow spectral lines with widths usually around 200 to 1000 km/s. This area is referred to as the Narrow Line Region. The gas in this region is ionized by the radiation from the accretion disk and the BLR.

- **Dust Torus:** Surrounding the accretion disk and the BLR, there is a torus-shaped region of dust. This dust absorbs and re-emits energy, particularly in the infrared spectrum. The orientation of this torus relative to our line of sight can affect the observed properties of the AGN.
- **Jets:** In some AGNs, relativistic jets of charged particles are ejected perpendicular to the accretion disk. These jets can extend over vast distances, even beyond the host galaxy. They are often observed in radio and X-ray wavelengths and are a hallmark of radio-loud AGNs.

A scheme of an AGN can be seen in the Figure 1.9.

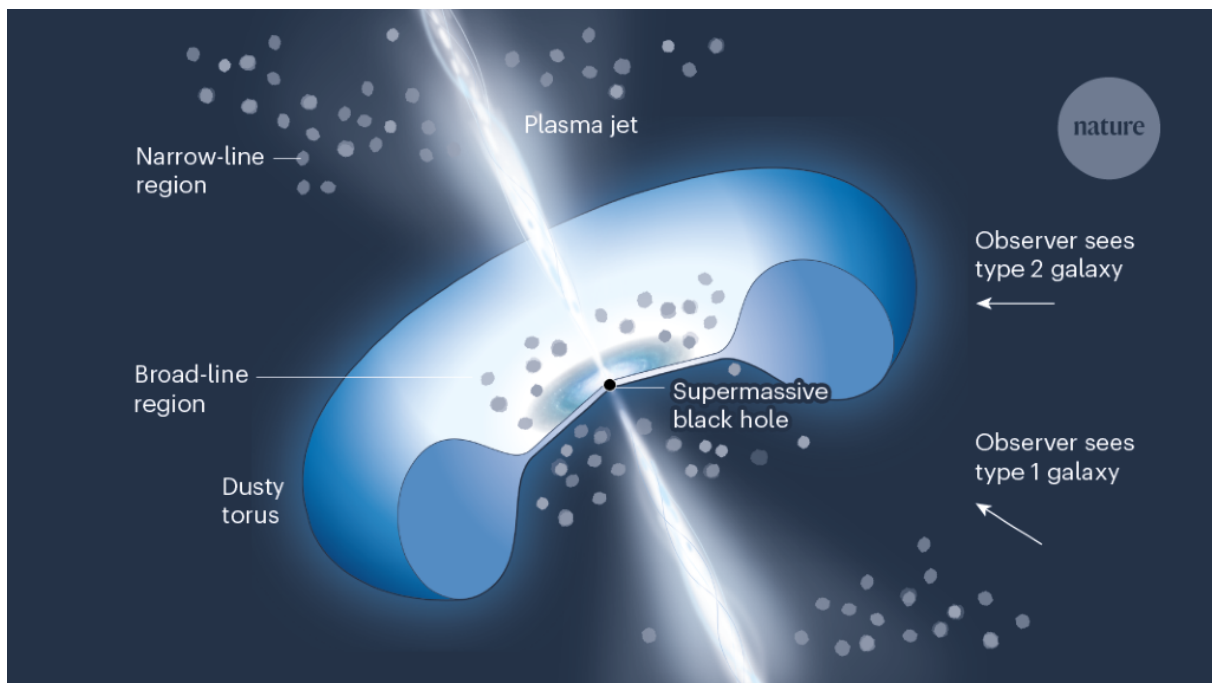


Figure 1.9: AGN components and explanation of the Unified AGN model. Credit: Antonucci (2022)

### 1.3.2 Types of AGNs

AGNs are classified into several types based on their observational characteristics, particularly their luminosities and the presence or absence of certain spectral features. The primary classes of AGNs are as follows:

### Seyfert Galaxies

Seyfert galaxies are a class of AGNs discovered by Carl Seyfert (Seyfert, 1943) and are found in spiral galaxies. They are further divided into two types:

- **Seyfert 1 galaxies** exhibit both broad and narrow emission lines in their spectra.
- **Seyfert 2 galaxies** show only narrow emission lines, with the broad lines being obscured.

### Quasars

Quasars are the most luminous AGNs, discovered by Schmidt (1963). They can outshine their host galaxies and are visible at very high redshifts.

### Radio Galaxies

Radio Galaxies are AGNs that emit large amounts of energy in the radio part of the spectrum. They are divided into:

- **Fanaroff-Riley type I (FR I) radio galaxies** which have jets that fade with distance from the nucleus (Fanaroff & Riley, 1974).
- **Fanaroff-Riley type II (FR II) radio galaxies** which have jets that remain bright and terminate in bright radio lobes.

### Blazars

Blazars (Urry & Padovani, 1995) are a subclass of AGNs with relativistic jets pointed nearly directly toward Earth. They are characterized by rapid variability and strong emission across the electromagnetic spectrum, from radio to gamma rays. Blazars are divided into two types:

- **BL Lacertae objects (BL Lacs)** which show weak or no emission lines,
- **Optically Violent Variables (OVVs)**, which display strong, broad emission lines similar to quasars.

### 1.3.3 The Unified Model of AGNs

The unified model of AGNs posits that the different types of AGNs can be explained by a single model when orientation effects are taken into account. In the study by Antonucci & Miller (1985), the galaxy NGC 1068, classified as a Seyfert 2 galaxy, was observed in polarized light.

Unexpectedly, a Seyfert 1 spectrum with broad emission lines was detected. This discovery indicated that AGNs, typically categorized by the presence or absence of broad emission lines, might actually be physically similar, with the observed differences resulting from the presence of an absorber. In subsequent years, the Unified Model of AGNs (Antonucci, 1993b) was established. This model suggests that the variations in observed properties are primarily due to the angle between the AGN's rotational axis and the observer's line of sight. The model posits that a thick torus of dust surrounds the accretion disk, obscuring the central region of the AGN from certain perspectives. This is illustrated in the Figure 1.9.

- When viewed edge-on, the torus obscures the broad-line region, and the AGN appears as a Seyfert 2 galaxy or a narrow-line radio galaxy.
- When viewed face-on, the broad-line region is visible, and the AGN appears as a Seyfert 1 galaxy, quasar, or blazar.

## 1.4 Impact of SMBH on Spectral Line Profiles

In AGNs, SMBHs are surrounded by an accretion disc emitting photons across a broad energy spectrum, from X-rays to far infrared. The high-energy X-ray and UV photons photoionize the gas in the BLR which is influenced by the SMBH's gravitational force. This photoionized gas emits lines whose width and shift are used to determine the SMBH mass.

As shown in Figure 1.10 (Popović, 2020), photoionized clouds exhibit varying velocities: those closer to the SMBH (green) move faster and contribute to the line wings, while more distant clouds contribute to the central part of the broad line. Clouds in rotational motion towards the observer appear in the blue part of the line, while those receding appear in the red part. The combination of rotational motion and random gas velocities, depending on their distance from the SMBH, causes line broadening. The Full Width at Half Maximum (FWHM) reflects both rotational and random motions of the gas, both influenced by the SMBH's gravitational field. Thus, for virialized gas motion, the FWHM is linked to the SMBH mass. Additionally, if the emitting region is close to the SMBH, gravitational redshift can cause observable line redshifts and profile asymmetries (Popovic et al., 1995).

### 1.4.1 SMBH Mass determination using broad lines

Assuming the gas in the SMBH vicinity is virialized, the line FWHM reflects the rotational velocity ( $v_{\text{gas}}$ ) due to gravitational motion around the SMBH with mass  $M_{\text{BH}}$ . The gas velocity is related to the SMBH mass by:

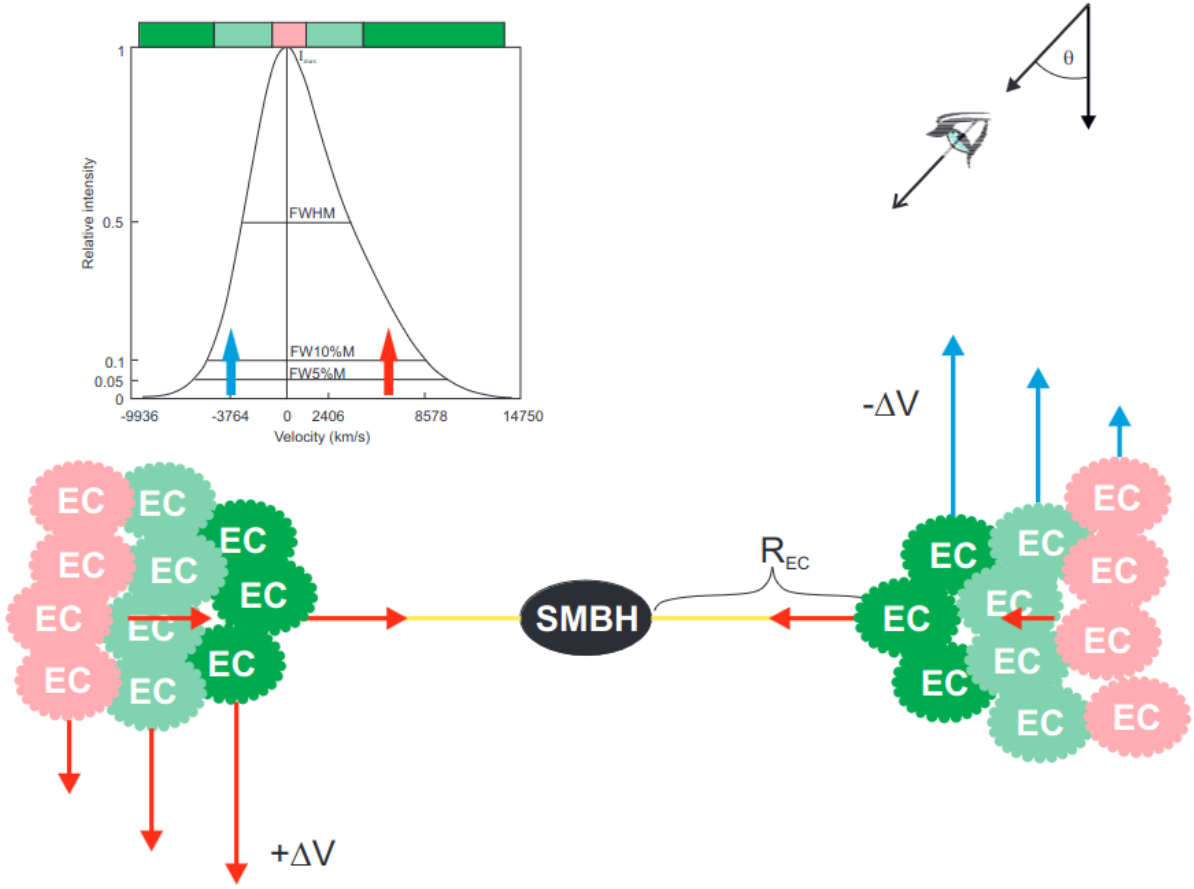


Figure 1.10: The diagram shows emitting gas motion near an SMBH (lower section) and the resulting broad line profile (upper section) from various emitting clouds. Red arrows indicate receding velocities and blue arrows indicate approaching velocities. The upper panel displays line profiles with red asymmetry due to gravitational redshift, marked by horizontal red arrows towards the central SMBH. Credit: Popović (2020)

$$v_{\text{gas}}^2 = \frac{GM_{\text{BH}}}{R} \quad (1.5)$$

where  $R$  is the radial distance of the emitting region that produces a broad line with respect to the BH center, and  $G$  is the gravitational constant.

The FWHM is related to the gas velocity as:

$$\text{FWHM} = v_{\text{obs}} = v_{\text{gas}} \cos \theta \quad (1.6)$$

where  $v_{\text{obs}}$  is the projected velocity on the line of sight (LOS) and  $\theta$  is the inclination angle. The SMBH mass is then obtained using the following relation (Peterson, 2014):

$$M_{\text{BH}} = f \cdot \frac{v_{\text{obs}}^2 R_{\text{BLR}}}{G} \quad (1.7)$$

where  $f$  is the virial factor, which includes the inclination and geometry of the BLR.

One approach to estimate the SMBH mass is to use the luminosity of broad lines, as the dimension of the BLR is connected with the luminosity (Dibai, 1977, 1978; Bochkarev & Gaskell, 2009):

$$R_{\text{BLR}} \sim L_{\text{line}}^{1/3}, \quad (1.8)$$

and then the SMBH mass can be obtained as:

$$M_{\text{BH}} = \frac{3}{2} \frac{R_{\text{BLR}} v^2}{G}. \quad (1.9)$$

A more accurate method involves reverberation mapping, where the BLR size is determined by the time delay ( $\Delta t$ ) between continuum and line flux variability:

$$R_{\text{BLR}} \approx c \Delta t \quad (1.10)$$

where  $c$  is the speed of light.

The relation between  $R_{\text{BLR}}$  and the continuum luminosity ( $L_{\text{cont}}$ ) (e.g. Kaspi et al., 2000, 2005; Du et al., 2016) is given by:

$$\log(R_{\text{BLR}}) = a \cdot \log L_{\text{cont}} + b \quad (1.11)$$

where  $R_{\text{BLR}}$  is the dimension of the BLR (emitting the broad line) and  $L_{\text{cont}}$  is the nearby continuum luminosity. This method is crucial for determining SMBH masses in AGNs across different cosmological scales.

To conclude, measuring SMBH masses and their relationship with host galaxies provides vital insights into the Universe's evolution. Direct methods analyze the dynamics of stars and gas influenced by the SMBH, while indirect methods use correlations between galaxy parameters and black hole masses (e.g. Ferrarese & Merritt, 2000; Shankar et al., 2019). In AGNs, virialized gas emits broad lines reflecting gravitationally bound motion, aiding in SMBH mass estimation through techniques like FWHM analysis and polarization in broad lines, showing consistency with other methods like reverberation mapping and  $M_{\text{SMBH}} - \sigma^*$  relation (e.g. Afanasiev et al., 2019).

## 1.5 Variability in AGNs

### 1.5.1 Stochastic variability

All AGNs exhibit variable behavior, which is predominantly stochastic in nature. This means that AGNs show unpredictable changes in their brightness and emission across various wavelengths. Several mechanisms are believed to contribute to this kind of behavior. The turbulent nature of the accretion disk around the supermassive black hole can cause random fluctuations in the emitted light. Localized changes in the accretion rate and temperature within the disk can lead to variations in brightness (e.g. Krolik et al., 1991). Also, the torus of dust and gas surrounding the accretion disk is not uniform. Instead, it consists of clumps that can move in and out of the line of sight, causing irregular obscuration and variations in the observed emission (e.g. Nenkova et al., 2008). In AGNs with relativistic jets, instabilities within the jet can lead to irregular changes in emission. The interaction of the jet with the interstellar medium can also introduce variability Marscher & Gear (1985). Furthermore, stars or compact objects passing in front of the AGN can act as gravitational lenses, temporarily amplifying the light from different parts of the AGN. This can lead to random, short-term variations in brightness (e.g. Wambsganss et al., 1990).

### 1.5.2 Periodic variability

In addition to stochastic changes, some AGNs exhibit periodic behavior. These phenomena are currently a major topic in astronomy. Technological advancements have significantly improved the understanding of this behavior in AGNs, making it one of the main subjects discussed in this thesis.

Explanations for the periodic behavior in AGNs include a variety of astrophysical phenomena. One such explanation is radio jet precession, where the jets emitted by the AGN change direction over time (e.g. Kudryavtseva et al., 2011). Another possibility is the presence of tilted or warped accretion disks, which can cause periodic variations in the emitted light as different regions of the disk come into view (Tremaine & Davis, 2014). Tidal disruption events, where a star is torn apart by the gravitational forces of the supermassive black hole, can also lead to periodic emissions as the remnants of the star interact with the black hole's accretion disk (e.g. Mandel & Levin, 2015). Additionally, supermassive binary black hole systems, where two black holes orbit each other, can produce regular oscillations in the emitted light due to their interactions and gravitational influences (e.g. Graham et al., 2015a; Valtonen et al., 2008; Liu & Gezari, 2018).



### Supermassive binary black hole systems as explanation of periodicity in AGNs

Supermassive binary black hole systems (SMBBHs) are predicted to exist in the centers of many galaxies (e.g. Begelman et al., 1980; Merritt & Milosavljević, 2005). However, detecting them is challenging as they often produce activity similar to that of active galactic nuclei (AGN) (see e.g. review, Popović, 2012).

Peculiar spectral line profiles, such as double-peaked emission lines, and periodic oscillations in light curves can suggest the presence of SMBBHs. However, these indicators are often masked by AGN activity and observational limitations (Eracleous et al., 2012; Li et al., 2016; Guo et al., 2018, e.g. ).

Direct identification of close binary (CB) SMBBHs (e.g., resolving the pair and monitoring gas dynamics) is challenging due to small angular separations, which exceed the resolving power of current instruments. Spectroscopy, however, can provide insights into CB-SMBBH dynamics, though spectral line effects cannot unambiguously confirm CB-SMBBH existence. Asymmetries and double-peaked emission line profiles in active galactic nuclei (AGNs) have been observed and studied (e.g. Eracleous & Halpern, 1994; Kim et al., 2020; Dias dos Santos et al., 2023). The most thoroughly investigated cases include changes in line profiles (e.g. Runnoe et al., 2017; Kollatschny et al., 2018; Wang & Bon, 2020; Popović et al., 2023), possibly explained by binary SMBH systems. Magnetohydrodynamic (MHD) simulations model how a binary system excavates surrounding material, forming a circumbinary disk (CBD) (Bogdanović et al., 2022). Material from the CBD's inner edges accretes onto SMBHs, forming disks around them. The BLR can be complex, with emission from each accretion disc ionizing nearby gas and creating BLRs (BLR1 and BLR2), while the total disc continuum ionizes gas around the system, forming a circum-binary BLR (cBLR). This setup produces broad emission lines from BLR1 and BLR2, with stationary emission from the cBLR.

Confirming SMBBHs requires long-term monitoring of spectroscopic and photometric variability (e.g. Barth et al., 2015; Runnoe et al., 2015; Shapovalova et al., 2016; Kovačević et al., 2020b). Future monitoring campaigns, such as the Vera C. Rubin Observatory's Legacy Survey of Space and Time (LSST) will provide appropriate cadence and survey depth for optical detection of candidate SMBBH systems. With accurate light curves in *ugrizy* filters and a limiting magnitude of approximately 24 mag from a single image, LSST is projected to detect 20-100 million variable quasars. These quasars are assumed to be compact massive black hole binaries ( $M = 10^5\text{--}9M_{\odot}$ ) with distinct periodic light-curves across redshifts  $z=0\text{--}6$  and orbital periods  $P=1\text{--}70$  days. Some ultra-compact binary quasars ( $P \leq 1$  day) may evolve into the mHz gravitational wave frequency band over 5-15 years, serving as "LISA verification binaries" (Xin & Haiman, 2021).

## 1.6 Multi-wavelength Observations in Astronomy

Different parts of the electromagnetic spectrum serve various types of astronomical studies, each offering unique insights into the universe. Radio observations are utilized to study cold gas and the cosmic microwave background. These observations can reveal large-scale structures in the universe, including the distribution of galaxies and the remnants of the Big Bang. Additionally, radio waves have been instrumental in imaging phenomena such as the supermassive black hole (SMBH) in M87 using the Event Horizon Telescope (EHT). This imaging not only reveals cold gas but also the dynamics of hot plasma around the SMBH, providing a broader understanding of these extreme environments.

Infrared observations are crucial for uncovering dust-enshrouded regions and cooler objects. Infrared light can penetrate dust clouds that block visible light, allowing astronomers to study star formation regions, protostars, and the structure of galaxies hidden by dust.

Ultraviolet observations are used to investigate hot, young stars and active galactic regions. Since ultraviolet light is emitted by high-energy processes, these observations provide valuable information about the early stages of star formation, the composition of stellar atmospheres, and the activity in galactic nuclei.

X-rays and gamma rays examine high-energy processes in black holes, neutron stars, and supernovae. X-ray observations probe the hot corona around black holes and the high-energy processes occurring in the innermost regions of active galactic nuclei. Gamma-ray observations detect the most energetic processes, such as those in relativistic jets and explosive events like supernovae and gamma-ray bursts.

Each part of the spectrum offers unique information, making multi-wavelength studies essential for a comprehensive understanding of the universe.

### 1.6.1 Observations of Variable Stars

Variable stars are best observed in the optical part of the electromagnetic spectrum because they emit most of their energy in this range. Observing variable stars in the optical spectrum allows for precise measurements of their brightness variations, which are crucial for studying their physical properties and behavior.

Near-infrared (NIR) observations are also important, especially for variable stars obscured by dust, such as Mira variables and other long-period variables. NIR data can penetrate dust clouds that obscure visible light, providing insights into the cooler outer layers of stars.

Ultraviolet (UV) observations can reveal high-energy processes in the atmospheres of variable stars, particularly those with hot components such as binary systems with white dwarfs,

neutron stars, or hot massive stars. UV data can provide information about temperature changes, stellar winds, and accretion processes in these systems.

X-ray observations are crucial for studying variable stars that emit high-energy radiation, such as cataclysmic variables, X-ray binaries, and other systems with compact objects. X-rays can penetrate dense material and reveal processes like accretion onto white dwarfs, neutron stars, or black holes.

Radio observations are valuable for studying the magnetic activity and particle acceleration in variable stars, particularly those with strong magnetic fields like certain types of flare stars and magnetic cataclysmic variables. Radio telescopes can detect synchrotron radiation and other emissions associated with stellar flares and magnetic phenomena.

### **1.6.2 Observations of Active Galactic Nuclei (AGNs)**

Active Galactic Nuclei (AGNs) emit energy across the entire electromagnetic spectrum, with different components becoming prominent at various wavelengths. Radio observations reveal jets and lobes, providing information about large-scale structures. Infrared observations focus on the dusty torus, which emits strongly and aids in studying core radiation. In the optical range, broad and narrow emission lines from nearby gas and light from the host galaxy are observed. Ultraviolet observations highlight the accretion disk, revealing high-energy processes near the black hole. X-ray observations probe the hot corona and high-energy processes in the innermost regions. Gamma-ray observations detect the most energetic processes in relativistic jets, providing insights into extreme environments.

## 1.7 Thesis outline

This thesis investigates long-period variability in extensive optical sky surveys, a crucial aspect for advancing our understanding of the universe. Periodically variable stars serve as key tools for distance estimation, while periodic variability in AGNs may reveal the presence of binary black hole systems, which are essential for studying gravitational waves. Recent technological advancements and high-precision telescopes now enable us to measure the brightness of distant, faint sources with large accuracy, opening new avenues for exploring long-period sources.

A fundamental challenge in this field is the accurate determination of periods for these sources to ensure true variability is distinguished from aliases or biases. This thesis aims to address this by proposing a robust set of statistical filters that can be applied to achieve a pure sample of long-period sources.

While long-period variability in stars is well understood, periodic changes in AGNs are attributed to various phenomena. In this thesis, the potential role of supermassive binary black holes (SMBBHs) is explored as an explanation for the observed periodicity in a quasar.

In the most recent Gaia DR3, light curves for all of the objects within a 5.5-degree field around the Andromeda Galaxy are provided. Despite the abundance of data, studies of Mira stars in the M31 galaxy using Gaia filters to calibrate their Period-Luminosity (PL) relations have not yet been conducted. The aim of this work is to leverage Gaia's capabilities to establish, for the first time, the PL relations for Mira stars in M31.

This thesis is structured as follows: introduction provides an overview of the research area, objectives, and the content of the work. Following this, the second chapter offers a description of the data used in the research. The third chapter elaborates on the methods employed in the study. Fourth chapter describes the search for long-period objects and identifies candidates for binary supermassive black hole systems. Moving on to the fifth chapter, one of these candidates undergoes detailed analysis. The sixth chapter explains the search for periodically variable red giants in the Andromeda galaxy, along with determining their period-luminosity relations. The final chapter explains the significance of this research in the context of modern astrophysics and suggests potential directions for future studies linked to the dissertation topics.

The key findings of this thesis have been presented in: **Fatović, M.**, Palaversa, L, Tisanić K., Thanjavur K., Ž. Ivezić Ž., Kovačević A. B., Ilić D., and Popović, L. Č. *Detecting Long-period Variability in the SDSS Stripe 82 Standards Catalog*. In: 165.4, 138 (Apr. 2023), p. 138. doi: 10.3847/1538-3881/acb596. arXiv: 2303.04600 [astro-ph.GA]., and one paper in preparation: **Fatović, M.**, Ilić D., Kovačević A. B., Palaversa, L, Simić, S., Popović, L. Č., Thanjavur, K., Razim, O., Ivezić, Ž., Yue, M., and Fan, X. *Complex MgII Time*

*Evolution in SDSS J2320+0024: Clues for a Subparsec Binary Supermassive Black Hole?*”; in prep.

# Chapter 2

## Data

This chapter outlines the data sets that were used in this thesis for analyzing periodic variability in quasars and red giants observed with optical surveys. Specifically, Sections 2.1 and 2.2 provide detailed descriptions of the used photometric and spectroscopic data, respectively.

### 2.1 Photometry

Photometry, a technique in astronomy used to measure the brightness of light emitted from astronomical sources, is vital for understanding periodically variable objects. In this thesis, the focus was on two specific regions of the electromagnetic spectrum: optical photometry, covering approximately 350 nm to 750 nm, and near-infrared photometry, spanning from about 750 nm to about 2 micrometers.

Photometry operates on the principle of collecting and quantifying light. Specialized cameras are used to measure the intensity of photons arriving from an astronomical source within a specific wavelength range or through specific filters.

These cameras are equipped with several key components. The primary light detector is the image sensor, typically a Charge-Coupled Device (CCD). These sensors convert incoming photons into electrical signals, which are then digitized for analysis. Filters are employed to isolate specific wavelength ranges of light, functioning as optical barriers that transmit light within a defined range while blocking other wavelengths. The transmission curves for *ugriz* filters are illustrated in Figure 2.1. These filters are placed in front of the focal plane, as shown in Figure 2.2.

The amount of light entering the camera is controlled by adjustable apertures and the exposure time is regulated by shutters. Typically photometry cameras also incorporate cooling systems to reduce sensor noise, thereby improving the accuracy of measurements.

For the analysis of periodicity described in this thesis, photometric data from the Sloan Digital Sky Survey (SDSS, Blanton et al., 2017), Zwicky Transient Facility (ZTF, Bellm et al., 2019; Graham et al., 2019), Pan-STARRS (PS1, Chambers et al., 2016; Flewelling et al., 2020), Gaia (Gaia Collaboration et al., 2018, 2023a) and The Two Micron All-Sky Survey (2MASS, Skrutskie et al., 2006) were utilized. These surveys are described in detail in the following sections and are represented in Figure 2.3.

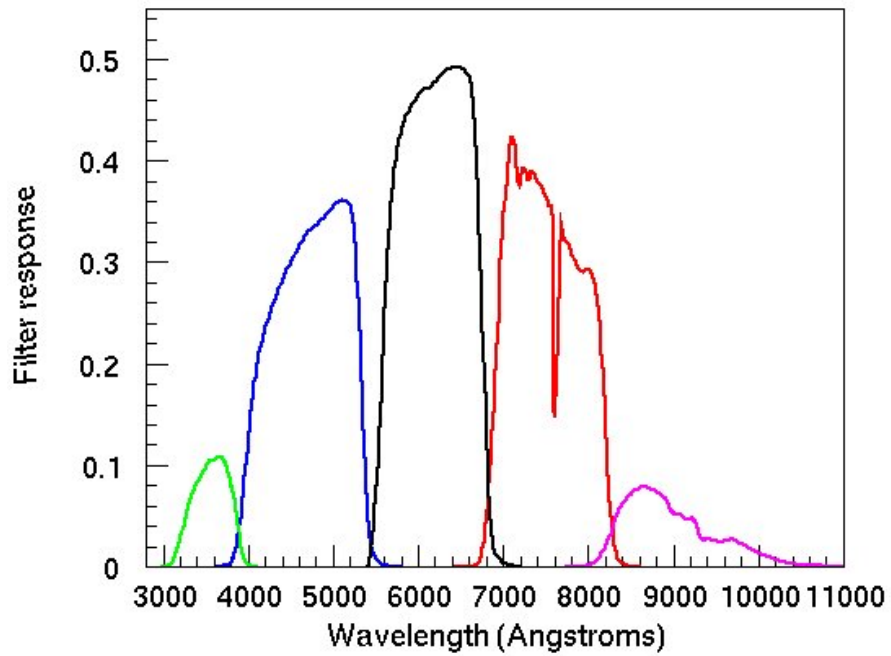


Figure 2.1: An example of the photometric filters: the SDSS-III camera filter throughput curves. Credit: SDSS-III.

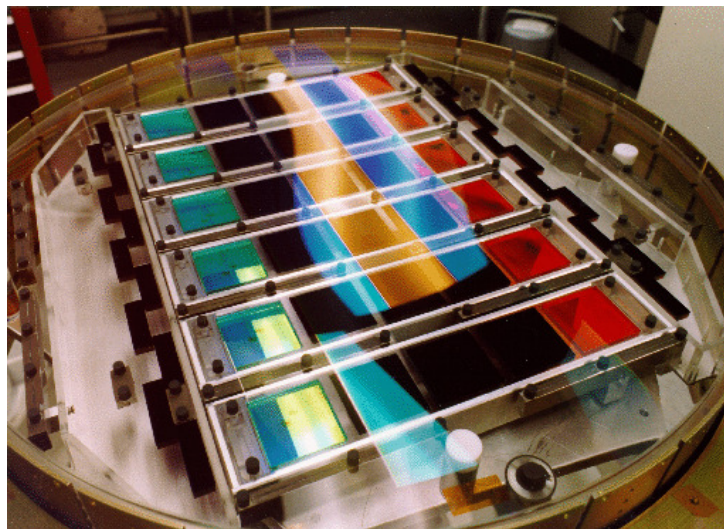
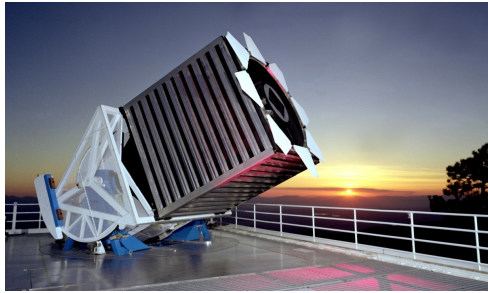


Figure 2.2: The arrangement of the CCDs and filters on the SDSS-III camera. Credit: Gunn et al. (1998)





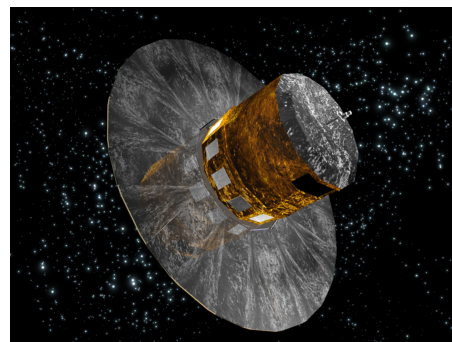
(a) SDSS (New Mexico, USA; image source: SDSS)



(b) ZTF (California, USA; image source: IPAC-Caltech)



(c) PS1 (Hawaii, USA; image source: Space Telescope Science Institute)



(d) Gaia (image source: ESA)



(e) 2MASS (CTIO, Chile; image source: Virtual Observatory)



(f) 2MASS (Fred Lawrence Whipple Observatory, Arizona, USA; image source: Virtual Observatory)

Figure 2.3: The photometric data used in this thesis were obtained from these five surveys.

### 2.1.1 SDSS Stripe 82 photometry

The Sloan Digital Sky Survey (SDSS) is one of the most significant astronomical surveys ever conducted. Its primary mission was the creation of a detailed three-dimensional map of the universe. To accomplish this, SDSS utilized a 2.5-meter telescope located at the Apache Point Observatory in New Mexico, equipped with a large-format digital camera that captured images of the sky in five different optical bands, commonly referred to as the *ugriz* system. These filters covered a broad range of wavelengths which are illustrated in the Figure 2.1.

Throughout its mission, SDSS systematically surveyed large regions of the sky, divided into stripes and patches. One of the largest regions on the sky with multi-band photometry precise to about 0.01 mag, faint limit reaching approximately  $r \sim 22$ , and more than 10 observations per object is a 300 deg<sup>2</sup> region known as the SDSS Stripe 82 (S82, Jiang et al., 2014). Stripe 82 is a region stretching between  $-60^\circ \leq \text{R.A.} \leq 60^\circ$  [20h to 4h], and  $-1.266^\circ \leq \text{Dec} \leq 1.266^\circ$ .

In the initial phase of the research explained in this thesis, SDSS S82 light curve data was used, which had already undergone a thorough screening process to exclude sources that were evidently variable. In the subsequent sections, an overview of the data and the specific catalogs that served as the foundation for this research will be provided.

#### SDSS standard catalog

The SDSS standard star catalog published by Ivezić et al. (2007), hereafter I007, was assembled through the averaging of multiple SDSS photometric observations. Each source in this catalog is represented by a minimum of four observations per band, with a median of ten observations, all conducted within the *ugriz* photometric system. The catalog includes 1.01 million presumably non-variable unresolved objects. The averaged photometric measurements for these individual sources exhibit random errors of less than 0.01 magnitudes. This level of precision holds true for stars brighter than 19.5 in the *u*-band, 20.5 in the *gri*-bands, and 18.5 in the *z*-band, representing a substantial improvement compared to measurements obtained from individual SDSS runs.

The selection criteria for the 1.01 million standard stars within the I007 catalog involved an assessment based on  $\chi_{dof}^2$  (the reduced chi-squared,  $\chi^2$  per degree of freedom), under the assumption of constant brightness. Those exhibiting  $\chi_{dof}^2$  values below 3 in the *gri* bands were considered as non-variable sources. However, approximately 67,000 light curves were excluded from this category, as they displayed evident variability, characterized by  $\chi_{dof}^2$  values exceeding 3 and root-mean-square (rms) variability greater than 0.05 magnitudes, observed in both the *g* and *r* bands. It is important to note that the analysis of such unmistakably variable sources, which predominantly consisted of RR Lyrae stars and quasars, was comprehensively examined

by Sesar et al. (2007) and fell outside the scope of this research.

### Light curve data

Recently, Thanjavur et al. (2021) extended light curves assembled by I007 by incorporating SDSS data collected after the year 2007. The SDSS Data Release 15 (DR15), which was accessible as of April 2019 (Blanton et al., 2017), they proceeded to construct an enriched set of light curves for stars sourced from the standard star catalog. This new dataset boasts nearly twice the number of data points compared to those available to I007, averaging around 20 data points per light curve and extending to 50 in select regions within Stripe 82.

The final dataset, consisting of all the light curves in the five *ugriz* filters for the presumably 1,001,592 non-variable standard stars from the I007 catalog resulted in  $\sim 20$  GB of tabular data. The light curves from this catalog are publicly available<sup>1</sup>.

### 2.1.2 ZTF photometry

The Zwicky Transient Facility (ZTF) is a time-domain survey that uses a 47 deg<sup>2</sup> camera on the Samuel Oschin Telescope at Palomar Observatory to scan the sky for transients and variable sources. ZTF has been in operation since 2017 and has already produced an extensive archive of data that has been used to study a variety of astrophysical phenomena.

In March 2021, ZTF released Data Release 11 (DR11), which includes photometry and lightcurves for over 1.2 billion sources detected by the survey between October 2017 and December 2019. The photometry is measured in the *g*, *r*, and *i* bands, and the lightcurves cover a range of timescales, from minutes to years. The DR11 release is particularly exciting because it includes a number of improvements and upgrades over previous releases. For example, DR11 includes improved image subtraction algorithms that produce cleaner and more accurate lightcurves. The lightcurve data made available in this release is the one that was used in this research.

### 2.1.3 PS1 photometry

The Panoramic Survey Telescope and Rapid Response System (Pan-STARRS) is a project based on a single telescope atop Haleakalā in Hawaii. Its primary goal is to capture detailed images of the entire sky across different wavelengths. Using optical filters, Pan-STARRS divides incoming light into five bands, known as the *grizy* system, covering the optical and near-infrared

---

<sup>1</sup><http://faculty.washington.edu/ivezic/sdss/catalogs/stripe82.html>

spectrum from 475 nm to 960 nm.

In this research, data from the second data release (DR2) of Pan-STARRS was used, specifically the PS1 light curve data. This data was crucial in checking for periodic patterns in previously studied light curves.

### 2.1.4 Gaia photometry

Gaia (Gaia Collaboration et al., 2016, 2023b) is a spacecraft launched 2013 by the European Space Agency (ESA) designed to chart a three-dimensional map of the Milky Way. It consists of two telescopes that continuously scan the sky, capturing high-precision measurements of stellar positions, parallaxes, and proper motions. Gaia's objective is to create a detailed and dynamic map of our Galaxy, which currently includes nearly 2 billion sources.

Gaia observes the sky in three optical filters: G, RP, and BP. The G filter covers a broad range of wavelengths from 330 nm to 1050 nm. The RP filter focuses on the red part of the spectrum, while the BP filter targets the blue part of the spectrum. The transmission curves for all three filters are given in the Figure 2.4. Gaia's limiting magnitude, which defines the faintest objects it can observe, is approximately 20.7 in the G-band.

#### Gaia Andromeda Photometric Survey (GAPS)

The most recent major Gaia data set is Data Release 3 (DR3). In it Gaia provides light curve data for objects classified as variable stars. The upcoming Data Release 4 (DR4), scheduled for late 2025, will include light curves for all observed sources, regardless of their classification as variable or non-variable. As a precursor, DR3 includes all observations and light curves for objects within a 5.5-degree radius around the Andromeda Galaxy (M31). This specific dataset is known as the Gaia Andromeda Photometric Survey (GAPS, Evans et al., 2023).

The GAPS field is strategically chosen because of Gaia's unique scanning patterns in this region, resulting in a number of field-of-view (FoV) transits that is ranging from about 10 to 80. Additionally, the wide 5.5-degree field centered on M31 includes numerous foreground stars from the Milky Way, offering valuable data for comparative studies between the two galaxies.

### 2.1.5 2MASS photometry

The Two Micron All-Sky Survey (2MASS, Skrutskie et al., 2006) is an astronomical survey that mapped the entire sky in three near-infrared wavelengths: J (1.25  $\mu\text{m}$ ), H (1.65  $\mu\text{m}$ ), and K (2.17  $\mu\text{m}$ ). Conducted from 1997 to 2001 using telescopes located in both the Northern and Southern Hemispheres, 2MASS cataloged over 300 million celestial objects.

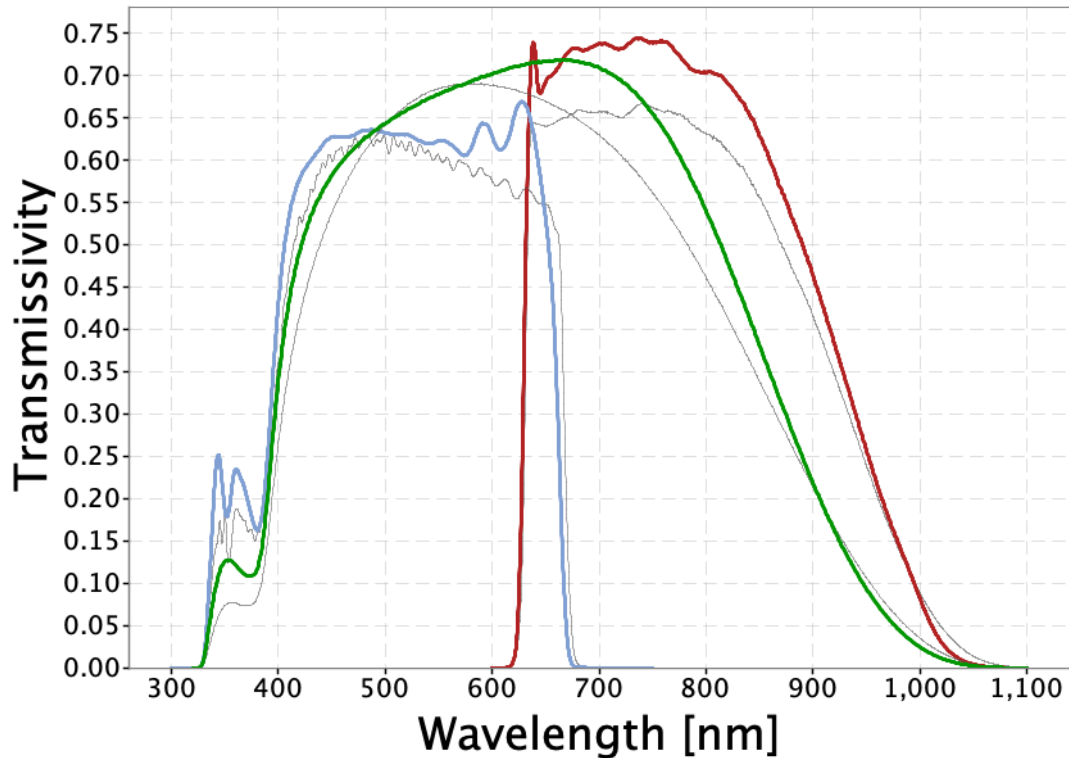


Figure 2.4: Gaia (E)DR3 passbands as produced by Coordination Unit 5 of the Gaia Data Processing and Analysis Consortium. The coloured lines in the figure show the G, BP and RP passbands (green: G; blue: BP; red: RP), defining the Gaia (E)DR3 photometric system. The thin, grey lines show the nominal, pre-launch passbands published in Jordi et al. (2010b), used for Gaia DR1. Credits: ESA/Gaia/DPAC, P. Montegriffo, F. De Angeli, M. Bellazzini, E. Pancino, C. Cacciari, D. W. Evans, and CU5/PhotPipe team.

A significant extension of the 2MASS project, known as 2MASS 6X, involved deeper observations of selected sky regions (Cutri et al., 2012). This extension used exposure times six times longer than the main survey, allowing for data that penetrated approximately one magnitude deeper. Approximately 590 square degrees of the sky were covered in these extended observations, focusing on areas of high astronomical interest, including star-forming regions and nearby galaxies.

The Andromeda Galaxy (M31) was one of the prominent targets in the 2MASS 6X survey. Observations of M31 with 2MASS 6X penetrated dust clouds and revealed intricate components of the galaxy.

## 2.2 Spectroscopy

Spectroscopy is the study of electromagnetic radiation emitted, absorbed, or scattered by astrophysical objects, providing crucial insights into their physical properties. Spectroscopic data allow the identification of the chemical composition, temperature, density, and velocity of stars, galaxies, and other sources. By analyzing the spectra, the presence of various elements and molecules can be determined, and redshift measurements can reveal the movement and distance of galaxies, contributing to the understanding of the expansion of the universe. In the context of this thesis, spectroscopic data were used to investigate the complex behavior of a candidate periodically variable quasar. The Mg II line was observed, allowing conclusions to be drawn about the nature and dynamics of the presumed system. More details can be found in Chapter 5.

### 2.2.1 Spectroscopic observations

Since a part of this thesis consists of spectroscopic data obtained specifically for this work, it is important to explain key points of the spectroscopic observations.

#### Basic spectrograph scheme

Spectrograph is the primary instrument used in spectroscopic observations. The scheme of a simple spectrograph is given in Figure 2.5. The incoming light first travels from a telescope through a small opening in the spectrograph, called a slit. A slit is there to control and limit the amount of light that enters the spectrograph. It is important in the context of eliminating unwanted light, spatial resolution (how effectively can the details be resolved) and spectral resolution (how good can closely spaced wavelengths or spectral lines be distinguished). After it passes the slit, the light comes to a collimating mirror. Collimated light consists of rays that are parallel and have minimal or no divergence, meaning they do not converge or spread apart. That collimated beam then reaches a finely scored plate of glass known as a diffraction grating. It is a device with a surface that contains a large number of closely spaced, parallel slits or grooves. These cause diffraction of incoming light into its constituent colors which then allows separate and analysis of the individual wavelengths. By rotating the diffraction grating, it is possible to control wavelengths reach another mirror, which in turn focuses these wavelengths onto a CCD. Converted electrical signals are then interpreted by computer to measure the strength of different wavelengths.

While preparing for the observations, one of the most important things is to decide on the exposure time of the scientific target. The exposure is the duration for which the detector

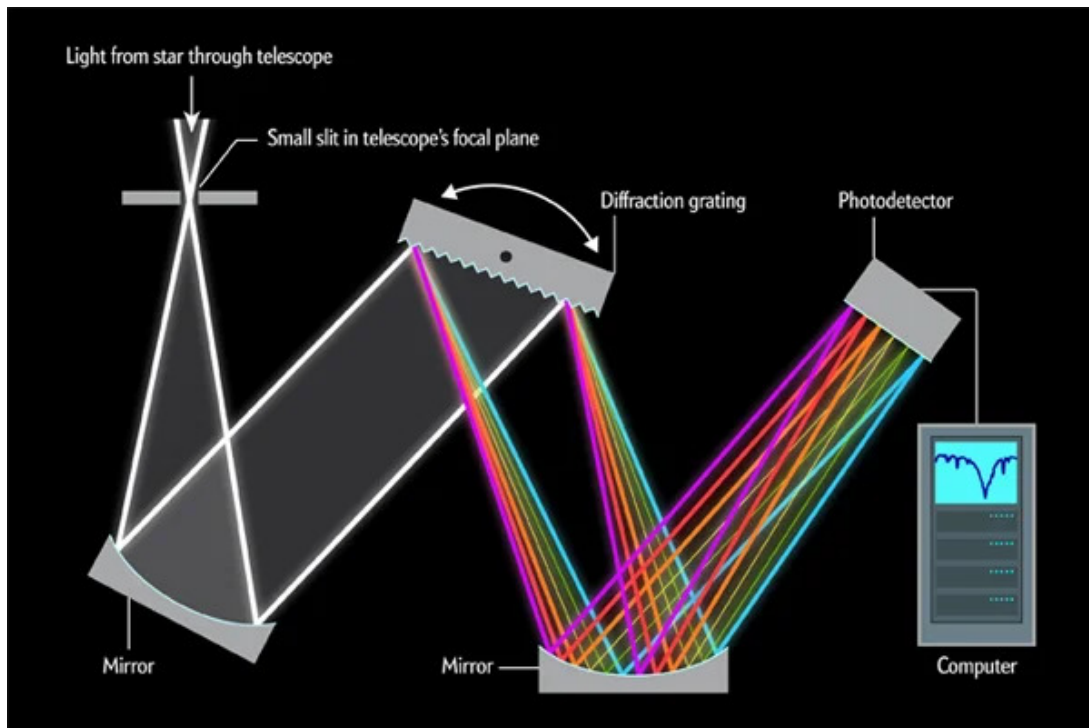


Figure 2.5: A simple scheme of a spectrograph. Credit: Illustration by George Retseck

collects photons from the target. It depends on factors such as the object's brightness, the desired signal-to-noise ratio, and the spectrograph's configuration. Longer exposures capture fainter details but may introduce saturation for bright sources.

The resulting set of the observation data consists of the science data, arc lamp data, standard star observations, bias frames and flat fields. Here I will explain what are all these data and how are they used.

The science frames consist of the observations of the science target in the duration of the previously determined exposure time. The number of the observations is determined by the time allocated on the telescope.

The calibration sources like arc lamps or known standard stars used for accurate wavelength calibration and flux calibration. Arc lamps, such as mercury, helium, or neon lamps, emit known spectral lines at precise wavelengths. By comparing observed spectral lines with those from the arc lamp the spectra can be accurately wavelength calibrated.

Standard stars are sources with well-known spectra and fluxes. They are observed under the same photometric conditions as the certain science target, to establish a reference for flux calibration. Absolute flux scale of the observed spectra can be determined by comparing the observed flux of a standard star to its known flux.

Bias frames are images taken with the spectrograph's shutter closed and no light entering the system. They are used to measure the electronic noise characteristics of the detector and are subtracted from the science frames to correct for detector bias.

Flat-field frames are used to correct for variations in pixel sensitivity across the detector. They are typically taken by imaging a uniformly illuminated source, such as a twilight sky or a flat-field lamp. The resulting frames help correct for non-uniform illumination and detector imperfections.

This raw data is to be reduced and calibrated before making them useful for science analysis. The processing of the data is explained in the Chapter 3.

### 2.2.2 Gemini and Magellan observations

The source of interest was a SDSS S82 quasar with a plausibly periodic behaviour explained in detail in Chapters 4 and 5. This part of the sky is visible every year from late summer till mid-winter. Getting the time for the observations of this source in year 2022 was of the specially great importance since it was visible during the time the calculated periodic variability indicated to be in its photometric maximum. Why is this important will be more clear after reading the Chapter 5. For now it is important to list some of the specificities of this source like the redshift of  $z=1.06$  and SDSS median  $r$  band magnitude of  $r \sim 21.3$  mag.

The observations of the MgII emission line of the targeted quasar were conducted in November and December of 2022 with Gemini and Magellan telescopes respectively. In the following text I will describe specifications of the observations characteristic for both telescopes. Both telescopes are given in the Figure 2.6.

#### Gemini: GMOS-S

The Gemini Observatory consists of twin 8.1-meter diameter optical/infrared telescopes located in both North and South hemisphere. From their locations on mountains in Hawai'i and Chile, Gemini Observatory's telescopes can collectively access the entire sky.

Our observations were conducted using the Gemini South Observatory's Gemini Multi-Object Spectrograph (GMOS-S), located in Cerro Pachon in Chile. Observations were taken on November 14th, 2022 and used longslit (1.0 arcseconds) spectroscopy with the R831 grating whose efficiency is shown in the Figure 2.7. The 2.2 hours of directors' discretionary time resulted with a total of 6x1100 seconds science exposure with central wavelengths being altered between 650 nm, 655 nm, and 660 nm, due to the gaps between the GMOS CCDs. The observations were conducted using the Hamamatsu CCD detector with spatial and spectral binning





(a) Gemini (Cerro Pachon, Chile; image source: Gemini Observatory)



(b) Magellan Telescopes (Las Campanas Observatory, Chile; image source: Wikipedia)

Figure 2.6: The spectroscopic observations were conducted with these two telescopes.

of 2x4, and the standard star LTT3218 was used along with a CuAr lamp arc for calibration.

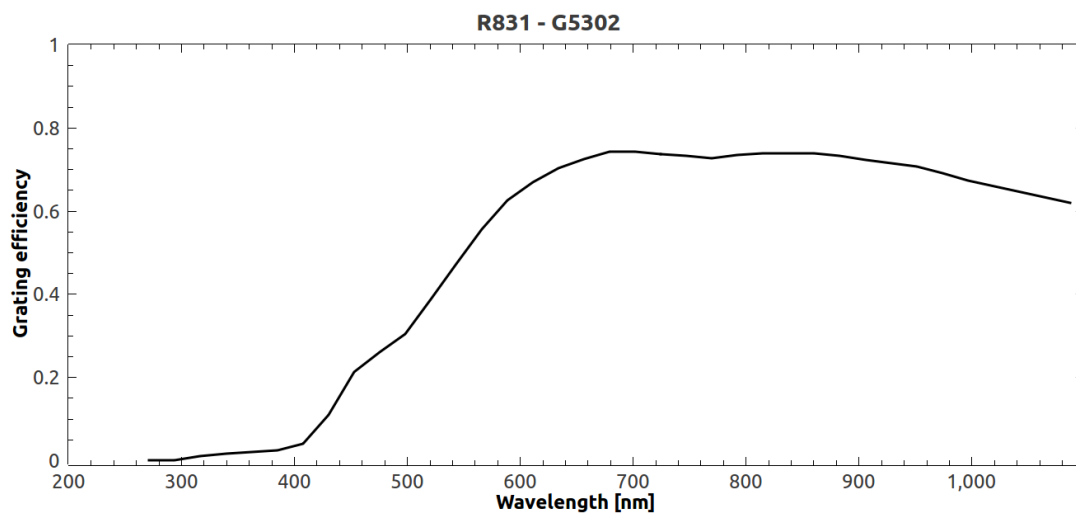


Figure 2.7: Grating efficiency for R831. Author: Inger Jorgensen, Created: 15 Feb 2001.

### Magellan: LDSS-3

The twin Magellan Telescopes are 6.5 optical telescopes located at the Las Campanas Observatory in the Chilean Andes. The observation was carried out using the Low Dispersion Survey Spectrograph (LDSS-3) on December 22nd, 2022 during the astronomical twilight.

Three consecutive integrations of 1ks were selected in order to reduce the effect of the accumulated cosmic rays and potential instrumental and atmospheric noise sources. The combination

of VPH Blue grism<sup>2</sup> and a 1.0 arcsecond slit was employed. The binning was set to 1x1 (in the spatial and spectral directions) with the slit angle aligned with the average position angle (PA) of the target object.

### 2.2.3 SDSS spectroscopy - eBOSS

For this research, data provided by the SDSS's Extended Baryon Oscillation Spectroscopic Survey program (eBOSS, Dawson et al., 2012, 2016a) were used.

The eBOSS program is a part of the fourth phase of the Sloan Digital Sky Survey (SDSS-IV), aimed at mapping the large-scale structure of the universe. It focuses on obtaining high-quality spectra of distant galaxies and quasars to measure the expansion history of the universe through the Baryon Acoustic Oscillations (BAO) feature.

Observations for eBOSS were carried out using the 2.5-meter Sloan Foundation Telescope located at the Apache Point Observatory in New Mexico, USA. The telescope is equipped with a pair of dual-channel spectrographs that cover a wavelength range from 360 nm to 1040 nm. Each spectrograph is capable of observing up to 1000 objects simultaneously, thanks to its multi-fiber optical system.

The eBOSS survey targeted several classes of objects, including luminous red galaxies (LRGs), emission line galaxies (ELGs), and quasars. These observations provided a comprehensive dataset for studying the distribution of matter in the universe, the nature of dark energy, and the growth of cosmic structures.

---

<sup>2</sup>The VPH Blue Grism is optimized for the blue region of the spectrum, typically covering wavelengths from around 3600 to 6300 Å.

# Chapter 3

## Methods

This chapter summarizes the methods used to obtain the results in this research. It covers period determination and filtering procedure, spectral analysis of AGNs, and the calibration of the PL relation.

### 3.1 Period determination

One of the greatest challenges in studying periodically variable sources is determining their period. Various methods have been proposed to address this issue, including Fourier analysis, wavelet analysis, Lomb-Scargle periodogram and others (all nicely summarized in VanderPlas, 2018).

Another challenge is determining whether the calculated period is a genuine period of a source or simply an alias caused by the Earth's rotation and revolution around the Sun or other technical factors related to the telescope used for observation.

#### 3.1.1 Lomb - Scargle periodogram

The Lomb-Scargle periodogram is a widely used tool in astrophysics for detecting periodic signals in unevenly sampled time series data. It was introduced by Lomb (1976) and later independently by Scargle (1982). The periodogram provides a measure of the likelihood of a periodic signal with a given period being present in the data.

Given a time series  $y_i$  with measurements taken at times  $t_i$ , the Lomb-Scargle periodogram computes a power spectral density  $P(f)$ , which is a function of frequency. The Lomb-Scargle periodogram is defined as:

$$P(f) = \frac{1}{2\sigma^2} \left[ \frac{(\sum_{i=1}^N (y_i - \bar{y}) \cos(2\pi f(t_i - \tau)))^2}{\sum_{i=1}^N \cos^2(2\pi f(t_i - \tau))} + \frac{(\sum_{i=1}^N (y_i - \bar{y}) \sin(2\pi f(t_i - \tau)))^2}{\sum_{i=1}^N \sin^2(2\pi f(t_i - \tau))} \right], \quad (3.1)$$

where  $\bar{y}$  is the mean value of the data,  $N$  is number of data points,  $\sigma^2$  is the variance of the data and  $\tau$  is a time offset parameter given as:

$$\tau = \frac{1}{2\pi f} \arctan \left( \frac{\sum_{i=1}^N \sin(4\pi f t_i)}{\sum_{i=1}^N \cos(4\pi f t_i)} \right). \quad (3.2)$$

The Lomb-Scargle periodogram can be used to identify the period of a periodic signal in the data by searching for peaks in the power spectrum. The height of a peak in the periodogram indicates the strength of the periodic signal with the corresponding period. However, care must be taken in interpreting the significance of peaks in the periodogram, as the power spectrum can be affected by noise and aliasing effects.

### Astropy's implementation of Lomb-Scargle periodogram

In this thesis, the Lomb-Scargle periodogram (Press & Rybicki, 1989) as implemented in *astropy* (Astropy Collaboration et al., 2013, 2018) was utilized. This implementation allows users to specify a custom frequency grid for period calculations, providing flexibility in determining the spacing at which periods are calculated. Additionally, it offers an *autopower* method that automatically adapts the grid spacing. The frequency grid is a set of discrete frequencies at which the periodogram is evaluated, and its selection is crucial because it impacts the resolution and accuracy of period detection.

The *autopower* method takes user-defined minimum and maximum frequencies and adjusts the grid spacing based on the observations of the source and the length of the observational baseline. This method ensures that five grid points are allocated for each significant peak detected in the periodogram, optimizing the accuracy and efficiency of the period detection process.

Additionally, an implemented model is provided by this method for the plotting of the LC model, with the possibility of including higher terms in the model:

$$y(t; f, \vec{\theta}) = \theta_0 + \sum_{n=1}^{\text{nterms}} [\theta_{2n-1} \sin(2\pi n f t) + \theta_{2n} \cos(2\pi n f t)]. \quad (3.3)$$

Including higher terms is often preferable, as certain periodically variable sources exhibit more complex periodic behavior.

### 3.1.2 2D Hybrid method

Random fluctuations significantly account for the variance in time series, with greater stochastic effects observed over longer periods. The spectral density of red noise, being inversely related to frequency, greatly impacts lower frequencies. To address this, a time-domain periodicity search method called the 2D hybrid method was applied. This method relies on various types of wavelets described in Kovačević et al. (2018, 2019).

Wavelet matrices (scalograms)  $S$  and  $S'$  of two-time series  $y_t$  and  $y'_t$  are compared to check for similar patterns. The 2D hybrid method uses correlation to compare scalograms (Kovačević et al., 2020a). Various wavelets, including continuous, discrete weighted wavelet Z-transform (WWZ, Foster, 1996), high-resolution superlets (Moca et al., 2021), and both observed light curves and their models, are employed.

A contour map of the intensity of autocorrelation on a period-period plane was generated. This plane is defined by two independent period axes matching the two time series (or one). The map is symmetric and can be integrated along any axis, producing a periodogram-like curve showing the strength of correlation among oscillations. For more details, see Kovačević et al. (2018, 2019).

The significance of a detected period  $\sigma_P$  was calculated by shuffling the time series (Johnson et al., 2018), allowing the period to be recomputed over this new modified data set. The height of the maximum peak in the 2D hybrid integrated map was then compared to that found for the original simulated data. This process was repeated  $N$  times (e.g., 100, as per the wavelet computation), and the significance level was subsequently determined (Johnson et al., 2018):

$$\sigma_P = \frac{x}{N}, \quad (3.4)$$

where  $x$  represents the number of times the peak power of the period in the original data exceeded that of the uncorrelated ensemble.

Another approach for estimating significance, based on the moving block bootstrap (MBB) methodology (Ivezić et al., 2014; VanderPlas, 2018), was also used. In the MBB approach, blocks of data of a given length are glued together to create a new time series. Similarly to the shuffling method, periods of bootstrapped mock light curves were first calculated. Then, the generalized extreme value (GEV) distribution was fitted to the histogram of detected peaks in the mock curves. For a given range of significance levels ( $p$  values), the associated confidence level was obtained from the fitted GEV. If the candidate period had a peak value greater than the confidence level, the null hypothesis that the observed light curve is not periodic was rejected at the given significance level.

### 3.1.3 Monte - Carlo simulations

This method is described in the paper in preparation: Tisanić, K. et. al.

The simulations were based on the best-fitting Lomb-Scargle periodogram light curve model implemented in *gatspy* (VanderPlas & Željko Ivezić, 2015). This model describes magnitudes  $m$  observed at time  $t$  and in band  $b$ , denoted as  $m(t, b)$ . Each mock observation,  $i$ , consisted of a simulated point:  $(t_i, b_i, m_i, \sigma_{m,i})$ .

Instead of using a simple bootstrap method, the Gaussian kernel density estimator (KDE) was employed to determine the distributions of  $t$ ,  $m$ , and  $\sigma_m$ . This approach enabled the generation of mock light curves with the same number of points as the original data set. It was assumed that the data points were independently distributed among the different bands, with each band appearing the same number of times in the mock light curve as in the original data.

To accurately reproduce the magnitude error distribution, it was determined that estimating  $\log \sigma_m$  using KDE yielded better results compared to estimating the KDE of  $\sigma_m$ . The magnitudes at specific mock times were computed by fitting the multiband Lomb-Scargle function to the initial dataset, allowing the prediction of values at mock times for a randomly selected band. To these predicted values, the simulated error value  $\sigma_m$  was added.

This process was iterated over 1000 random light curves per object, with the number of mock times set to match the observing times in the original light curves. For each mock dataset, the *gatspy* multiband periodogram was executed to estimate the reliability of the resulting periods. The standard deviations of the period distributions were determined using a robust approach, specifically utilizing the 16th and 84th percentiles of the simulated period distributions. Based on these estimated sigma values and the periods calculated using the *astropy* implementation of the Lomb-Scargle periodogram, as described in Section 3.1.1, the corresponding P-values were computed. In instances where certain standard deviations were smaller than one day, the standard deviations used for P-value computation were capped at 0.1 days.

Based on the outcomes derived from this approach, an additional filter was implemented on the sample. This filter required that the previously computed periods must align with those generated through this method within the associated uncertainty range ( $|P - P_{\text{gatspy}}| < \sigma_P$ ).

## 3.2 Statistical methods of filtering calculated periods

The calculated periods may not accurately reflect the actual periods of the source due to potential contamination caused by biases or aliases. Biases can originate from technical factors associated with the telescope, as well as natural rotational occurrences like the Earth's revolution around the Sun. Meanwhile, aliases can result in different calculated periods being associated with the same source. To minimize the presence of false periodicity, employing a collection of statistical filters is the most effective approach. These filters are designed to identify and exclude groups of periods that are influenced by biases, thus improving the accuracy of the analysis.

### 3.2.1 $\chi^2$ and periodogram relation

One way to check how well the light curve data agree with the light curve model is by calculating  $\chi^2$ . The fact that there is a connection between  $\chi^2$  and the power of the Lomb-Scargle periodogram was used, and previously calculated  $P_{LS}$  was employed in the following way:

$$P_{LS} = 1 - \frac{\chi_{per}^2}{\chi_{const}^2}. \quad (3.5)$$

Values  $\chi_{per}^2$  and  $\chi_{const}^2$  were calculated as:

$$\chi_{per}^2 = \sigma_G(x_{per})^2, \text{ where: } x_{per} = \frac{mag - model}{magErr}, \quad (3.6)$$

$$\chi_{const}^2 = \sigma_G(x_{const})^2, \text{ where: } x_{const} = \frac{mag - \langle mag \rangle}{magErr}. \quad (3.7)$$

The function  $\sigma_G(x) = 0.7413 \cdot (x_{75} - x_{25})$ , which is the normalized interquartile range of the observed source magnitudes, was used. A requirement was set that  $P_{LS} > 0.5$ . This means that an improvement of the  $\chi^2$  by a factor of 2 was required.

### 3.2.2 Phase distribution analysis and Kuiper statistics

Additional analysis was proceeded with under the requirement that each potential candidate should display an evenly spread-out arrangement of observations when considering its phase. This condition was introduced based on the assumption that it is unlikely that for a significant fraction of the observed sources the cadence of the survey will be matched to the period of a particular source in a way that would produce observations always near the same point (or a few

points) within the phased light curve. Considering the consistent and uniform cadence maintained across all S82 observed fields, a significant abundance of objects with closely clustered observations within the phased light curve would suggest that these objects share a common frequency denoted as  $f_c \in f/n$ , where  $f$  signifies the object's period, and  $n$  represents a small integer. It is important to note that the application of this condition might result in the exclusion of some potentially valid candidates. However, since higher priority was placed on the quality and purity of the sample rather than achieving completeness, any source whose phase-folded light curve exhibited clustered observations was flagged as a false positive and consequently excluded from further analyses. This filtering was performed using Kuiper's statistics. Kuiper statistics, named after the Dutch-American astronomer Gerald Kuiper, measure whether a set of data is uniformly distributed around a circle. The Kuiper statistic aids in deciding if a pattern is uniform by providing a number that represents how much the data differ from a uniform distribution. This statistic compares an empirical cumulative distribution function defined on a circle with the expected cumulative distribution function for a uniform distribution ( $CDF(x) = x$ ). The maximum deviations are given as:

$$D = \max(CDF_{data} - CDF_{unif}) + \max(CDF_{unif} - CDF_{data}). \quad (3.8)$$

The probability of observing the calculated D value due to random fluctuations in a uniform distribution was computed. When this probability is found to be very low, it leads to the conclusion that the phase coverage is not uniform. Consequently, the corresponding period is discarded. The D percentage for a uniform distribution is dependent on the sample size, N:  $D\% = \frac{C}{N^p}$ . In this case, for a 99.9% threshold,  $C = 2.04$  and  $p = 0.486$  were employed. These values were determined by fitting this mathematical expression to numerical simulations involving draws from uniform distributions of various sizes, falling within the range  $8 < N < 10^4$ . This relationship holds true within the range of  $0.95 < D\% < 0.999$ . Subsequently, only those sources that had D values smaller than  $D_{99.9\%}$  for each of the *gri* bands were retained.



## 3.3 Analysis of the quasar spectra

In Chapter 5, spectral analysis was utilized to study the quasar with which changes in the shape of the Mg II emission line were observed. From these analyses of the Mg II emission line, drawing conclusions about the kinematics of the quasar itself was possible.

### 3.3.1 Data reduction and calibration

Before scientific analysis, observed spectra must be reduced and calibrated. This section provides a general summary of the procedure involved required to obtain scientific-grade data for the submitted and published papers. Most instruments have standard procedures built in for processing raw data, which include all specificities related to each individual telescope and its observation methods.

The first step in the data reduction process is bias subtraction. Bias frames, which are zero-exposure images taken with the shutter closed, represent the electronic noise of the detector. To correct for this noise, each science and calibration frame is corrected by subtracting a master bias frame, created by taking the median of several bias frames.

Next, flat fielding is performed. Flat frames, which are images of a uniformly illuminated entrance pupil of an imaging system, are used to correct for pixel-to-pixel sensitivity variations. The science frames are divided by flat fields. This step ensures that the variations in pixel sensitivity do not affect the scientific data.

After flat fielding, cosmic ray removal is necessary. High-energy particles can create bright spots in images, which need to be removed. Algorithms such as median filtering and sigma clipping are used to detect and remove these cosmic ray artifacts. This ensures that the resulting spectra are free from these spurious signals.

The two-dimensional (2D) spectrum extraction follows. The position of the spectrum is traced<sup>1</sup> along the spatial direction to correct for any distortions or curvatures. Once traced, the spectrum is extracted by summing the pixel values along the spatial direction within a defined aperture around the traced position. This step converts the 2D data into a one-dimensional (1D) spectrum for each spatial position along the slit.

Wavelength calibration is performed using arc lamp calibration. Arc frames are exposures of a calibration lamp (such as neon or argon) with known emission lines. These emission lines in the arc spectrum are identified and matched with their known wavelengths. A polynomial

---

<sup>1</sup>An aperture is the defined region around the traced position from which pixel values are summed. Tracing involves following the spectrum's position along the spatial direction to correct distortions or curvatures. This ensures accurate extraction of the 1D spectrum.

fit, typically of the second or third order, is applied to the identified lines to establish a wavelength solution. This wavelength solution is then applied to the science spectra, converting pixel positions into wavelengths.

Flux calibration starts with the observation of standard stars. These spectrophotometric standard stars have well-known flux distributions. The observed spectrum of the standard star is corrected for atmospheric extinction using an extinction curve appropriate for the observatory site. By comparing the observed flux of the standard star with its known flux, a sensitivity function is derived, representing the instrumental response and atmospheric transmission. This sensitivity function is then applied to the science spectra, converting instrumental counts to absolute flux units.

The final steps include sky subtraction and the combination of multiple exposures. A region of the slit without the target object is used to extract the sky spectrum. This sky spectrum is subtracted from the science spectrum to remove sky background emission. Multiple exposures of the same target are aligned (in wavelength and spatial direction) and co-added to increase the signal-to-noise ratio. Finally, the calibrated 2D spectrum is summed along the spatial direction to produce a 1D spectrum for detailed analysis.

The Gemini data were reduced and calibrated with the official Gemini DRAGONS pipeline (Labrie et al., 2019). The Magellan spectrum was processed with the standard pipeline PypeIt (Prochaska et al., 2020b; Prochaska et al., 2020a).

### 3.3.2 Shifting Quasar Spectra to the Rest Frame

When observing a quasar, its spectral lines appear at wavelengths longer than their rest-frame values due to the redshift  $z$ . The observed wavelength  $\lambda_{\text{obs}}$  relates to the rest-frame wavelength  $\lambda_{\text{rest}}$  by:

$$\lambda_{\text{obs}} = (1 + z)\lambda_{\text{rest}}, \quad (3.9)$$

### 3.3.3 Spectral Analysis in Velocity Space

Analyzing spectra in velocity space is particularly useful for studying the kinematics of gas around quasars.

The velocity  $v$  associated with a given observed wavelength  $\lambda$  relative to a reference rest wavelength  $\lambda_0$  (the central wavelength of an emission - in the case presented in this thesis - Mg II) is calculated using the Doppler formula:

$$v = c \left( \frac{\lambda - \lambda_0}{\lambda_0} \right), \quad (3.10)$$

where  $c$  is the speed of light.

### 3.3.4 Mass estimation

The Mg II line is one of the best UV lines for SMBH mass measurements, used for high-redshift quasars (e.g., Popović et al., 2019; Vestergaard & Peterson, 2006; Lira et al., 2018; Woo et al., 2018). The used relation between SMBH mass, luminosity at 3000 Å ( $L_{3000}$ ), and Mg II FWHM are given by:

$$M_{BH} \sim (L_{3000})^{0.5} \cdot FWHM_{MgII}^2, \quad (3.11)$$

often presented as:

$$\log(M_{BH}) = \alpha + \beta \cdot \log(L_{3000}) + \gamma \cdot \log(FWHM_{MgII}), \quad (3.12)$$

where  $\alpha = 1.15 \pm 0.27$ ,  $\beta = 0.46 \pm 0.08$ , and  $\gamma = 1.48 \pm 0.49$ , with  $M_{BH}$  in  $10^6 M_{\odot}$ ,  $FWHM_{MgII}$  in  $10^3 \text{ km s}^{-1}$ , and  $L_{3000}$  in  $10^{44} \text{ erg s}^{-1}$  (Wang et al., 2009; Popović, 2020).

### 3.3.5 PoSKI model

To model SMBBHs that can describe the observed variability and complex Mg II line shape, several configurations of SMBBHs were explored by varying the mass ratio and dynamical parameters while fixing the periodicity. The variability in the broad Mg II line shape suggests the presence of a component without shift changes and another component with shifting changes. This led to the use of the Popović, Simić, Kovačević, Ilić model (PoSKI, Popović et al., 2021) model with a specific configuration: two SMBBHs, where one is significantly larger ( $q \sim 0.1$ ), and only the smaller component has a broad line region (BLR) within its Roche lobe, moving with the component. Both components have accretion discs that illuminate the gas around both SMBBHs, forming a circum-binary BLR. It was assumed that the more massive component lacks sufficient ionized gas in its Roche lobe to form its own BLR, possibly due to the smaller component clearing the material around the larger one. Using this configuration, the observed Mg II line profile was qualitatively fit, and the observed periodicity in the continuum was reproduced.

An orbital period was acquired from the observational data, providing basic constraints on the component masses and their separation. For such a defined system, the orbital velocities are too high, resulting in significant line shifts that are not detected in the observations. Therefore, the inclination angle was reduced to a very low value, and the emission from the SMBBH was computed almost in a face-on orientation. Additionally, since the observations from Gemini

and Magellan were taken close in time and the light curve showed minimal variation, further constraints on the eccentricity and the orbital plane's orientation toward the observer were established. Due to the asymmetric deviation in the MgII line, a low mass ratio binary system with  $q = 0.1$  was proposed.

The parameter values used in the simulation are as follows:  $m_1 = 2 \times 10^7 M_\odot$ ,  $m_2 = 2 \times 10^8 M_\odot$ ,  $R = 0.0025$  pc,  $ecc = 0.1$ ,  $incl = 10^\circ$ ,  $accesion\_node = 140^\circ$ ,  $roche\_ratio = 0.87$ . The phases for particular observations are:  $t_{SDSS} = 0.02P_{orb}$ ,  $t_{Gem} = 0.53P_{orb}$ ,  $t_{Mag} = 0.7P_{orb}$ .

To achieve a satisfactory fit, the magnitude of the MgII line from the smaller component was artificially increased. The correction factors are  $c_{SDSS} = 1$ ,  $c_{Gem} = 1.3$ , and  $c_{Mag} = 1.4$ . This adjustment is justified by variations in mutual component interactions, which are significant due to the very close component separation and the eccentric orbits.

### 3.3.6 Calculation of the synthetic magnitudes

The calculation of synthetic magnitudes from an observed spectrum involves integrating the spectral flux over the transmission function of the desired filter, in this case, the SDSS  $r$  filter. The synthetic magnitude provides a measure of the apparent brightness of an object as it would appear through the specific filter.

The synthetic magnitude  $m_r$  in the SDSS  $r$  filter is derived using the observed flux spectrum  $f(\lambda)$  and the filter transmission function  $T_r(\lambda)$ . The monochromatic flux  $f(\lambda)$  is given in units of flux density. The transmission function  $T_r(\lambda)$  describes the transmission efficiency of the SDSS  $r$  filter at different wavelengths and is dimensionless.

The flux through the filter is calculated by integrating the product of the observed flux and the filter transmission function over the wavelength range of the filter. The synthetic flux  $F_r$  is given by:

$$F_r = \frac{\int f(\lambda)T_r(\lambda)\lambda d\lambda}{\int T_r(\lambda)\lambda d\lambda} \quad (3.13)$$

This integration normalizes the flux by the effective width of the filter. The synthetic magnitude  $m_r$  is then calculated using the standard formula for magnitudes:

$$m_r = -2.5 \log_{10} \left( \frac{F_r}{F_0} \right) \quad (3.14)$$

where  $F_0$  is the reference flux for the  $r$  filter, often taken from a standard star or a known flux reference.

### 3.4 Calibration of Period-Luminosity relation

In the Introduction, the distance determination using periodically variable stars and their PL relation was already briefly explained, but in this Section the more extensive explanation is provided. An example of the procedure of obtaining the distance to some X galaxy using the periodically variable stars is given in the Figure 3.1. The first step is to choose a type of

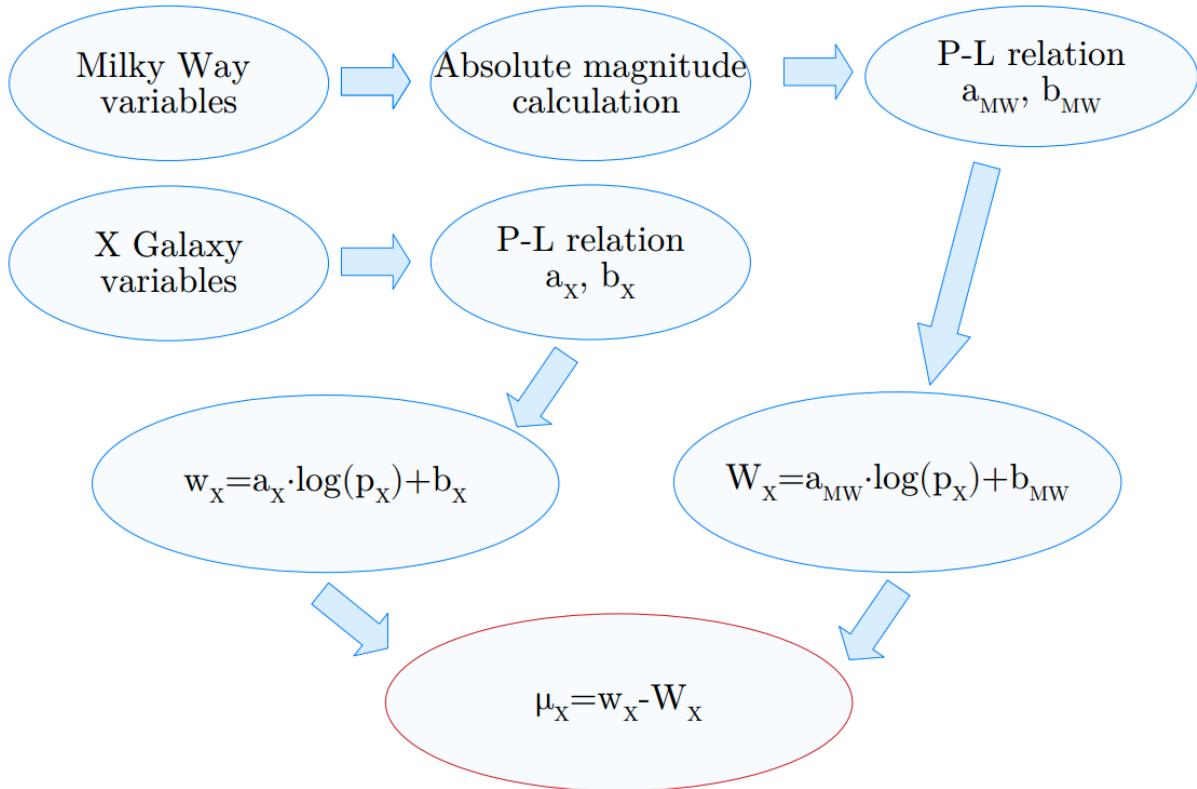


Figure 3.1: An algorithm of calibration procedure of PL relation. This example is related to calculation of the distance to the arbitrary X galaxy.

periodically variable stars, such as Miras, from our Galaxy. Then, using the observed magnitude and measured parallax, calculate the absolute magnitude of that star. Then, calculate the period and determine the coefficients of the PL relation. The obtained coefficients are then used to calculate an absolute magnitude of the same type of stars in the target galaxy. Once we have the PL of the apparent magnitude and the absolute magnitude, it is possible to calculate the distance modulus to that galaxy. Distance modulus  $\mu$  is:

$$\mu = m - M. \quad (3.15)$$

The PL relation can also be employed to detect and identify variable stars within a galaxy by analyzing their periods and luminosities. Different types of periodic stars create distinct ridges on the PL diagram. This method is specifically used to identify Mira stars in the research presented in this thesis.

## Chapter 4

# Detecting long - period variability in the SDSS Stripe 82 standards catalog

The primary reason for the scarcity of research in long period variables is the lack of suitable observational data. To investigate such variability, extensive requirements must be met: a long observational timeline, high photometric precision, and broad sky coverage. While several surveys partially fulfill some of these prerequisites, none combine them as comprehensively as SDSS's time-domain survey in the S82 region (discussed in detail in Section 2.1.1). This survey not only has superior photometric precision and depth (reaching as faint as  $r \sim 22$  mag) compared to surveys like (LINEAR, Stokes et al., 2000; Palaversa et al., 2013), Palomar Transient Factory (PTF, Law et al., 2009), Gaia, and ZTF but also offers more observational epochs in the *gri* bands on average than PS1 and the Dark Energy Survey (DES, Dark Energy Survey Collaboration et al., 2016). Apart from SDSS S82, only two other surveys, the Optical Gravitational Lensing Experiment (OGLE, Udalski et al., 1997; Udalski, 2003) and Kepler (Ciardi et al., 2011), provide a suitable environment for studying sources with a few percent change in brightness. The disadvantage of OGLE over SDSS is that OGLE focuses primarily on the inner Galactic bulge and the Magellanic Clouds, whereas SDSS covers a more extensive timespan and a broader portion of the sky compared to Kepler.

In this search for periodic changes within S82, an unbiased method was used. Instead of focusing on specific types of changes, the long observational history of S82 was used to find any kind of long-term variability. This included various possibilities, such as sources within our Galaxy and those outside it.

Galactic long-period candidates include multiperiodic, semi-regular variable red stars, such as the OGLE Small Amplitude Red Giants (OSARGs) (Wray et al., 2004), and potentially binary stars with edge-on orbits exhibiting nearly sinusoidal light curves. Mira stars also fell

within the period range of interest, but their substantial amplitude variations excluded them from our analysis, as large amplitude sources were already tagged in the S82 data by previous studies (see Section 2.1.1). Among extragalactic long-period variable candidates in this sample were quasars exhibiting periodic optical light curve variations. Explanations for this behavior included phenomena like radio jet precession (e.g. Kudryavtseva et al., 2011), tilted (warped) accretion disks (e.g. Tremaine & Davis, 2014), tidal disruption events (e.g. Liu et al., 2014), supermassive binary black hole systems (e.g. Graham et al., 2015b; Valtonen et al., 2008; Liu & Gezari, 2018) and others.

The results presented in this Chapter were published as Fatović et al. (2023) : *Detecting Long-period Variability in the SDSS Stripe 82 Standards Catalog*, 2023, AJ, 165, 138. doi:10.3847/1538-3881/acb596.

## 4.1 Period calculation and filtering

As explained in Section 3.1, one of the most significant challenges in the study of periodically variable sources lies in accurately determining their periods. This research project was centered around addressing this issue by introducing a range of filtering methods to identify genuine long-period variable candidates within a sample that was initially presumed to comprise solely non-variable sources. Despite the commitment to an entirely unbiased search, the anticipated outcome was a final sample primarily composed of long-period sources characterized by small amplitudes.

In this study, primary focus was on ensuring the purity of the final sample, prioritizing this aspect over completeness. In this study, the purity of the final sample was prioritized over completeness. To achieve this goal, a rigorous filtering approach was implemented, comprising a series of meticulous statistical filtering steps.

### 4.1.1 Number of data points

A sample of 1,001,592 light curves was initially considered (see Section 2.1.1). From this, a subset of 143,505 light curves with at least  $N = 25$  observational epochs was selected after filtering out epochs with likely spurious photometry. Epochs were excluded if their *gri* magnitude was outside the range of 11 to 23 mag, if they had unrealistically small photometric errors (less than 0.0001 mag), or if their photometric errors were larger than 0.2 mag.



### 4.1.2 Lomb-Scargle period agreement

For the work described in this chapter, the implementation of the Lomb-Scargle periodogram from *astropy* (see Section 3.1.1) was utilized. The *autopower* method was employed to determine the grid spacing, minimizing computational effort given the substantial number of initial sources. The input frequencies used were  $f_{min} = 1/600 \text{ days}^{-1}$  and  $f_{max} = 1/2 \text{ days}^{-1}$ . The upper boundary of the period search was capped at 600 days to reduce computational load, while the lower limit was set at 2 days. This decision was influenced by the fact that periods shorter than 1 day are typically associated with variable stars that have been extensively examined in previous studies of the SDSS S82 region. Additionally, periods around  $P \approx 1 \text{ day}$  are often affected by aliasing, so the lower limit was increased by a factor of 2.

The *gri* bands, which typically display the most favorable photometric signal-to-noise ratios, were the focus for calculating periodograms. To prevent occasional instances of unrealistically small reported errors, a systematic photometric error of 0.01 mag was added in quadrature to the photometric uncertainties reported by the SDSS photometric pipeline.

Within each individual band, periods corresponding to the three most prominent peaks in the periodogram were retained. This approach provided greater flexibility in assessing the potential impact of aliasing on the observed signal, as incorporating more than three peaks often results in capturing noise rather than real signals.

Out of the nine periods calculated for each source, light curves displaying plausible periodic variability were selected based on the requirement of having at least one common period across all three *gri* bands, with a tolerance level of 0.1%. This criterion was implemented to eliminate unreliable cases and focus on consistently periodic behavior. This resulted in 1,078 sources with 2,135 corresponding periods.

### 4.1.3 Agreement with the model

To assess the agreement between the data and the simple sinusoidal model, the  $\chi^2$  method, as described in Section 3.2.1, was applied. This filtering resulted in 342 sources with 601 corresponding periods.

### 4.1.4 Dealing with repeated periods and filtering out aliases

In the sample of 342 sources with 601 periods, numerous repeated periods were observed. The period histogram is shown in Figure 4.1.

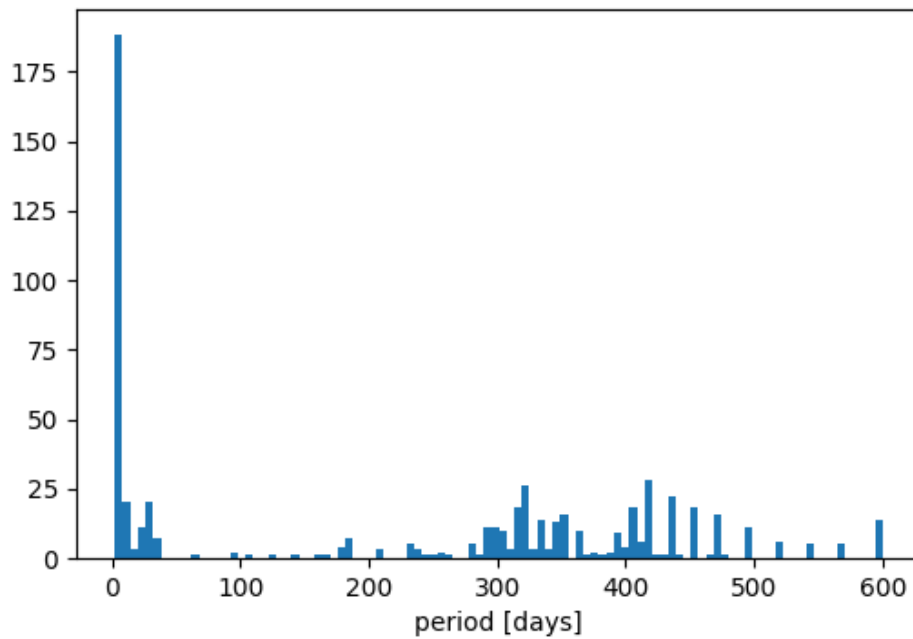


Figure 4.1: Histogram of periods for 342 sources with 601 corresponding periods.

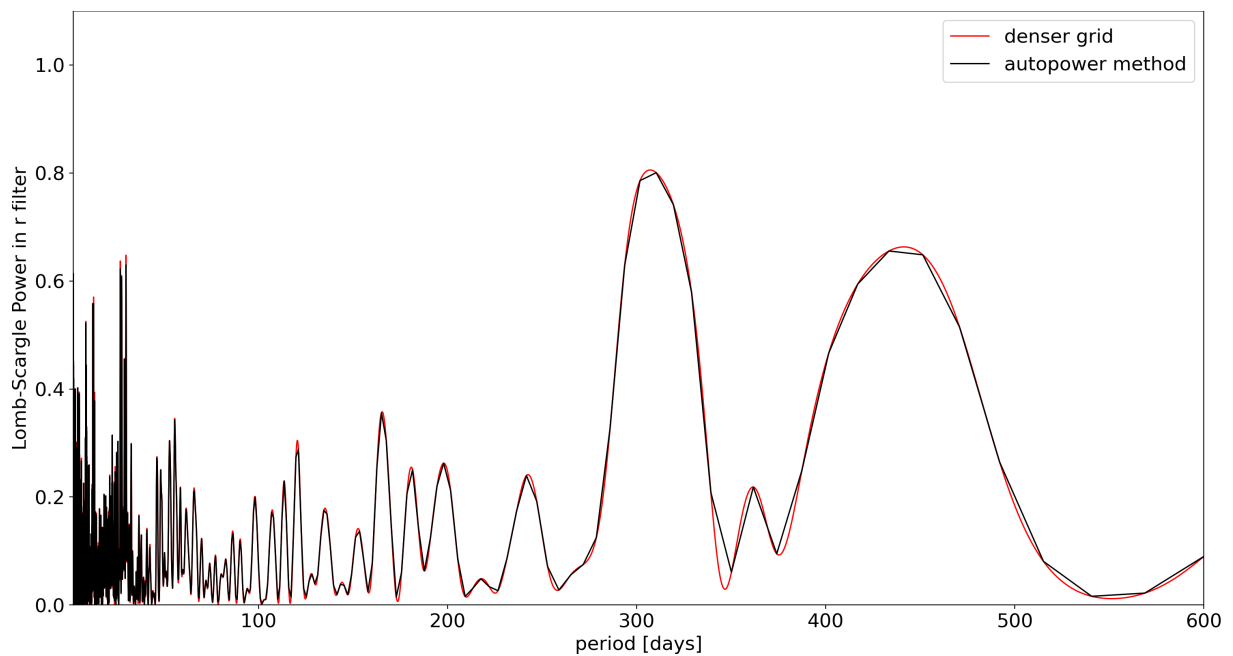


Figure 4.2: A typical example of a Lomb-Scargle periodogram for a candidate variable. The figure shows periodograms obtained using the *autopower* method and a denser grid.

It was suspected that these repeating periods could be aliases. However, it was also possible that certain genuine periods were overlooked due to the coarse nature of the grid, influenced by the *autopower* method used in the Lomb-Scargle routine. To explore the implications of utilizing a denser grid in period calculations, a new Lomb-Scargle period search was conducted on a grid with higher density. Given the reduction in dataset size (now: 342, before: 143,505), this adjustment did not require substantial computational resources. The frequency range remained consistent ( $f_{min} = 1/600 \text{ days}^{-1}$ ,  $f_{max} = 1/2 \text{ days}^{-1}$ ), but the grid was configured as follows: for periods ranging from 2 to 8 days, a time spacing ( $\Delta t$ ) of 1 minute was used; for periods between 8 and 32 days,  $\Delta t$  was set to 3 minutes; for periods from 32 to 128 days,  $\Delta t$  was 10 minutes; and for periods spanning 128 to 600 days,  $\Delta t$  was 1 hour. By comparing the outcomes of both period estimation runs, it was confirmed that no significant peaks in the periodogram were overlooked in the run with the less dense search grid.

Figure 4.2 presents a comparison between the periodograms derived from a denser grid and those using the *autopower* method. Evidently, there is no notable distinction between the two.

All clustered periods that could fit within a 0.1-day bin were excluded. Given that these periods exhibit agreement within this narrow time range, it is plausible that they represent aliases. Consequently, 69 sources with a total of 82 periods remained. For more focused analysis on long periodicities, only objects with periods exceeding 100 days were retained. This constraint left 45 unique objects with 58 corresponding periods. This threshold was chosen to focus exclusively on longer-period variations. Additionally, Figure 4.1 illustrates that periods within the range of up to 100 days predominantly cluster around smaller values, often near zero. This pattern likely results from the 1-day aliasing caused by Earth's rotation. As the catalog underwent a cleanup process, removing all short-period variable sources, such sources were not factored into this study.

#### 4.1.5 Implementation of Kuiper metric

As described in Section 3.2.2, the primary objective of this study was to obtain a pure sample of long-term periodicities. Consequently, it was required that the phased light curve (PLC) be free of gaps and data clusters. This filtering process resulted in a sample of 28 sources with 33 corresponding periods.

#### 4.1.6 Characterization of Sources

To better characterize the list of periodically variable candidates, color-color and color-magnitude diagrams, as shown in Figure 4.3, were used. The clustering pattern observed in the upper left

panel of the diagram inspired the introduction of four distinct subgroups, detailed in Table 4.1. Each source within these subgroups was uniquely identified by assigning an ID based on its specific position in the  $g$  vs.  $u - g$  plot, as shown in Figure 4.3.

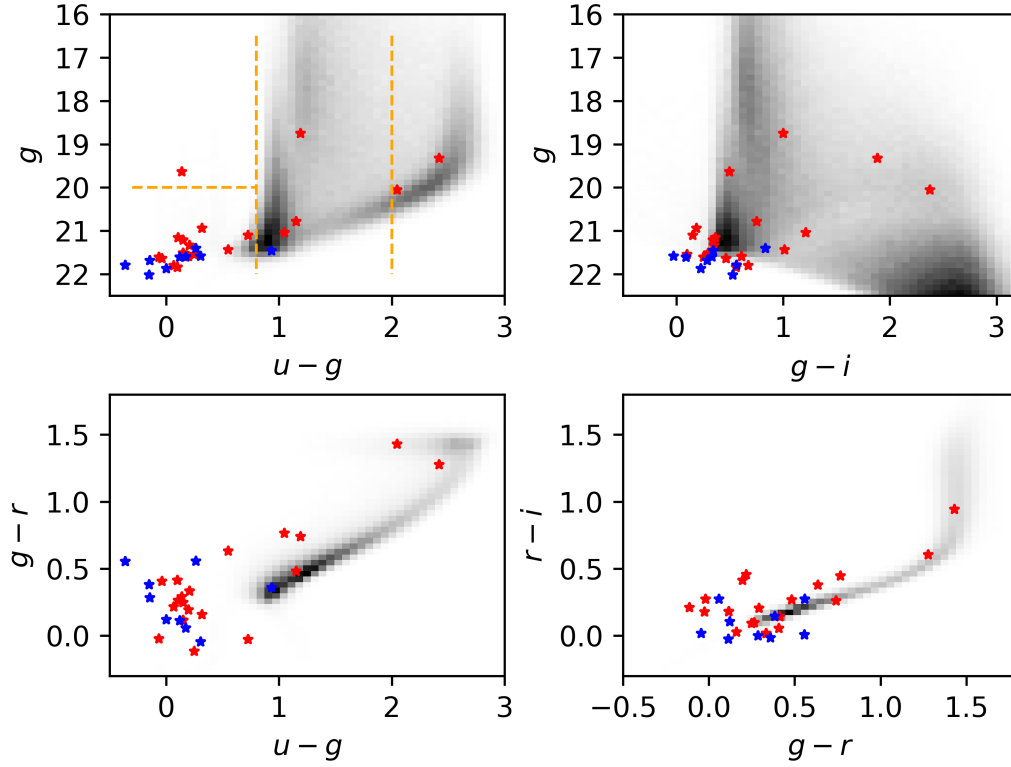


Figure 4.3: Color-magnitude and color-color diagrams for 28 candidates remaining after the Kuiper statistics filter. Sources with period  $P < 365$  days are plotted as red and those with  $P > 365$  days are plotted as blue symbols. The gray background represents the distribution of all objects from the standards catalog.

Table 4.1: The division of the sample in 4 subgroups. Using the logic of this partition, new names for each source, which are given in column ID, were introduced.

Regions	Types	ID
<i>i</i> ) $u-g > 2.0$	“late-type” K and M stars	0-1
<i>ii</i> ) $0.8 > u-g > 2.0$	“intermediate-type” F and G stars	2-5
<i>iii</i> ) $u-g < 0.8$ and $g < 20$	quasars; possible presence of stars	6
<i>iv</i> ) $u-g < 0.8$ and $g > 20$	quasars	7-27

### 4.1.7 Comparison with MC simulations

The periods were required to align with those generated through the MC method explained in Section 3.1.3 within the associated uncertainty range ( $|P - P_{\text{gatspy}}| < \sigma_P$ ). This effectively narrowed down the sample to 9 sources, corresponding to a total of 10 distinct periods.

### 4.1.8 Dealing with one-year period aliases

As a final filter, the calculated periods were evaluated to determine whether they were real signals or merely one-year aliases. The following equation was used:

$$P_a = 365 \pm \frac{k}{n} \cdot 365; \quad k = 1, 2; \quad n = 1, 2, 3, 4, 5. \quad (4.1)$$

This equation was employed to detect any indications of periods that could be aligned with yearly aliases. The previously calculated period  $P$  was considered within a specific range around the value of a year (365 days), taking into account the period's uncertainty, denoted as  $\sigma_P$ , which was derived through Monte Carlo simulations (explained in detail in Section 3.1.3). If a calculated period fell within the range of  $P \pm \sigma_P$ , it was categorized as an alias linked to a one-year cycle. The application of this filtering criterion led to a refined group of 5 sources exhibiting periodic variability with 6 corresponding periods.

### 4.1.9 Additional checks

Additional checks were employed to account for the possibility of visually obvious deficiencies in the phenomena.

#### Examining SDSS Images

To address the possibility that observed changes in magnitude might be attributed to nearby sources, an analysis of SDSS cutouts for each of the five identified final sources was conducted. Through a visual examination of these images, it was confirmed that none of the candidates were subject to blending effects.

#### Examining more recent light curves

To investigate the behavior of the light curves of each source at times different from those of the SDSS observations, the analysis was extended to include databases from other surveys. Among these, ZTF DR11 and PS1 were identified as valuable sources of light curve information for

the final 5 candidates. This approach involved the simultaneous plotting of light curves from SDSS, ZTF, and PS1 databases, each corresponding to their respective filters, along with the SDSS-based model.

It was required that the apparent variability be confirmed in at least one filter for at least one of the additional surveys at later times.

The confirmation of apparent variability across all 5 sources significantly reduced the likelihood that the original SDSS data were faulty or that the detected periodic variability arose from random fluctuations.

#### 4.1.10 Summary of the filters used

The summary of the filters applied in the selection procedure is provided here. The process began with an initial set of 1,001,592 light curves.

- at least  $N = 25$  observational epochs  $\rightarrow$  143,505 sources
- each of the *gri* periods agree to within 0.1%  $\rightarrow$  1,078 sources with 2,135 corresponding periods
- $\chi^2$  and  $P_{LS} > 0.5$  analysis  $\rightarrow$  342 sources with 601 corresponding periods
- "repeated" periods ( $\Delta P = 0.1$  days) and periods  $100 \text{ days} < P < 600 \rightarrow$  45 sources with 58 corresponding periods
- Kuiper statistic:  $D < D_{99.9\%} \rightarrow$  28 sources with 33 corresponding periods
- comparison with Monte-Carlo results  $\rightarrow$  9 sources with 10 corresponding periods
- one-year period alias  $\rightarrow$  5 sources with 6 corresponding periods

Additional checks:

- blending  $\rightarrow$  no sources were discarded
- comparison to more recent light curves  $\rightarrow$  no sources were discarded



## 4.2 Results

Each of the five final sources has phased light curves with a uniform distribution of data points along the light curve, is well isolated from other sources and has (periodic) variability at later times supported by either ZTF or PS1 survey data. The figures summarizing light curves of each of the sources, along with SDSS photometry cutouts are given in following section.

### 4.2.1 Representative figures of final candidates

Each figure contains:

- Left column: SDSS cutouts described in Section 4.1.9,
- Middle column: light curves in *ugriz* bands with light-curve model derived using SDSS data. In addition to SDSS data, ZTF and PS1 data are also plotted in the figure as described in Section 4.1.9. To account for the difference between the instruments, a magnitude correction was applied to each of the *gri* filters:

$$SURVEY_{corr} = SURVEY + \langle SURVEY \rangle - \langle SDSS \rangle, \quad (4.2)$$

where  $SURVEY_{corr}$  is the corrected magnitude, i.e. magnitude shifted by the median difference between the survey in question and the SDSS ( $\langle SURVEY \rangle - \langle SDSS \rangle$ ).

In certain instances, a few data points from the ZTF and PS1 datasets are not visible within the figures due to their significant deviation from the model light curve. To maintain a convenient scale for the plots, these outlier values were excluded from the plot's ordinate range. Instead, they were represented using color-coded arrows on the left-hand side of some panels within the middle column. The length of these arrows ( $l$ ) correlates with the number of data points ( $N$ ) lying outside the ordinate range, calculated as  $l = N \cdot 0.05 + 0.03$ .

Furthermore, given the ZTF's shallower limiting magnitudes compared to Pan-STARRS and SDSS (approximately 20.5 mag), which result in larger scatter at the fainter end of the ZTF data, a binning approach was implemented. The ZTF data were divided into 7-day intervals, and a weighted mean magnitude was computed for each bin. This binning strategy was employed to enhance photometric precision and improve the overall clarity of the plots.

- Right column: phased light curves in *ugriz* bands.



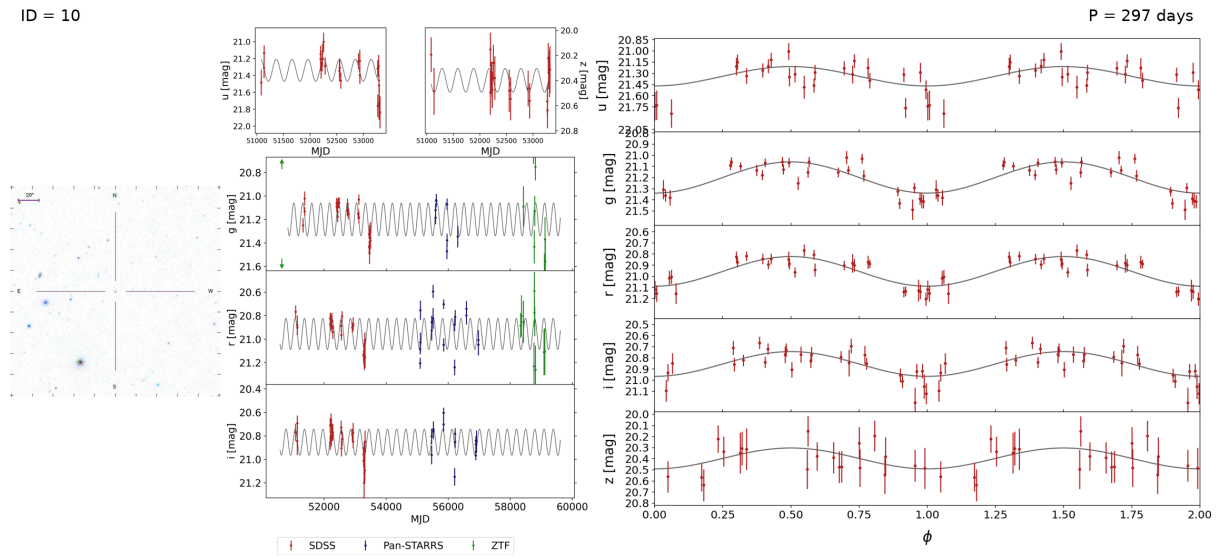


Figure 4.5: ID = 10. The variability of this source at later times can not be excluded with PS1 data. ZTF data are too noisy to give definitive arguments.

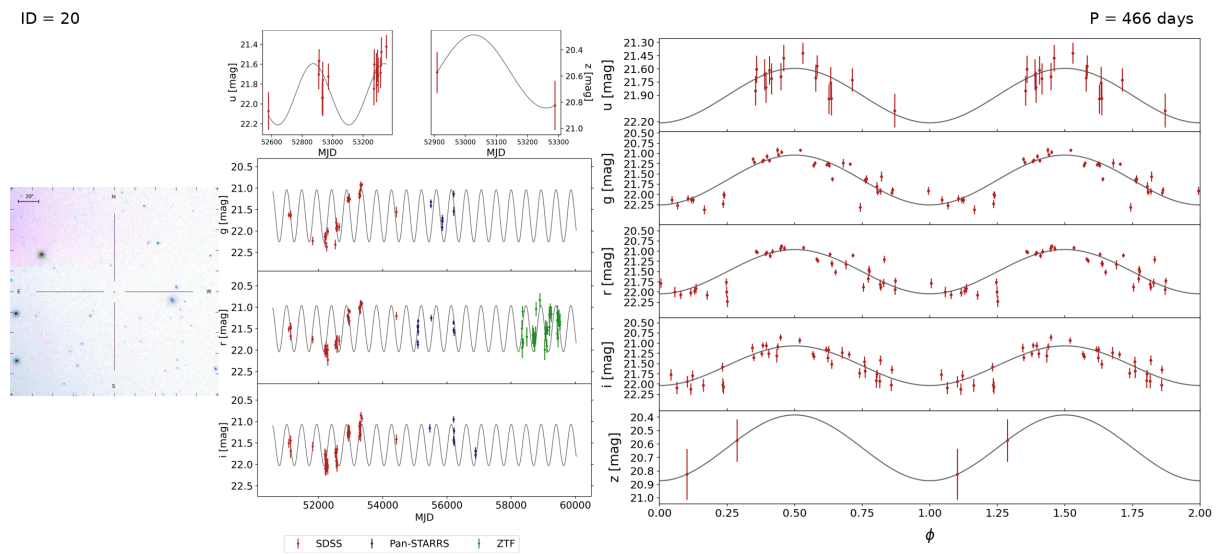


Figure 4.6: ID = 20. This source has a confirmation of the variability both from ZTF (only in  $r$  band) and from PS1 ( $gri$  bands). Also, the possibility of periodicity cannot be ruled out.

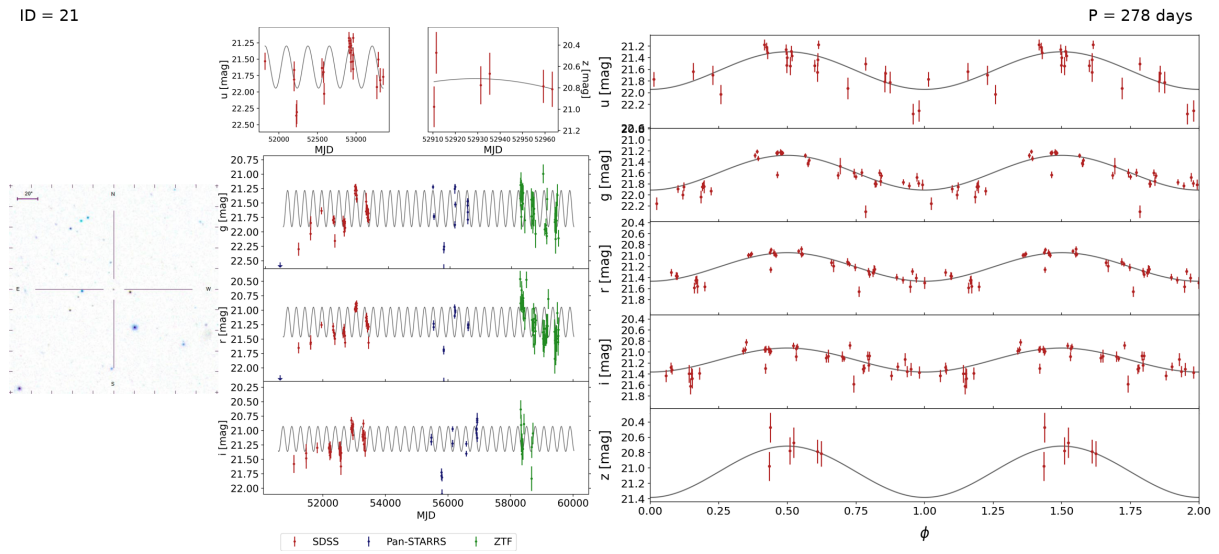


Figure 4.7: ID = 21. Although there is a lot of noise in the ZTF data, the observations at later times can not rule out periodical variability of this source. PS1 has fewer data points, but it still shows variable behavior.

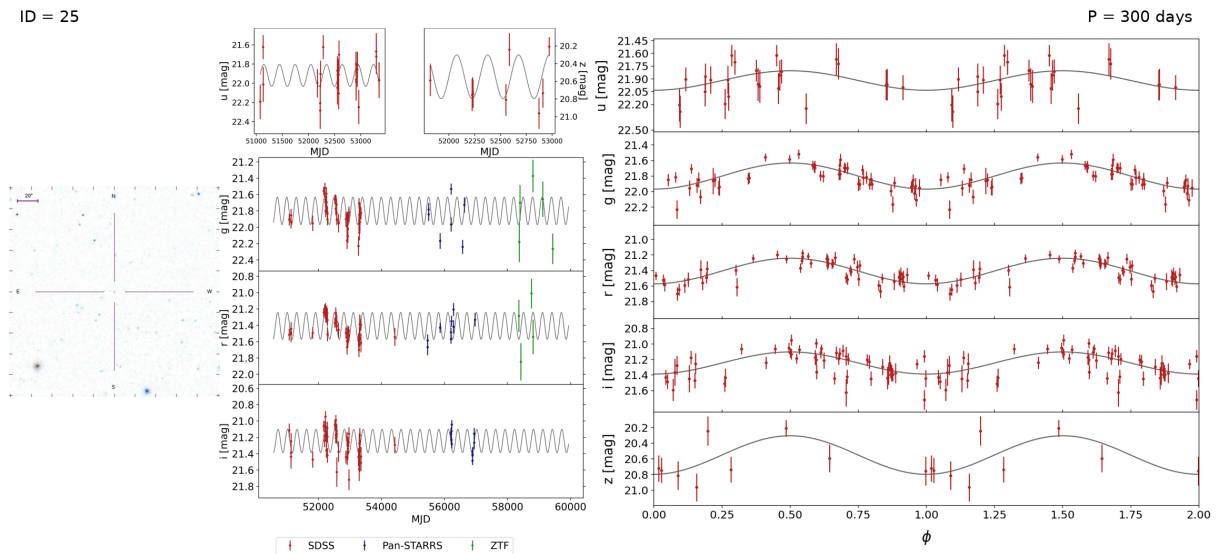


Figure 4.8: ID = 25. Due to too few points and too much noise, it is not possible to conclude anything about the ZTF, but PS1 data show variable behavior.

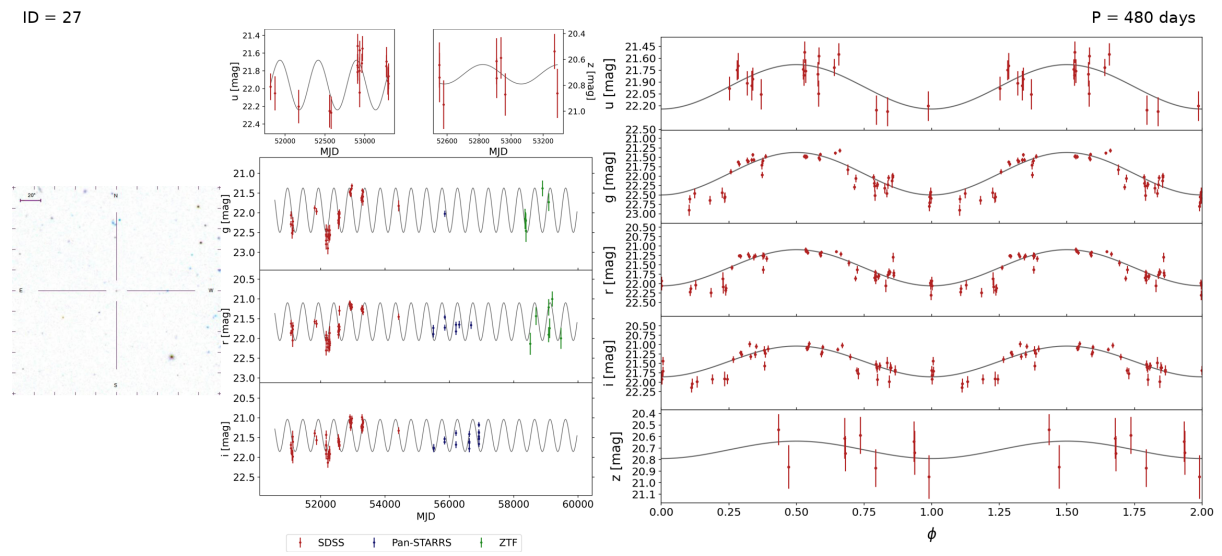


Figure 4.9: ID = 27. ZTF data in  $gr$  bands can not rule out the possibility of periodic behavior for this source at later times. PS1 data are inconclusive or show lower amplitude variability.

### 4.2.2 Table of final candidates

The Table 4.2 is representing the final 5 long-period candidates. The column explanation is given here:

- objID: SDSS DR9 object ID,
- ID: ID given on the basis of the position of an object in color-magnitude diagram described in Table 4.1,
- ra / dec: coordinates,
- period: calculated period of a source (in days),
- $u/g/r/i/z$ : weighted mean of magnitude in each filter,
- $u-g/g-r$ : mean colors,
- $\text{Amp}(g/r/i)$ : the difference between the maximum and minimum of the sinusoidal model.

Table 4.2: Table of 5 long-period variability candidates.

objID	ID	ra	dec	period	u	g	r	i	z	u-g	g-r	Amp(g)	Amp(r)	Amp(i)
1237666338651242745	10	14.629833	-0.622042	297.1988	21.30	21.18	20.93	20.84	20.4	0.12	0.25	0.28	0.27	0.22
1237666338653864147	20	20.57287	-0.422368	466.3183	21.69	21.39	21.26	21.36	20.68	0.30	0.13	1.22	1.08	0.97
1237666408438038843	21	350.059098	0.416449	277.8278	21.45	21.51	21.13	21.08	20.76	-0.06	0.38	0.63	0.52	0.44
1237663783133970736	25	23.53744	-0.839078	299.7779	21.90	21.79	21.38	21.21	20.58	0.11	0.41	0.34	0.33	0.29
1237666300553068800	27	44.539858	-0.206044	479.5917	21.81	21.73	21.43	21.32	20.71	0.08	0.30	1.13	0.96	0.82

### 4.2.3 The results of Monte Carlo simulations

Here are presented the results of Monte Carlo simulations based on the *gatspy* multiband algorithm used to infer the reliability of the *astropy*-based period-finding procedure. After the *gatspy*-derived period for each source has been determined, the set of 1000 mock lightcurves was produced, as described in detail in Section 3.1.3. The mock observations were simulated by estimating the underlying time, magnitude, band and magnitude error distributions from the KDE fit to the real observations. Each mock light curve was then fitted using the same *gatspy* algorithm, yielding a set of mock sample periods. The derived distribution of mock sample periods was used to infer the error bars on the expected period - the expected *astropy*-based period calculated, as described in Section 4.1.2. The columns in the Table 4.3 show the following:

- ID: ID given on the basis of the position of an object in color-magnitude diagram described in Table 4.1,
- $\sigma_P$ : error bars estimated using Monte Carlo simulations,
- expected period: calculated period of a source (in days) as described in Section 4.1.2,
- *gatspy* period: best-fitting period (in days),
- simulated period: mean period derived using Monte Carlo simulations (in days) ,
- expected P-value ( $\sigma \rightarrow \max(\sigma, 0.1d)$ ): P-values using a capped sigma for the expected period,
- *gatspy* P-value ( $\sigma \rightarrow \max(\sigma, 0.1d)$ ): P-values using a capped sigma for the *gatspy* period.

Table 4.3: Results of Monte Carlo simulations of the sample’s periods.

ID	$\sigma_P$	expected periods	<i>gatspy</i> period	simulated period	expected P-value ( $\sigma \rightarrow \max(\sigma, 0.1d)$ )	<i>gatspy</i> P-value ( $\sigma \rightarrow \max(\sigma, 0.1d)$ )
10	2	297	296	296	0.66	0.99
20	2	466	467	466	0.73	0.56
21	1	278	278	278	0.60	0.99
25	2	300	302	302	0.21	0.92
27	3	480	479	478	0.45	0.56

### 4.3 Discussion

The substantial uncertainties associated with ZTF photometry preclude definitive conclusions for sources with IDs 10 and 25. However, PS1 photometry adequately confirms variability in at least one of the bands.

Source ID 10, depicted in Figure 4.5, exhibits the smallest amplitude ( $A \sim 0.2$  mag) among all final candidates. Source ID 25, shown in Figure 4.8, is notable for having two reported periods that meet the selection criteria ( $P_1 = 300$  days,  $P_2 = 299$  days). Since these periods fall within the uncertainty range specified in Table 4.3 ( $|P_1 - P_2| < \sigma_P$ ), it is reasonable to conclude that both methods recover the same period, approximately 300 days.

Sources ID 20 and 27, observed in Figure 4.6 and Figure 4.9, respectively, demonstrate robust periodic variability confirmation, supported by both ZTF and PS1 data. Additionally, these figures illustrate that the ZTF amplitudes do not exclude the SDSS-based model as incorrect.

A particularly intriguing quasar within this sample is ID 21 (Figure 4.7), which exhibits a period of  $P = 278$  days. In addition to the optical variability detected in this study, this source also has a Chandra X-ray catalog variability flag set to 1 (indicating flux variability within or between observations in one or more energy bands) (Evans et al., 2010). For this source, an additional analysis of its periodicity was conducted using the 2D hybrid model outlined in Section 3.1.2. By applying the 2D hybrid method, whose core is the WWZ, a period of  $278.36^{+57.34}_{-25.21}$  days was obtained. The significance was measured to be above 99% using the shuffling method, while the GEV approach produced a significance of 90%. To apply the 2D hybrid method with the high-resolution superlets core, homogeneous data were required. Therefore, observed light curves were modeled with the deep Gaussian process (see e.g., Damianou & Lawrence, 2013), consisting of a latent variable layer and two Gaussian process layers. The Gaussian processes utilized Matern<sub>12</sub> and Matern<sub>32</sub> kernels. The detected period was  $288.62^{+28.84}_{-07.35}$  days, with a significance of 95% based on the shuffling method and 88% based on the MBB. The results indicated excellent agreement between this period and the period calculated using the method explained in Section 4.1.2.

## 4.4 Chapter summary and conclusions

This study primarily focuses on the search for periods and the development of filtering method aimed at uncovering long-period phenomena that might have been overlooked by existing optical surveys. Initially, the expectations revolved around identifying long-period, small-amplitude stars in the final sample. However, contrary to this assumptions, five strong candidates displaying periodic variability were identified. All five of these candidates have been spectroscopically confirmed as quasars.

Understanding the underlying causes of variability in these candidates is not possible without additional data. Therefore, a one quasar (ID=21) with a period of  $P = 278$  days was singled out. Its periodic variability remained unexcluded by ZTF and PS1, and it also displayed X-ray variability as detected by Chandra. To further investigate the nature of this variability and potentially enhance the approach to photometrically detecting such exotic sources, new spectra of this source were obtained through two additional surveys: Gemini GMOS-S and Magellan LDSS3. This subsequent phase of the study is detailed in the following chapter of this thesis.



## Chapter 5

# Complex MgII Time Evolution in SDSS J2320+0024: Clues for a Subparsec Binary Supermassive Black Hole?

In the previous chapter, five quasar candidates exhibiting periodic variability were introduced. Various potential explanations for this phenomenon were discussed in Section 1.5.2. The candidate with the shortest period of 278 days was selected for further study as a prototype.

An analysis of the archived SDSS spectrum (Dawson et al., 2016a) revealed a complex, slightly asymmetrical broad MgII emission line profile. A spectroscopic follow-up was conducted to capture the MgII emission line at its peak brightness, aiming to detect a potential peculiar or, in the best-case scenario, double-peaked profile. Due to the faintness of the source, 8-meter class telescopes were required to obtain high-quality spectra for a detailed analysis of the MgII line profile.

Spectroscopy was chosen as the next step in this research due to its potential to yield significant insights in a shorter timeframe. However, targeted photometric monitoring is also planned to complement the spectroscopic data and provide a comprehensive understanding of the quasar's behavior.

It is also necessary to mention that this source does not have a corresponding radio frequency signal, as it was not detected in various radio surveys, including the Very Large Array (VLA) FIRST Survey at 1.4 GHz (Becker et al., 1995), the AT20G Survey at 20 GHz (Massardi et al., 2011), and the early phases of the VLA Sky Survey. It was also undetected in the 1.4 GHz catalog by Hodge et al. (2011), which had slightly higher sensitivity (0.09 mJy compared to 0.13 mJy).

In this chapter, new observations of the MgII spectral line from the Gemini and Magellan

telescopes are presented and compared with the archived SDSS spectrum. These new observations were specifically proposed, obtained, and reduced for this study, forming an essential part of the research conducted. The physical implications of the significant changes in the double-peaked line profile are discussed, with observational times incorporated into the light curve folded with the previously calculated period. The comprehensive analysis combines both spectroscopic and planned photometric observations to provide a more complete understanding of the quasar's periodic variability and underlying physical processes.

## 5.1 Data and Analysis

The newly obtained Gemini and Magellan spectra are in more detail described in Section 2.2.2. Using the reduced and calibrated data, the underlying continuum and satellite Fe II emission lines were subtracted from the reduced and calibrated spectra as in Popović et al. (2019), using Fully Automated python tool for AGN Spectra analysis (Fantasy, Ilić et al., 2023). The spectrum was shifted to the rest frame and analyzed in terms of velocity space, calculated as described in Sections 3.3.2, 3.3.3.

The MgII line profile was analyzed using a set of easily measurable quantities to describe its complex changes, as outlined in Lewis et al. (2010): the velocity shifts of the two peaks, the flux ratio of the red and blue peaks, the full width at half-maximum (FWHM) and the full width at quarter-maximum (FWQM) of the entire profile, the peak separation, and profile asymmetry/skewness, measured as the shift between the center at half- and quarter-maximum of the MgII line profile and the  $0 \text{ km s}^{-1}$  (Popović et al., 2019).

A first estimate of the total mass of the system is calculated from the width of the broad MgII line and continuum flux at  $3000\text{\AA}$ , using the procedure described in Section 3.3.4. The separation  $a$  of the black holes in a possible SMBBH system is calculated as in Liu et al. (2019), using Kepler's law and assuming the variation occurs precisely on the rest-frame orbital period timescale. The relation is given by:  $\frac{a^3}{t_{\text{orb}}^2} = \frac{GM}{4\pi^2}$ , where  $t_{\text{orb}} = \frac{P_{\text{obs}}}{1+z}$  represents the rest-frame orbital period. These separations are expressed in units of parsecs (pc). The formal errors are obtained through independent measurements of the underlying continuum and are propagated accordingly.

The `rubin_sim` package (Yoachim et al., 2023) was used to calculate synthetic SDSS  $r$ -band magnitudes derived from Gemini, Magellan, and SDSS spectra at the phased points corresponding to the 278-day period. These were then compared to the model (phased) light curve. The spectral coverage was not sufficiently broad to obtain synthetic magnitudes in other bands.

Finally, given the dramatic variability in the emission line that could indicate complex dynamics within the system, an attempt was made to model the MgII broad line in the context of a binary SMBH system using the Popović, Simić, Kovačević, Ilić model (PoSKI, Popović et al., 2021) described in Section 3.3.5.

## 5.2 Results and Discussion

Dramatic evolution of MgII broad emission line profile displayed in velocity scale and shifted according to the observed phase based on photometric light curve in Fatović et al. (2023), is shown in Figure 5.1. The peak separation changed from  $1661 \text{ km s}^{-1}$  to  $1328 \text{ km s}^{-1}$ , and the peak flux ratio changed from 0.893 to 0.973 within the month that had passed between Gemini and Magellan observations. SDSS profile displays a single peak corresponding to the position of the red peak in the other two profiles. Also, there is an approximate  $1000 \text{ km s}^{-1}$  difference in Full Width at Half Maximum (FWHM), Full Width at Quarter Maximum (FWQM), and the skewness/asymmetry in the SDSS profile and the profiles of the new spectra. An intriguing observation is that the skewness of the line profile changed markedly in the time between Magellan and Gemini by around  $500 \text{ km s}^{-1}$  within a month. The red peak remains steady while the blue peak shifts, changing the overall shape of the MgII line profile. This observation inspired our efforts to model and explain these variations using the SMBBH system.

The results of the peak measurements are given in the Table 5.1. The system's mass estimation for all three spectra is  $M_{\bullet\bullet} \sim 10^9 M_{\odot}$ . This would make SDSS J2320+0024 one of the most massive sub-annual binary quasar candidates known.

Figure 5.2 shows a light curve, which combines observed and synthetic photometry from SDSS, ZTF, PS1, Gemini, and Magellan, overlaid on the sinusoidal model of periodic variations for SDSS J2320+0024. The parameters for this model were obtained by Fatović et al. (2023). The observations fall within the 95% confidence interval of the sinusoidal light curve, indicating periodic variability of the quasar. The inset displays a phase-folded view of the SDSS, Magellan, and Gemini observations, making the periodic nature of the variability more apparent and providing a compact representation of the quasar's optical variability over a single period. It is important to note that the SDSS synthetic magnitude shows greater deviation compared to the Gemini and Magellan synthetic magnitudes. This discrepancy is due to the entire observed SDSS spectrum being shifted upward by approximately  $2 \times 10^{-17} \text{ ergs s}^{-1} \text{ cm}^{-2} \text{ \AA}^{-1}$  before continuum subtraction. This shift is assumed to be caused either by a calibration error in the spectrum or by a flare of the AGN at the time of observation.

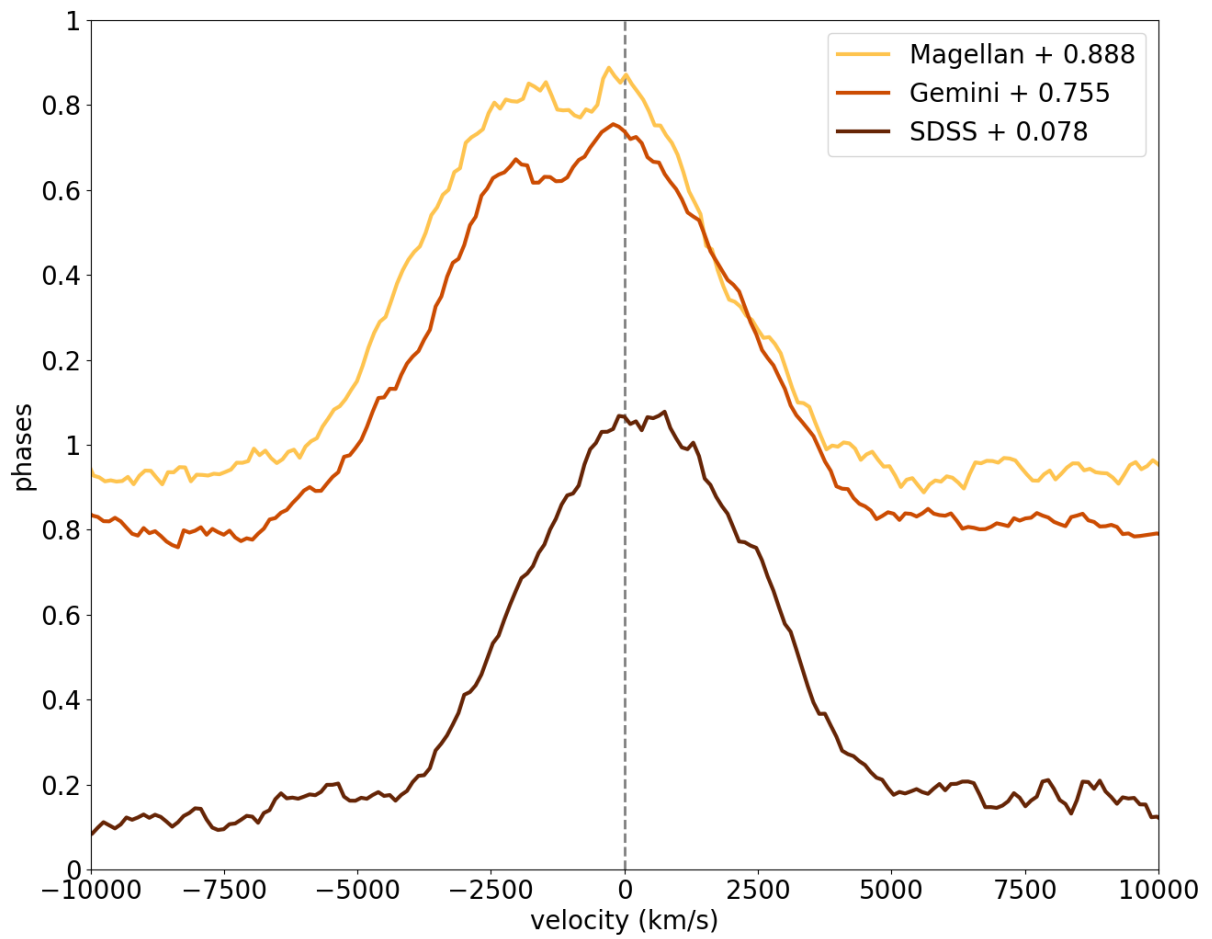


Figure 5.1: The normalized line profiles of the extracted MgII line, as observed with SDSS, Gemini, and Magellan telescopes, shifted by the observed phase, obtained from the photometric light curve. The vertical dashed line indicates a velocity of  $0 \text{ km s}^{-1}$ .

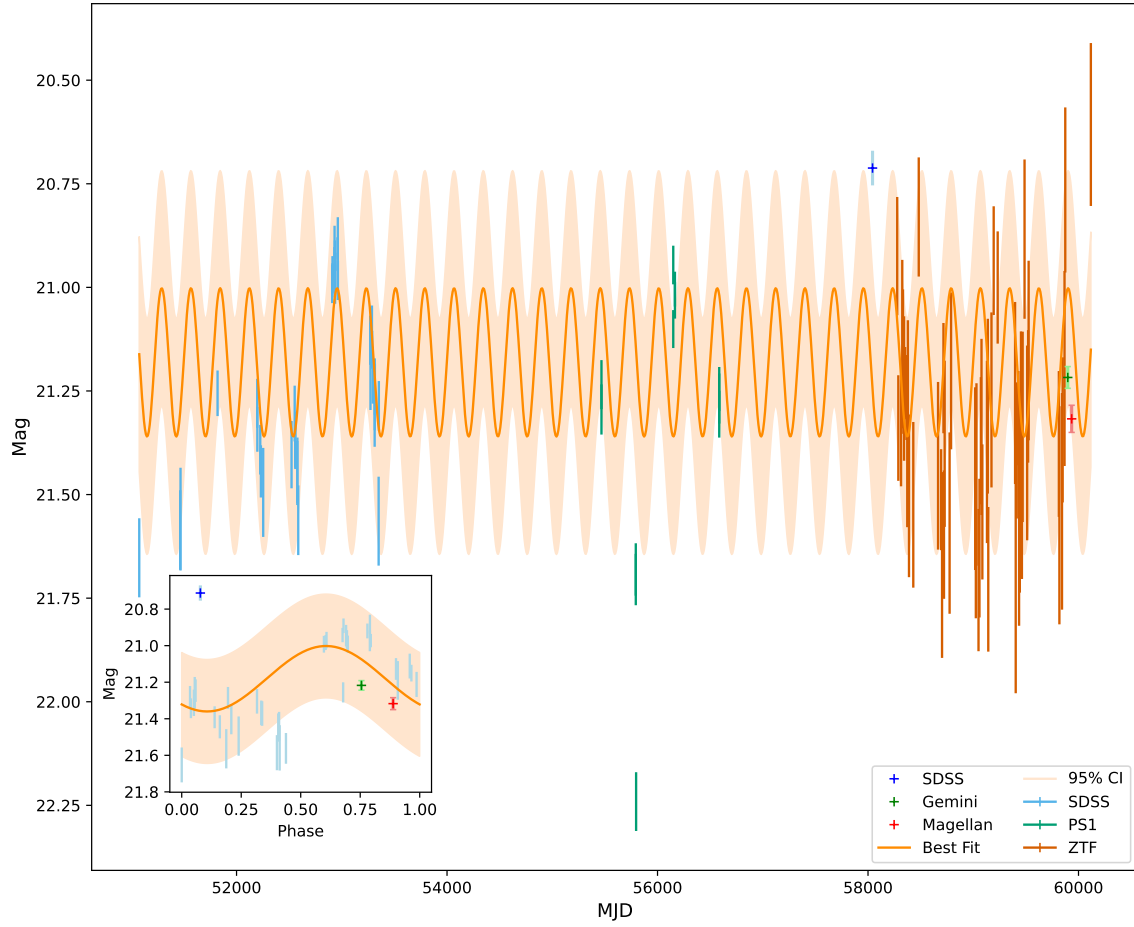


Figure 5.2: Overlay the SDSS, ZTF, PS1, Gemini, and Magellan observations, and the sinusoidal fit derived by (Fatović et al., 2023). The shaded area represents the 95% confidence interval (CI) of the sinusoidal fit. The inset showcases a phase-folded view of the SDSS, Magellan, and Gemini observations.

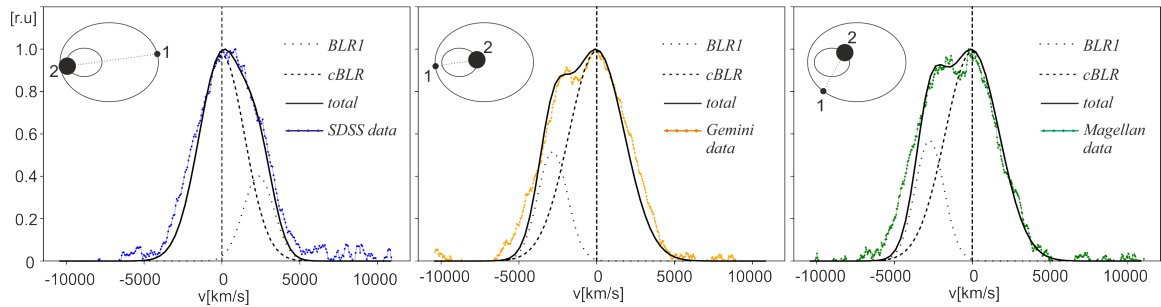


Figure 5.3: The PoSKI model of MgII broad line (black solid line) for all three epochs (left: SDSS, middle: Gemini, right: Magellan data). The components are coming from the smaller BLR (BLR1, dotted line) and cBLR (dashed line). Upper insets in each panel shows the binary configuration for the corresponding epoch. The wavelength is converted to the velocity scale given on the x-axis, whereas the y-axis shows the normalized intensity.

### 5.2.1 PoSKI model results

The PoSKI model was applied to interpret the observed behavior due to the dramatic changes in the position of the blue peak in the MgII line profile (see Figure 5.1), which correspond to expected phases (see Figure 5.2) and suggest the possibility of a binary system.

Figure 5.3 presents the MgII broad line profile described by the model (solid line) for all three epochs: SDSS, Gemini, and Magellan. The full parameter space constrained by our observations was explored, revealing the best-fitting parameters as follows: the total mass of the system is approximately  $\log(M) \sim 8.3 M_{\odot}$ , with a very low mass ratio ( $q = 0.1$ ) and a separation of 0.0025 pc. Each component has an accretion disk, while only the less massive component possesses a BLR. Both accretion disks illuminate a cBLR, resulting in a steady red peak from the cBLR and a shifting blue peak from the BLR of the smaller black hole. More sophisticated modeling will be possible with high-resolution and high signal-to-noise spectra.

The choice of a binary model is based on three factors. First, the binary model must correctly predict observable features, such as orbital characteristics and total mass, which it does in this study. Additionally, it should align with various data types, including light curves and spectral lines, both confirmed in our case, though radio emissions lack significant evidence. Finally, statistical significance may favor the binary model; however, to assess the single black hole alternative, other emission lines should be included in the analysis and their behavior investigated.

### 5.3 Chapter summary and conclusions

The detected dramatic variability in the broad MgII emission line is presented, observed during the initial spectroscopic follow-up of a potential CB-SMBBH candidate, selected through the detected periodicity ( $P=278$  days) in photometric light curves. This analysis yielded estimates of the total mass of the system to be approximately  $10^9 M_{\odot}$ , with significant velocity shifts between the two peaks of several hundred  $\text{km s}^{-1}$ . This substantial mass places the object among the most massive subannual binary quasar candidates known, suggesting a history marked by extensive galaxy mergers.

The results from the modeling and observations yielded consistent values for the masses and separations of the two components. Since these quantities were calculated and modeled independently, the obtained results are more convincing as accurate.

The case presented here stands out due to the pronounced changes in the MgII line shape that also appear correlated with variations in the light curve. If confirmed by spectroscopy of other emission lines, these results would indicate the potential yields of upcoming large time-domain optical surveys, such as the Vera Rubin Observatory Legacy Survey in Space and Time (LSST). The associated spectroscopy surveys are expected to detect and analyze such massive binary quasars, which will be instrumental in constraining the frequency of galaxy mergers. Further follow-up with large telescopes and high-precision instruments is necessary to confirm the true nature of this quasar.



Table 5.1: Measured quantities from the broad MgII emission line. Columns:  $\log(M_{\bullet\bullet}/M_{\odot})$ : logarithm of the estimated system's mass given in solar masses;  $\text{Shift}_B$  and  $\text{Shift}_R$ : peak shift of the blue and red peak in relation to the 0 km/s;  $F_R/F_B$ : ratio of the maximum fluxes of red and blue peaks; FWHM and FWQM: width of the whole profile at 50% and 25%; Separation: velocity separation of the blue and red peaks;  $\text{Shift}_{HM}$  and  $\text{Shift}_{QM}$ : velocity shift of the profile centroid at 50% and 25%, a: the separation.

	$\log(M_{\bullet\bullet}/M_{\odot})$	$\text{Shift}_B$ km s <sup>-1</sup>	$\text{Shift}_R$ km s <sup>-1</sup>	$F_B/F_R$	FWHM km s <sup>-1</sup>	FWQM km s <sup>-1</sup>	Separation km s <sup>-1</sup>	$\text{Shift}_{HM}$ km s <sup>-1</sup>	$\text{Shift}_{QM}$ km s <sup>-1</sup>	a pc
SDSS	9.0 ± 0.5	NA	356 ± 71	NA	5254 ± 71	7291 ± 179	NA	377 ± 36	324 ± 89	0.004 ± 0.001
Gemini	8.9 ± 0.5	-1801 ± 107	-140 ± 107	0.893 ± 0.004	6219 ± 107	8470 ± 250	1661 ± 107	-640 ± 36	-694 ± 36	0.003 ± 0.001
Magellan	8.8 ± 0.5	-1453 ± 71	-125 ± 71	0.973 ± 0.004	6112 ± 71	8256 ± 500	1328 ± 71	-1203 ± 38	-988 ± 250	0.003 ± 0.001

# Chapter 6

## Period analysis of Red Giant stars in Andromeda

Mira stars, a subtype of long-period variables (LPVs), form during the evolution of low- and intermediate-mass stars, particularly in the asymptotic giant branch (AGB) phase. Their distinct characteristics, including brightness, large amplitudes, and periods ranging from 10 to 1000 days, make them easily detectable. Consequently, their PL relation has emerged as a key tool for investigating LPVs and their evolution during the AGB phase.

Additional PL relations in semi-regular variables (SRVs) were initially identified by Wood & Sebo (1996b). Through research on the Magellanic Clouds, further distinct parallel PL relations or sequences were revealed (Wood et al., 1999; Ita et al., 2004), each associated with specific pulsation modes or star types. Notably, sequences B and C' are linked to the first overtone (1O) mode, while sequence D encompasses long secondary periods (LSPs) of uncertain origin (Hinkle et al., 2002; Wood & Nicholls, 2009; Saio et al., 2015).

Over the past two decades, large-scale surveys like the OGLE project have been instrumental in detecting and studying PL relations of LPVs (Soszyński et al., 2009a; Soszyński et al., 2011, 2013). With the release of Gaia DR3, a comprehensive database now facilitates all-sky monitoring of LPVs across multiple optical bands. Specifically, the GAPS field offers light curves for all sources, presenting a unique opportunity to explore the periodicity of Mira stars in the M31 galaxy.

Despite advancements, studies of Mira stars in the M31 galaxy using Gaia filters and calibration of their PL relations remain unexplored. Research on Mira stars in the Magellanic Clouds, utilizing data from the Optical Gravitational Lensing Experiment (OGLE), has provided significant insights into their properties and behaviors (e.g., Soszyński et al., 2009b; Groenewegen, M. A. T. & Blommaert, J. A. D. L., 2005; Bhardwaj et al., 2019). These studies have estab-

lished robust PL relations, which are crucial for understanding stellar evolution and distance measurements.

This chapter focuses on studying the long-period behavior of Mira stars observed in the GAPS field. Primary objectives include isolating Mira variable stars, determining their periods, and evaluating their fit to the PL relation using 2MASS data and Gaia photometric data for the first time, alongside comparisons with previous studies.

## 6.1 Data and Methods

The data used in this research are described in Sections 2.1.4 and 2.1.5. Starting with the Gaia GAPS data, the first step was to identify the Andromeda galaxy. Since Milky Way sources have well-determined parallaxes, they were filtered out using a criterion of large parallax angles. This approach ensures that only M31 sources remain in the sample, as large distances cause parallaxes to tend towards zero, and negative parallaxes and measurement errors were accounted for in the process. It is important to note that inverting parallaxes to determine distances can be inaccurate due to measurement uncertainties, non-linearity, and negative parallax values, leading to unreliable estimates. The Bailer-Jones catalog (Bailer-Jones et al., 2021) uses a Bayesian approach, incorporating parallax uncertainties and prior knowledge about stellar distributions, resulting in more accurate and reliable distance measurements. All sources with a parallax less than 0.5 mas were discarded as belonging to the Milky Way. For the remaining sources, it was required that their variability amplitude, measured from the 95th to the 5th percentile, be greater than 0.8 mag in G filter. This criterion excluded most of non-Mira stars, as Miras are known for their significant brightness variations. Although this sample might have included some Cepheids, they were later filtered out based on their distinctive light curve shapes. Using this straightforward filtering method, the sample likely remained contaminated with sources from the Milky Way that are in the line of sight toward M31. It is expected that these sources, if present in the sample, would later be filtered out due to their significantly higher brightness compared to the others.

At this point, the sample contained sources that a) were unlikely to be in the Milky Way and b) exhibited an amplitude of at least 0.8 magnitudes in the G filter. The next logical step was to determine the locations of these sources within the GAPS field, as shown in Figure 6.1. In Figure 6.1, red dots represent the sources extracted so far. The grey dot marks the center of the M31 galaxy, while the orange dots indicate the 400 sources closest to the center of M31 from the filtered sample. This final sample was used for period calculations and considered as potential Mira stars in the M31 galaxy, which were the targeted sources.

To reduce the impact of dust extinction, this sample was also cross-referenced with the 2MASS catalog as mentioned in the Section 2.1.5.

The Wesenheit magnitudes for 2MASS and Gaia data were calculated using following formulas (Soszyński et al., 2005; Lebzelter et al., 2018; Ripepi et al., 2019):

$$W_{J,K} = K - 0.686(J - K), \quad (6.1)$$

$$W_G = G - 1.9(BP - RP), \quad (6.2)$$

$$W_{BP,RP} = RP - 1.3(BP - RP), \quad (6.3)$$

where the maxima of the models were utilized instead of mean magnitudes, as recommended in Bhardwaj et al. (2019). However, due to the absence of light curve data in the 2MASS dataset, only mean magnitudes were employed. Because of the small number of observations, it is likely that these medians deviate from the true medians. Additionally, due to the large amplitudes of Mira, significant deviations are possible.

### Period analysis

For the period calculation, *astropy's* implementation of Lomb-Scargle periodogram described in Section 3.1.1 was used. Although Gaia provides light curves in all three bands (G, BP, RP), only the G band was used for period calculation. This is because the G band typically has a larger number of data points and a higher signal-to-noise ratio. Also, crowding in the BP and RP Gaia filters occurs due to the presence of multiple sources in close proximity causing the overlapping of multiple stellar spectra, making it difficult to distinguish individual stars. The BP and RP filters were later used for confirmation. As suggested in Evans et al. (2023), the flags `rejected_by_photometry` and `rejected_by_variability` were set to `False`. Additionally, each lightcurve was required to have at least 25 data points. The period grid was defined from 100 days to the observed time span, calculated as  $t_{\max} - t_{\min}$ , with a grid spacing of 10 minutes. A 5-minute grid was tested, but it resulted in only a 0.0001% difference in the calculated periods, so the 10-minute spacing was used. This process narrowed down the initial 400 candidates to 209 candidates for Mira stars.

To eliminate aliases, sources with similar periods (within 0.5 days) were discarded, as it is statistically unlikely for multiple sources to have identical periods. This refinement left a sample of 101 sources.

To verify their that the correct periods were derived, the contamination of the sample and the variability type, the light curves (LCs) and phased light curves (PLCs) were visually assessed. This step was crucial to confirm whether a source is truly a variable Mira star. While visual

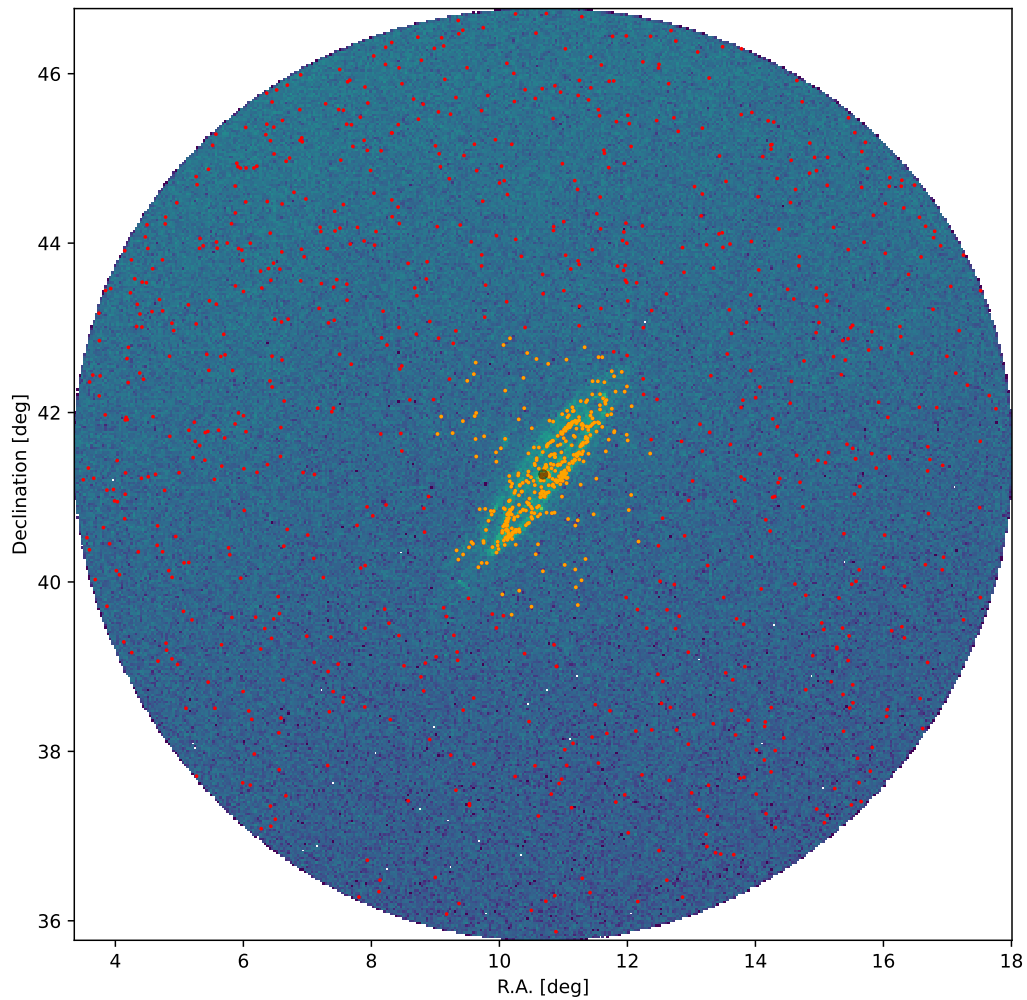


Figure 6.1: Sample selected from the GAPS field.

assessment of LCs is a standard technique, more rigorous statistical analyses could be employed in future work to achieve greater precision and minimize human subjective bias. After this criterion, the sample was left with 25 sources.

## 6.2 Results and discussion

An example of a good Mira candidate using Gaia G band data is shown in Figure 6.2.

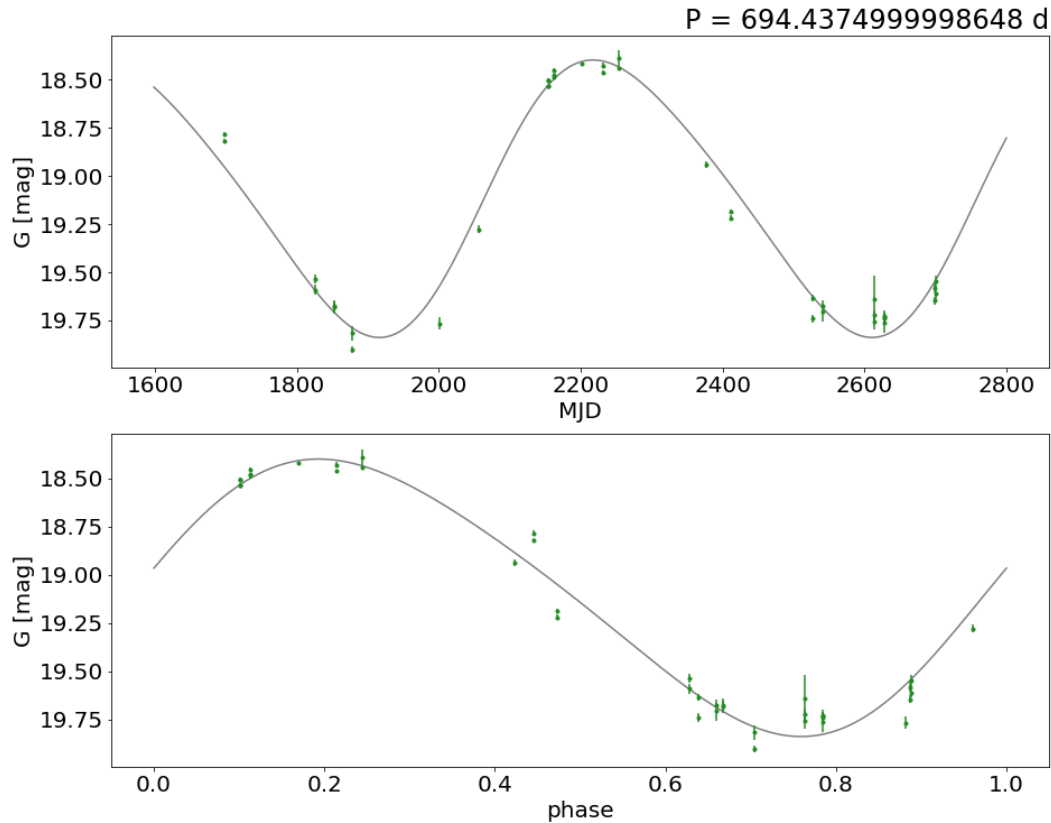


Figure 6.2: An example of a good Mira candidate. Upper panel is showing a light curve, and the bottom one shows a phased light curve folded with the period noted in the upper right corner of the figure. The green error bars show the data in Gaia G band, and the grey line shows the predicted model.

The model light curve, plotted as a grey line, was calculated using  $N=2$  terms in the Fourier series described in Section 3.1.1. The upper panel displays the light curve, while the lower panel shows the phased light curve, folded with the period indicated in the upper right corner of the figure.

For comparison, these 25 candidates were cross-matched with the Gaia archive, specifically in the `gaiadr3.vari_long_period_variable` table, with the condition that they have a value in "frequency" column. This search resulted in 8 matches. The purpose of this comparison was to determine how many of the 25 candidates were already identified in the Gaia archive as long-

period variables and to compare the periods from this study with the Gaia-calculated periods. The results showed that this study identified 17 new sources as long-period variables, likely Mira-type stars. The period comparison is illustrated in Figure 6.3. A notable discrepancy of 119 days was found for one source. By comparing phased light curves folded with both the period from this study and the Gaia period, it was concluded that the period from this study provided a better fit. The good agreement between the Gaia periods and those calculated in this study provides confidence in the accuracy of the periods for the 17 new candidates.

### 6.2.1 PL relation

The next objective was to determine the placement of these sources on the Period-Luminosity (PL) relation. The Wesenheit magnitude was calculated using equation 6.2. All sources were compared to the OGLE III Miras dataset (Soszyński et al., 2009b), as illustrated in Figure 6.4. This comparison indicated that 23 out of 25 sources in this study were likely classified as O-rich Miras, while the remaining 2 (fainter than 13 mag) were identified as C-rich Miras. Due to their low number, these C-rich Miras will be excluded from further analysis. The classification of some longer-period Miras is not definitive as they could be either O-rich or C-rich. However, since they generally follow the same ridge as the OGLE II O-rich Miras, these sources were retained, considering the already small sample size. Consequently, the final sample for this research consists of 23 O-rich Mira candidates.

Unlike the OGLE III study of the LMC, this work found only a few shorter-period Mira candidates. Most of the candidates are in the longer-period range, which is expected given the greater distance of M31 compared to the LMC and the fact that longer periods are associated with brighter stars.

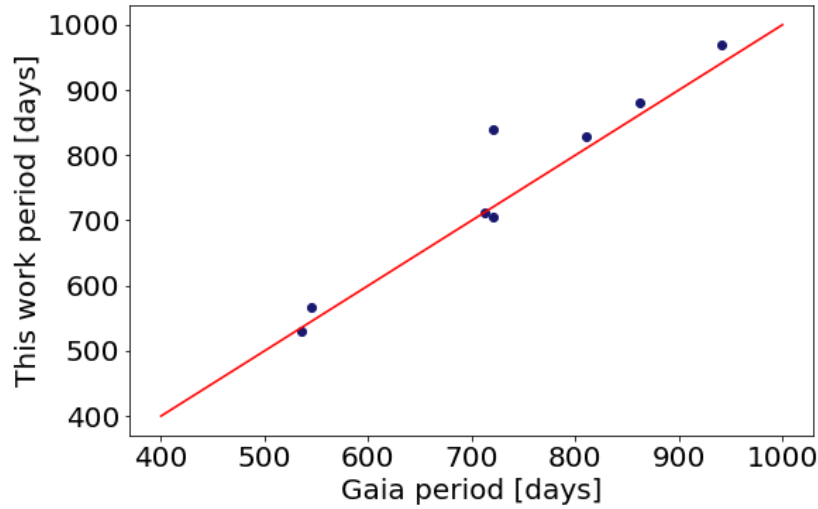


Figure 6.3: Comparison of the Gaia periods with those calculated in this study. The red line represents the  $x = y$  line, which serves as a visual aid to help compare the periods.

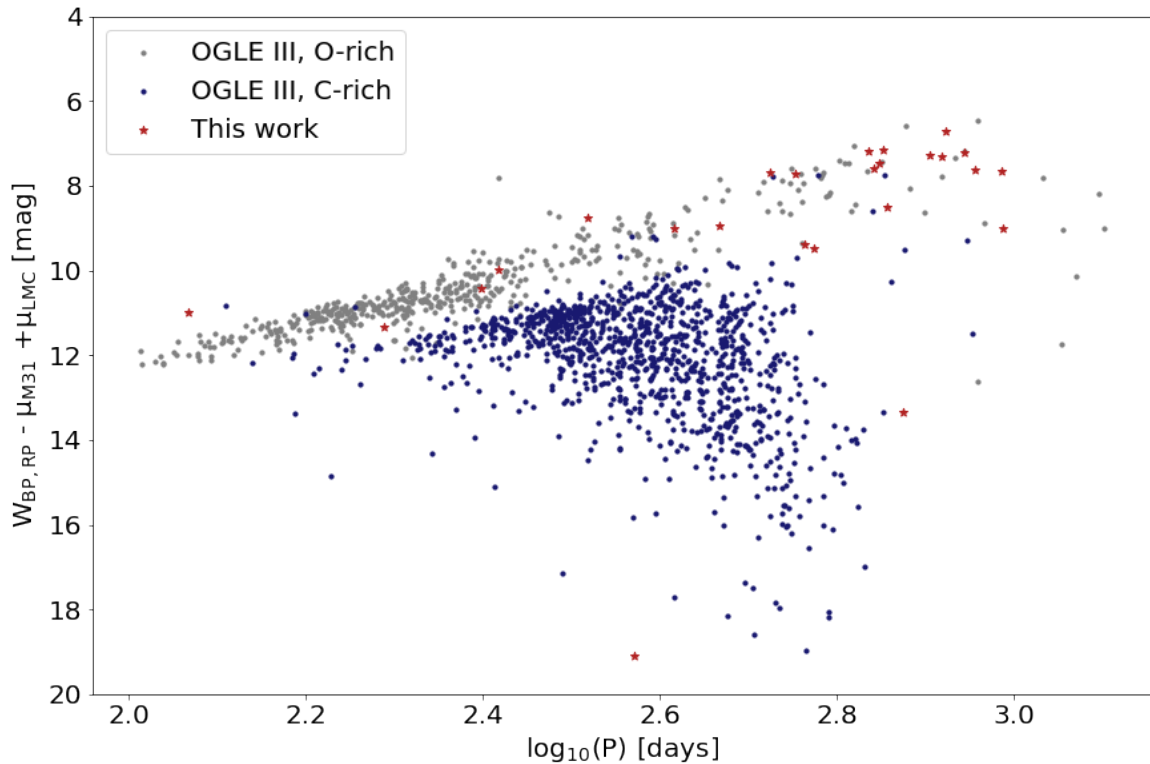


Figure 6.4: The comparison between the OGLE III Miras and those identified in this study. For consistency in the comparison, all data have been adjusted to the distance modulus of the Large Magellanic Cloud (LMC). The distance moduli applied were  $\mu_{LMC} = 18.49$  mag (de Grijs et al., 2017) for the LMC and  $\mu_{M31} = 24.41$  mag (Li et al., 2021) for M31. OGLE III Miras dataset is taken from Soszyński et al. (2009b) and cross-matched with Gaia DR3 sources.

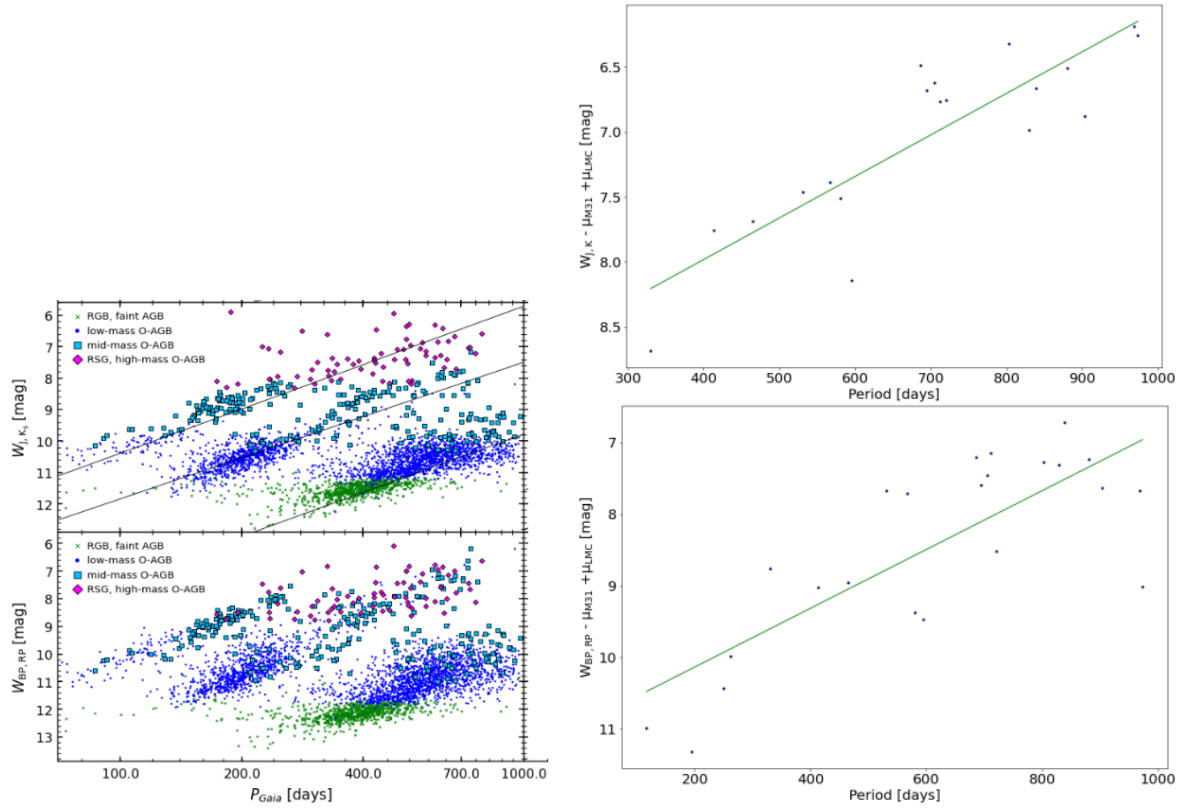


Out of the final 23, only 19 were detected in 2MASS 6X. Their PL relation is given in the Figure 6.5 and compared to results from Lebzelter, T. et al. (2019). When the comparison is made, it can be concluded that the sample from this work consist of high- and mid-mass O-AGB stars.

The final result is presented in the Table 6.1 together with the results from the previous works similary summarized in Sun et al. (2023). The PL relation for the comparison given in this table was modified so the comparison is possible:

$$M = a_0 + a_1(\log_{10}(P) - 2.3), \quad (6.4)$$

where  $M$  represents the absolute magnitude,  $P$  represents the period, and  $a_0$  and  $a_1$  represent the zero-point slope of the PL relation.



(a) PL relations for different variable sources in Gaia  $W_{BP,RP}$  (bottom panel) and 2MASS in  $W_{J,K}$  (upper panel). This figure was taken from Lebzelter, T. et al. (2019).

(b) PL relation for 23 final sources in Gaia  $W_{BP,RP}$  (bottom panel) and 19 final sources found in 2MASS in  $W_{J,K}$  (upper panel).

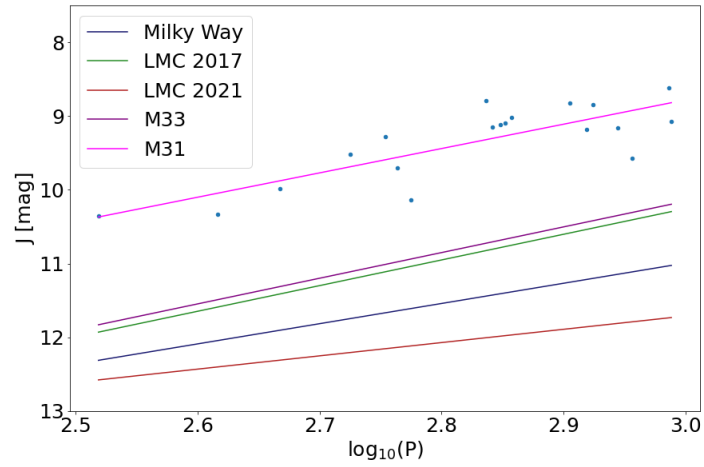
Figure 6.5: Comparison of the PL relations in Gaia and 2MASS from this work and Lebzelter, T. et al. (2019). For consistency in the comparison with two panels of the left column taken from Lebzelter, T. et al. (2019), all data have been adjusted to the distance modulus of the Large Magellanic Cloud (LMC). The distance moduli applied were  $\mu_{LMC} = 18.49$  mag (de Grijs et al., 2017) for the LMC and  $\mu_{M31} = 24.41$  mag (Li et al., 2021) for M31. The green line represents the linear fit.

All PL relations given in Table 6.1 are visualized in Figure 6.6. It can be observed that all PL relations are relatively consistent with each other. Additionally, it is evident that the data and PL relation from this study (M31 in the images) show a significantly larger intercept. Several potential explanations exist for this observation. Firstly, previous studies often used significantly more data for calibrating the PL relation. Furthermore, by using Gaia observations of Mira stars from M31, it was possible to reliably identify only the brighter Miras with longer periods due to a sufficient number of observations. This absence of sources in the lower left corner of the PL relation could have affected the results. Additionally, many studies of the PL

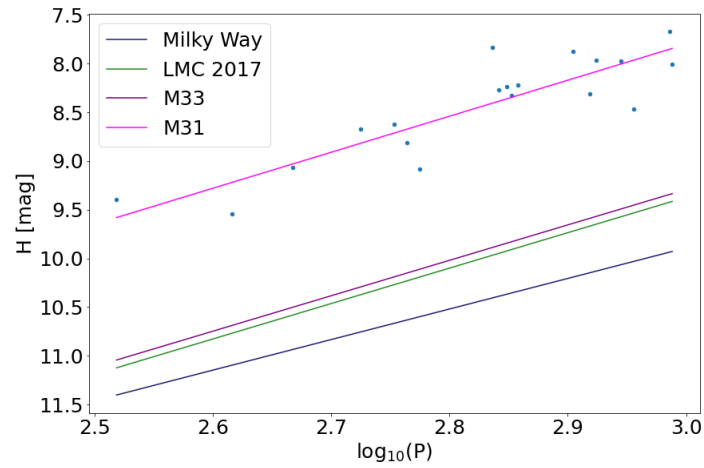
relation for Miras use higher-degree polynomials, as seen in Yuan et al. (2017a, 2018a). The nonlinear nature of the PL relation in Mira stars, combined with the fact that the data used in this study only cover the upper right part of the PL diagram, may contribute to the observed discrepancy.

Table 6.1: The results of this study were compared with those of previous research. By employing identical source types and fitting the period-luminosity relation, consistent outcomes were achieved across various galaxies. Additionally, the period-luminosity parameters for  $W_{BP,RP}$  and  $W_{J,K}$  were determined in this study.

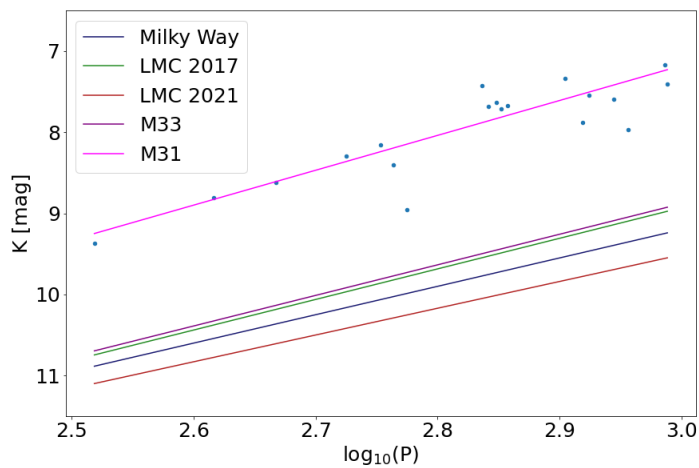
Galaxies	Band	$a_1$	$a_0$	Number	Reference
Milky Way	$J$	$-2.74 \pm 0.32$	$-5.58 \pm 0.06$	299	Sun et al. (2023)
Milky Way	$H$	$-3.14 \pm 0.30$	$-6.40 \pm 0.06$	299	Sun et al. (2023)
Milky Way	$K$	$-3.50 \pm 0.25$	$-6.84 \pm 0.05$	298	Sun et al. (2023)
LMC	$J$	$-3.48 \pm 0.09$	$-5.80 \pm 0.04$	158	Yuan et al. (2017b)
LMC	$H$	$-3.64 \pm 0.09$	$-6.57 \pm 0.04$	158	Yuan et al. (2017b)
LMC	$K$	$-3.77 \pm 0.07$	$-6.92 \pm 0.04$	158	Yuan et al. (2017b)
LMC	$J$	$-1.83 \pm 0.79$	$-5.52 \pm 0.09$	29	Iwanek et al. (2021)
LMC	$K$	$-3.30 \pm 0.46$	$-6.67 \pm 0.06$	29	Iwanek et al. (2021)
M33	$J$	$[-3.48]$	$-5.90 \pm 0.01$	1,169	Yuan et al. (2018b)
M33	$H$	$[-3.64]$	$-6.65 \pm 0.01$	1,169	Yuan et al. (2018b)
M33	$K$	$[-3.77]$	$-6.97 \pm 0.01$	1,169	Yuan et al. (2018b)
M31	$J$	$-3.3 \pm 0.6$	$-7.4 \pm 0.3$	19	This work
M31	$H$	$-3.7 \pm 0.5$	$-8.1 \pm 0.3$	19	This work
M31	$K$	$-4.2 \pm 0.3$	$-8.3 \pm 0.3$	19	This work
M31	$W_{BP,RP}$	$-4.5 \pm 0.6$	$-8.1 \pm 0.3$	23	This work
M31	$W_{J,K}$	$-4.7 \pm 0.6$	$-9.0 \pm 0.3$	19	This work



(a) PL relations for different galaxies in J filter.



(b) PL relations for different galaxies in H filter.



(c) PL relations for different galaxies in K filter.

Figure 6.6: Comparison of the PL relations for different galaxies in JHK filters. For consistency with the Table 6.1, M31 data have been adjusted to the distance modulus of the LMC. The distance moduli applied were  $\mu_{LMC} = 18.49$  mag (de Grijs et al., 2017) and  $\mu_{M31} = 24.41$  mag (Li et al., 2021).

### 6.3 Chapter summary and conclusions

This work studies the long-period behavior of Mira stars observed in the GAPS field. The primary objectives were to isolate Mira variable stars, determine their periods, and evaluate their fit to the PL relation using 2MASS and Gaia photometric data for the first time.

The obtained P-L relations are:

$$J = (-3.3 \pm 0.6) + (-7.4 \pm 0.3)(\log_{10}(P) - 2.3), \quad (6.5)$$

$$H = (-3.7 \pm 0.5) + (-8.1 \pm 0.3)(\log_{10}(P) - 2.3), \quad (6.6)$$

$$K = (-4.2 \pm 0.3) + (-8.3 \pm 0.3)(\log_{10}(P) - 2.3), \quad (6.7)$$

$$W_{BP,RP} = (-4.5 \pm 0.6) + (-8.1 \pm 0.3)(\log_{10}(P) - 2.3), \quad (6.8)$$

$$W_{J,K} = (-4.7 \pm 0.6) + (-9.0 \pm 0.3)(\log_{10}(P) - 2.3). \quad (6.9)$$

While there is room for improvement of this analysis which relies on the visual inspection of LCs and PLCs, the results are comparable to those from previous works given in Table 6.1. The main motivation for this research was to test the GAPS data, given that Gaia will soon release Data Release 4 (DR4), providing light curves for the entire sky. By publishing the light curves for the GAPS field, a glimpse of future capabilities with the upcoming Gaia data has been obtained.

# Chapter 7

## Thesis summary and outlook

### 7.1 Summary of this Thesis

This thesis investigates long-period variability in large optical sky surveys. Periodically variable sources are crucial for distance estimation in the universe. Additionally, observing periodic variability in AGNs can provide insights into the possibility of binary black hole systems, forming a foundation for the study of gravitational waves.

#### **Detecting long - period variability in the SDSS Stripe 82 standards catalog**

A key challenge in studying variable sources is accurately determining their periods. Ensuring the calculated period reflects true variability, rather than an alias or bias, requires careful application of various statistical filters. Chapter 4 tackles this issue by introducing a series of filters to reliably determine the periods of objects previously classified as non-variable. Consequently, five quasars with plausible periodic variability in the SDSS *ugriz* filters are identified, with the quasar exhibiting the shortest period selected for further investigation.

#### **Complex MgII Time Evolution in SDSS J2320+0024: Clues for a Subparsec Binary Supermassive Black Hole?**

Long-period variations are observed in both stars and AGNs. While stellar variations are well understood, periodic variability in AGNs can be explained by multiple phenomena. Chapter 4 identifies five quasars with significant periodic brightness changes. In Chapter 5, one of these quasars is analyzed using newly observed MgII lines and archived SDSS spectra, providing three epochs of MgII observations. By applying the PoSKI model and comparing synthetic magnitudes with photometric data, a correlation is established between the observed behavior

and the modeled system, suggesting the presence of a binary supermassive black hole in a close orbit.

### **Period analysis of Red Giant stars in Andromeda**

The Gaia satellite began its scientific observations in 2014. This is significant for the study of variability as Gaia maps the entire sky. So far, three Gaia data releases have been published, providing light curves for all classified variable objects. In the latest data release, DR3, Gaia included light curves for all objects within a field centered on the Andromeda Galaxy, covering 5.5 degrees around it. Using this data, in Chapter 6 Mira stars in the M31 galaxy were identified, and periods were determined for those with sufficient light curve data. For the first time, a period-luminosity (PL) relation for Mira variables in the M31 galaxy was established using Gaia filters. Although the method can be improved, the results obtained using simple cuts and analyses are promising and lay the foundation for future research using Gaia's light curves for the entire sky.

## 7.2 Future work

### Detecting long - period variability in the SDSS Stripe 82 standards catalog

Future research related to the work presented in Chapter 4 will benefit from upcoming sensitive large-area surveys, such as the Rubin Observatory Legacy Survey of Space and Time. With its significantly larger sky coverage (approximately 60 times greater than SDSS) and enhanced sensitivity ( $\sim 2$  magnitudes), this survey will be more effective in detecting periodic variability in sources previously characterized as non-variable due to their long periods (more than 100 days) and small amplitudes (less than 0.3 mag).

### Complex MgII Time Evolution in SDSS J2320+0024: Clues for a Subparsec Binary Supermassive Black Hole?

To characterize the source presented in Chapters 4 and 5 as a binary supermassive black hole system, extensive observations are required. These observations should include further spectroscopic monitoring, such as continued observation of the Mg II line, monitoring another line like  $H\beta$ , and comparing the changes in these lines to the previously calculated period. Photometric observations are also essential, as a large amount of data is needed to confirm periodicity in the light curve. Additionally, observations in other parts of the spectrum would be highly valuable.

Observations of the radio emission from this object may provide a unique diagnostic of the supermassive black hole binary (SMBBH) energetics and environment. For example, shocks generated during disc crossings can produce synchrotron radiation in the radio band. High-velocity outflows observed in the optical emission lines may also produce shocks on scales larger than the broad-line region. Furthermore, high-resolution Very Long Baseline Interferometry (VLBI) imaging, with milliarcsecond-scale resolution (corresponding to a physical size of about 8 parsecs at the redshift of SDSSJ2320+0024), is the only observational method that can indicate the presence of a compact radio core, using its compactness and high brightness temperature (e.g., An et al., 2022).

Detection of the jet would offer exciting follow-up possibilities, such as measuring changes in its position angle. Notably, the most promising other SMBBH candidate is the radio galaxy 0402+379, with two flat-spectrum radio cores detected using VLBA at a projected separation of about 7 parsecs (Maness et al., 2004).



**Period analysis of Red Giant stars in Andromeda**

The study presented in Chapter 6 offers a straightforward analysis of the periodicity of Mira variables in M31. This analysis can be enhanced by incorporating factors such as stellar motion in Andromeda, color, and all three Gaia filters when calculating periods, as well as using more objective methods to verify periodicity rather than relying on visual assessments. Methods used in Chapter 4, such as the Kuiper method and Monte Carlo simulations can also be applied in future work. Additionally, Gaia DR4 will provide light curve data for all observed objects, allowing this method to be used for other galaxies observed by Gaia, as well as for brighter AGNs.

# Appendix A

## Basic concepts

**The luminosity (brightness)** of a star  $L$ , is defined as the energy radiated by a star per unit of time. The luminosity of the Sun is  $L_{\odot} = 3.85 \cdot 10^{26}$  W.

**The flux of radiation**  $F$ , which represents the energy passing through a unit area perpendicular to the direction of radiation propagation at a distance  $r$  from a star with luminosity  $L$ , is calculated using the formula  $F = L/(4\pi r^2)$ .

**Apparent brightness or apparent magnitude**  $m$  of a star is a logarithmic scale for brightness. Expressed in terms of  $L$ :

$$m = -2.5 \cdot \log_{10} \left( \frac{L}{d^2} \right) - 2.72, \quad (\text{A.1})$$

where  $d$  is the distance to the star in parsecs (1 parsec = 3.26 ly =  $3.086 \cdot 10^{16}$  m). Therefore, a star appears brighter in the sky when  $m$  is smaller. The brightest stars even have negative brightness values. Due to its proximity, the Sun is the brightest object in the sky with  $m = -26.7$ , Sirius (the brightest star after the Sun) has  $m = -1.5$ , Vega has  $m = 0$ , etc.

**Absolute brightness or absolute magnitude**  $M$  is defined as the apparent magnitude a celestial object would have at a distance of 10 parsecs. The relationship between apparent and absolute magnitude is given by:

$$m - M = 5 \cdot \log_{10} d - 5. \quad (\text{A.2})$$

From the above equation is clear that in order to determine a source's absolute magnitude, it is important to measure its apparent magnitude and know the distance to that specific source.

This relationship shown in Equation A.2 is also called the **distance modulus** and is defined as  $\mu = m - M$ . In other words, knowing a source's apparent and absolute magnitude, it is possible to determine its distance:

$$d = 10^{\frac{\mu}{5} + 1}. \quad (\text{A.3})$$

**Opacity** ( $\kappa$ ) is a property of stellar layers that determines their ability to transmit photons. Assuming  $I_0$  as the initial intensity of light, after a distance  $x$ , the intensity becomes:

$$I(x) = I_0 e^{-\kappa \rho x}, \quad (\text{A.4})$$

where  $\rho$  is the density of matter.

# References

- Afanasiev V. L., Popović L. Č., Shapovalova A. I., 2019, MNRAS, 482, 4985, *Spectropolarimetry of Seyfert 1 galaxies with equatorial scattering: black hole masses and broad-line region characteristics*
- An T., et al., 2022, A&A, 663, A139, *VLBI imaging of the pre-coalescence SMBHB candidate SDSS J143016.05+230344.4*
- Antonucci R., 1993a, ARA&A, 31, 473, *Unified models for active galactic nuclei and quasars.*
- Antonucci R., 1993b, Annual Review of Astronomy and Astrophysics, 31, 473, *Unified models for active galactic nuclei and quasars*
- Antonucci R., 2022, Nature, 602, 390, *The glowing dusty heart of a hidden quasar*
- Antonucci R. R. J., Miller J. S., 1985, ApJ, 297, 621, *Spectropolarimetry and the nature of NGC 1068.*
- Astropy Collaboration et al., 2013, A&A, 558, A33, *Astropy: A community Python package for astronomy*
- Astropy Collaboration et al., 2018, AJ, 156, 123, *The Astropy Project: Building an Open-science Project and Status of the v2.0 Core Package*
- Bailer-Jones C. A. L., Rybizki J., Fouesneau M., Demleitner M., Andrae R., 2021, *VizieR Online Data Catalog: Distances to 1.47 billion stars in Gaia EDR3 (Bailer-Jones+, 2021)*, VizieR On-line Data Catalog: I/352. Originally published in: 2021AJ....161..147B
- Barth A. J., et al., 2015, The Astrophysical Journal Supplement Series, 217, 26, *The lick agn monitoring project 2011: Spectroscopic campaign and emission-line light curves*
- Barthes D., 2006, jaavso, 35, 81, *Pulsation Modes and Fundamental Parameters of Mira Stars*
- Becker R. H., White R. L., Helfand D. J., 1995, ApJ, 450, 559, *The FIRST Survey: Faint Images of the Radio Sky at Twenty Centimeters*
- Begelman M. C., Blandford R. D., Rees M. J., 1980, Nature, 287, 307, *Massive black hole binaries in active galactic nuclei*
- Bellm E. C., et al., 2019, PASP, 131, 018002, *The Zwicky Transient Facility: System Overview, Performance, and First Results*
- Bhardwaj A., et al., 2019, ApJ, 884, 20, *Multiwavelength Period-Luminosity and Period-Luminosity-Color Relations at Maximum Light for Mira Variables in the Magellanic Clouds*
- Blanton M. R., et al., 2017, AJ, 154, 28, *Sloan Digital Sky Survey IV: Mapping the Milky Way, Nearby Galaxies, and the Distant Universe*
- Bochkarev N. G., Gaskell C. M., 2009, Astronomy Letters, 35, 287, *The accuracy of supermassive black hole masses determined by the single-epoch spectrum (Dibai) method*
- Bogdanović T., Miller M. C., Blecha L., 2022, Living Reviews in Relativity, 25, 3, *Electromagnetic counterparts to massive black-hole mergers*
- Caputo F., Marconi M., Musella I., 2000, A&A, 354, 610, *Theoretical models for classical Cepheids. V. Multi-wavelength relations*
- Carroll B. W., Ostlie D. A., 2017, *An introduction to modern astrophysics, Second Edition*
- Catelan M., Pritzl B. J., Smith H. A., 2004, ApJS, 154, 633, *The RR Lyrae Period-Luminosity Relation. I. Theoretical Calibration*
- Chambers K. C., et al., 2016, arXiv e-prints, p. arXiv:1612.05560, *The Pan-STARRS1 Surveys*

- Chiosi C., 1990, in Cacciari C., Clementini G., eds, *Astronomical Society of the Pacific Conference Series Vol. 11, Confrontation Between Stellar Pulsation and Evolution*. pp 158–192
- Ciardi D. R., et al., 2011, *AJ*, 141, 108, *Characterizing the Variability of Stars with Early-release Kepler Data*
- Clementini G., et al., 2019, *A&A*, 622, A60, *Gaia Data Release 2. Specific characterisation and validation of all-sky Cepheids and RR Lyrae stars*
- Cutri R. M., et al., 2012, *VizieR Online Data Catalog: 2MASS 6X Point Source Working Database / Catalog (Cutri+ 2006)*, VizieR On-line Data Catalog: II/281. Originally published in: 2012yCat.2281....0C
- Damianou A., Lawrence N. D., 2013, in Carvalho C. M., Ravikumar P., eds, *Proceedings of Machine Learning Research Vol. 31, Proceedings of the Sixteenth International Conference on Artificial Intelligence and Statistics*. PMLR, Scottsdale, Arizona, USA, pp 207–215, <https://proceedings.mlr.press/v31/damianou13a.html>
- Dark Energy Survey Collaboration et al., 2016, *MNRAS*, 460, 1270, *The Dark Energy Survey: more than dark energy - an overview*
- Dawson K. S., et al., 2012, *The Astronomical Journal*, 145, 10, *The baryon oscillation spectroscopic survey of sdss-iii*
- Dawson K. S., et al., 2013, *AJ*, 145, 10, *The Baryon Oscillation Spectroscopic Survey of SDSS-III*
- Dawson K. S., et al., 2016a, *The Astronomical Journal*, 151, 44, *The sdss-iv extended baryon oscillation spectroscopic survey: Overview and early data*
- Dawson K. S., et al., 2016b, *AJ*, 151, 44, *The SDSS-IV Extended Baryon Oscillation Spectroscopic Survey: Overview and Early Data*
- Dias dos Santos D., Rodríguez-Ardila A., Panda S., Marinello M., 2023, *ApJ*, 953, L3, *First Observation of a Double-peaked O I Emission in the Near-infrared Spectrum of an Active Galaxy*
- Dibai E. A., 1977, *Soviet Astronomy Letters*, 3, 1, *Mass of the central bodies of active galaxy nuclei*
- Dibai E. A., 1978, *Soviet Ast.*, 22, 261, *The envelope parameters and mass of active nuclei of galaxies*
- Du P., et al., 2016, *ApJ*, 825, 126, *Supermassive Black Holes with High Accretion Rates in Active Galactic Nuclei. V. A New Size-Luminosity Scaling Relation for the Broad-line Region*
- Eracleous M., Halpern J. P., 1994, *ApJS*, 90, 1, *Double-peaked Emission Lines in Active Galactic Nuclei*
- Eracleous M., Boroson T. A., Halpern J. P., Liu J., 2012, *The Astrophysical Journal Supplement Series*, 201, 23, *A large systematic search for close supermassive binary and rapidly recoiling black holes*
- Evans I. N., et al., 2010, *ApJS*, 189, 37, *The Chandra Source Catalog*
- Evans D. W., et al., 2023, *A&A*, 674, A4, *Gaia Data Release 3. The Gaia Andromeda Photometric Survey*
- Eyer L., Mowlavi N., 2008, in *Journal of Physics Conference Series*. p. 012010 (arXiv:0712.3797), doi:10.1088/1742-6596/118/1/012010
- Fanaroff B., Riley J., 1974, *Monthly Notices of the Royal Astronomical Society*, 167, 31P, *The morphology of extragalactic radio sources of high and low luminosity*
- Fatović M., Palaversa L., Tisanić K., Thanjavur K., Željko Ivezić Kovačević A. B., Ilić D., Č. Popović L., 2023, *The Astronomical Journal*, 165, 138, *Detecting long-period variability in the sdss stripe 82 standards catalog*
- Ferrarese L., Merritt D., 2000, *ApJ*, 539, L9, *A Fundamental Relation between Supermassive Black Holes and Their Host Galaxies*
- Flewelling H. A., et al., 2020, *The Astrophysical Journal Supplement Series*, 251, 7, *The pan-starrs1 database and data products*
- Foster G., 1996, *AJ*, 112, 1709, *Wavelets for period analysis of unevenly sampled time series*
- Gaia Collaboration et al., 2016, *A&A*, 595, A1, *The Gaia mission*
- Gaia Collaboration et al., 2018, *A&A*, 616, A1, *Gaia Data Release 2. Summary of the contents and survey properties*
- Gaia Collaboration et al., 2019, *A&A*, 623, A110, *Gaia data release 2 - variable stars in the colour-absolute magnitude diagram*

- Gaia Collaboration et al., 2023a, *A&A*, 674, A1, *Gaia Data Release 3. Summary of the content and survey properties*
- Gaia Collaboration et al., 2023b, *A&A*, 674, A1, *Gaia Data Release 3. Summary of the content and survey properties*
- Glass I. S., Evans T. L., 1981, *Nature*, 291, 303, *A period-luminosity relation for Mira variables in the Large Magellanic Cloud*
- Graham M. J., et al., 2015a, *nat*, 518, 74, *A possible close supermassive black-hole binary in a quasar with optical periodicity*
- Graham M. J., et al., 2015b, *Nature*, 518, 74, *A possible close supermassive black-hole binary in a quasar with optical periodicity*
- Graham M. J., et al., 2019, *PASP*, 131, 078001, *The Zwicky Transient Facility: Science Objectives*
- Greene K. L., Cyr-Racine F.-Y., 2022, *J. Cosmology Astropart. Phys.*, 2022, 002, *Hubble distancing: focusing on distance measurements in cosmology*
- Gribbin J., 1992, *Astronomy Now*, 6, 37, *Focus: cosmic distance ladder. Introduction.*
- Groenewegen, M. A. T. Blommaert, J. A. D. L. 2005, *A&A*, 443, 143, *Mira variables in the ogle bulge fields*
- Gunn J. E., et al., 1998, *AJ*, 116, 3040, *The Sloan Digital Sky Survey Photometric Camera*
- Guo H., Liu X., Shen Y., Loeb A., Monroe T., Prochaska J. X., 2018, *Monthly Notices of the Royal Astronomical Society*, 482, 3288, *Constraining sub-parsec binary supermassive black holes in quasars with multi-epoch spectroscopy – III. Candidates from continued radial velocity tests*
- Hasselquist S., et al., 2021, *ApJ*, 923, 172, *APOGEE Chemical Abundance Patterns of the Massive Milky Way Satellites*
- Hinkle K. H., Lebzelter T., Joyce R. R., Fekel F. C., 2002, *AJ*, 123, 1002, *Velocity Observations of Multiple-Mode Asymptotic Giant Branch Variable Stars*
- Hodge J. A., Becker R. H., White R. L., Richards G. T., Zeimann G. R., 2011, *The Astronomical Journal*, 142, 3, *High-resolution very large array imaging of sloan digital sky survey stripe 82 at 1.4 ghz*
- Ilić D., Rakić N., Popović L. Č., 2023, *ApJS*, 267, 19, *Fantastic Fits with fantasy of Active Galactic Nuclei Spectra: Exploring the Fe II Emission near the H $\alpha$  Line*
- Ita Y., et al., 2004, *MNRAS*, 353, 705, *Variable stars in the Magellanic Clouds - II. The data and infrared properties*
- Ivezić Ž., et al., 2007, *The Astronomical Journal*, 134, 973, *Sloan digital sky survey standard star catalog for stripe 82: The dawn of industrial 1% optical photometry*
- Ivezić Ž., Connolly A. J., VanderPlas J. T., Gray A., 2014, *Statistics, Data Mining, and Machine Learning in Astronomy: A Practical Python Guide for the Analysis of Survey Data*, doi:10.1515/9781400848911.
- Iwanek P., et al., 2021, *The Astrophysical Journal Supplement Series*, 257, 23, *Multiwavelength properties of miras*
- Javadi A., van Loon J. T., Mirtorabi M. T., 2011, *MNRAS*, 411, 263, *The UK Infrared Telescope M33 monitoring project - I. Variable red giant stars in the central square kiloparsec*
- Jiang L., et al., 2014, *ApJS*, 213, 12, *The Sloan Digital Sky Survey Stripe 82 Imaging Data: Depth-optimized Co-adds over 300 deg<sup>2</sup> in Five Filters*
- Johnson M. A. C., Gandhi P., Chapman A. P., Moreau L., Charles P. A., Clarkson W. I., Hill A. B., 2018, *Monthly Notices of the Royal Astronomical Society*, 484, 19, *Prospecting for periods with LSST – low-mass X-ray binaries as a test case*
- Jordi C., et al., 2010a, *A&A*, 523, A48, *Gaia broad band photometry*
- Jordi C., et al., 2010b, *A&A*, 523, A48, *Gaia broad band photometry*
- Kaspi S., Smith P. S., Netzer H., Maoz D., Jannuzi B. T., Giveon U., 2000, *ApJ*, 533, 631, *Reverberation Measurements for 17 Quasars and the Size-Mass-Luminosity Relations in Active Galactic Nuclei*
- Kaspi S., Maoz D., Netzer H., Peterson B. M., Vestergaard M., Jannuzi B. T., 2005, *ApJ*, 629, 61, *The Relationship between Luminosity and Broad-Line Region Size in Active Galactic Nuclei*
- Kennicutt R. C., Evans N. J., 2012, *Annual Review of Astronomy and Astrophysics*, 50, 531, *Star formation in the milky way and nearby galaxies*

- Kim D.-C., Yoon I., Evans A. S., Kim M., Momjian E., Kim J. H., 2020, *The Astrophysical Journal*, 904, 23, *Dual agn candidates with double-peaked [o iii] lines matching that of confirmed dual agns*
- Kippenhahn R., Weigert A., Weiss A., 2013, *Stellar Structure and Evolution*, doi:10.1007/978-3-642-30304-3.
- Kollatschny Ochmann, M. W. Zetzl, M. Haas, M. Chelouche, D. Kaspi, S. Pozo Nuñez, F. Grupe, D. 2018, *A&A*, 619, A168, *Broad-line region structure and line profile variations in the changing look agn he 1136-2304*
- Kovačević A. B., Pérez-Hernández E., Popović L. C., Shapovalova A. I., Kollatschny W., Ilić D., 2018, *Monthly Notices of the Royal Astronomical Society*, 475, 2051, *Oscillatory patterns in the light curves of five long-term monitored type I active galactic nuclei*
- Kovačević A. B., Č Popović L., Simić S., Ilić D., 2019, *The Astrophysical Journal*, 871, 32, *The optical variability of supermassive black hole binary candidate pg 1302–102: Periodicity and perturbation in the light curve*
- Kovačević A. B., Popović L. C., Ilić D., 2020a, *Open Astronomy*, 29, 51, *Two-dimensional correlation analysis of periodicity in active galactic nuclei time series*
- Kovačević A. B., Yi T., Dai X., Yang X., Čvorović Hajdinjak I., Popović L. C., 2020b, *Monthly Notices of the Royal Astronomical Society*, 494, 4069, *Confirmed short periodic variability of subparsec supermassive binary black hole candidate Mrk 231*
- Krolik J. H., Horne K., Kallman T. R., Malkan M. A., Edelson R. A., Kriss G. A., 1991, *ApJ*, 371, 541, *Ultraviolet Variability of NGC 5548: Dynamics of the Continuum Production Region and Geometry of the Broad-Line Region*
- Kudryavtseva N. A., et al., 2011, *A&A*, 526, A51, *A possible jet precession in the periodic quasar B0605-085*
- Labrie K., Anderson K., Cárdenes R., Simpson C., Turner J. E. H., 2019, in Teuben P. J., Pound M. W., Thomas B. A., Warner E. M., eds, *Astronomical Society of the Pacific Conference Series Vol. 523, Astronomical Data Analysis Software and Systems XXVII*. p. 321
- Law N. M., et al., 2009, *PASP*, 121, 1395, *The Palomar Transient Factory: System Overview, Performance, and First Results*
- Leavitt H. S., 1908, *Annals of Harvard College Observatory*, 60, 87, *1777 variables in the Magellanic Clouds*
- Leavitt H. S., Pickering E. C., 1912, *Harvard College Observatory Circular*, 173, 1, *Periods of 25 Variable Stars in the Small Magellanic Cloud.*
- Lebzelter, T. Trabucchi, M. Mowlavi, N. Wood, P. R. Marigo, P. Pastorelli, G. Lecoœur-Taïbi, I. 2019, *A&A*, 631, A24, *Period-luminosity diagram of long period variables in the magellanic clouds - new aspects revealed from gaia data release 2*
- Lebzelter T., Mowlavi N., Marigo P., Pastorelli G., Trabucchi M., Wood P. R., Lecoœur-Taïbi I., 2018, *A&A*, 616, L13, *A new method to identify subclasses among AGB stars using Gaia and 2MASS photometry*
- Lebzelter T., Trabucchi M., Mowlavi N., Wood P. R., Marigo P., Pastorelli G., Lecoœur-Taïbi I., 2019, *A&A*, 631, A24, *Period-luminosity diagram of long period variables in the Magellanic Clouds. New aspects revealed from Gaia Data Release 2*
- Lewis K. T., Eracleous M., Storchi-Bergmann T., 2010, *ApJS*, 187, 416, *Long-term Profile Variability in Active Galactic Nucleus with Double-peaked Balmer Emission Lines*
- Li Y.-R., et al., 2016, *The Astrophysical Journal*, 822, 4, *Spectroscopic indication of a centi-parsec supermassive black hole binary in the galactic center of ngc5548*
- Li S., Riess A. G., Busch M. P., Casertano S., Macri L. M., Yuan W., 2021, *The Astrophysical Journal*, 920, 84, *A sub-2% distance to m31 from photometrically homogeneous near-infrared cepheid period–luminosity relations measured with the hubble space telescope*
- Lindgren, L. et al., 2021, *A&A*, 649, A2, *Gaia early data release 3 - the astrometric solution*
- Lira P., et al., 2018, *The Astrophysical Journal*, 865, 56, *Reverberation mapping of luminous quasars at high z*
- Liu T., Gezari S., 2018, in *American Astronomical Society Meeting Abstracts #231*. p. 105.02
- Liu F. K., Li S., Komossa S., 2014, *ApJ*, 786, 103, *A Milliparsec Supermassive Black Hole Binary Candidate in the Galaxy SDSS J120136.02+300305.5*
- Liu T., et al., 2019, *The Astrophysical Journal*, 884, 36, *Supermassive black hole binary candidates from the pan-starrs1 medium deep survey*

- Lomb N. R., 1976, *Ap&SS*, 39, 447, *Least-Squares Frequency Analysis of Unequally Spaced Data*
- Madore B. F., 1982, *ApJ*, 253, 575, *The period-luminosity relation. IV. Intrinsic relations and reddenings for the Large Magellanic Cloud Cepheids.*
- Mandel I., Levin Y., 2015, *ApJ*, 805, L4, *Double Tidal Disruptions in Galactic Nuclei*
- Maness H. L., Taylor G. B., Zavala R. T., Peck A. B., Pollack L. K., 2004, *ApJ*, 602, 123, *Breaking All the Rules: The Compact Symmetric Object 0402+379*
- Marscher A. P., Gear W. K., 1985, *ApJ*, 298, 114, *Models for high-frequency radio outbursts in extragalactic sources, with application to the early 1983 millimeter-to-infrared flare of 3C 273.*
- Massardi M., et al., 2011, *Monthly Notices of the Royal Astronomical Society*, 412, 318, *The Australia Telescope 20 GHz (AT20G) Survey: analysis of the extragalactic source sample*
- Merritt D., Milosavljević M., 2005, *Living Reviews in Relativity*, 8, 8, *Massive Black Hole Binary Evolution*
- Moca V. V., Bârzan H., Nagy-Dăbâcan A., Mureşan R. C., 2021, *Nature Communications*, 12, 337, *Time-frequency super-resolution with superlets*
- Molnár L., Joyce M., Kiss L. L., 2019, *The Astrophysical Journal*, 879, 62, *Stellar evolution in real time: Models consistent with the direct observation of a thermal pulse in *t ursae minoris**
- Mosser B., et al., 2013, *A&A*, 559, A137, *Period-luminosity relations in evolved red giants explained by solar-like oscillations*
- Mösta P., Ott C. D., Radice D., Roberts L. F., Schnetter E., Haas R., 2015, *Nature*, 528, 376, *A large-scale dynamo and magnetoturbulence in rapidly rotating core-collapse supernovae*
- Nenkova M., Sirocky M. M., Ivezić Ž., Elitzur M., 2008, *ApJ*, 685, 147, *AGN Dusty Tori. I. Handling of Clumpy Media*
- Netzer H., 2015, *ARA&A*, 53, 365, *Revisiting the Unified Model of Active Galactic Nuclei*
- Palaversa L., et al., 2013, *AJ*, 146, 101, *Exploring the Variable Sky with LINEAR. III. Classification of Periodic Light Curves*
- Peterson B. M., 1997, *An Introduction to Active Galactic Nuclei*
- Peterson B. M., 2014, *Space Sci. Rev.*, 183, 253, *Measuring the Masses of Supermassive Black Holes*
- Popović L. Č., 2020, *Open Astronomy*, 29, 1, *Broad spectral lines in AGNs and supermassive black hole mass measurements*
- Popovic L. C., Vince I., Atanackovic-Vukmanovic O., Kubiceła A., 1995, *A&A*, 293, 309, *Contribution of gravitational redshift to spectral line profiles of Seyfert galaxies and quasars.*
- Popović L. Č., Kovačević-Dojčinović J., Marčeta-Mandić S., 2019, *MNRAS*, 484, 3180, *The structure of the Mg II broad line emitting region in Type I AGNs*
- Popović L. Č., Simić S., Kovačević A., Ilić D., 2021, *mnras*, 505, 5192, *Detecting subparsec supermassive binary black holes: Long-term monitoring perspective*
- Popović L. Č., et al., 2023, *A&A*, 675, A178, *Long-term optical spectral monitoring of a changing-look active galactic nucleus NGC 3516. II. Broad-line profile variability*
- Popović L. C., 2012, *New Astronomy Reviews*, 56, 74, *Super-massive binary black holes and emission lines in active galactic nuclei*
- Popović L. C., Kovačević-Dojčinović J., Marčeta-Mandić S., 2019, *Monthly Notices of the Royal Astronomical Society*, 484, 3180, *The structure of the Mg II broad line emitting region in Type I AGNs*
- Press W. H., Rybicki G. B., 1989, *ApJ*, 338, 277, *Fast Algorithm for Spectral Analysis of Unevenly Sampled Data*
- Prochaska J. X., et al., 2020a, *pypeit/PypeIt: Release 1.0.0*, Zenodo, doi:10.5281/zenodo.3743493
- Prochaska J. X., et al., 2020b, *Journal of Open Source Software*, 5, 2308, *Pypeit: The python spectroscopic data reduction pipeline*
- Riess A. G., et al., 2022, *ApJ*, 934, L7, *A Comprehensive Measurement of the Local Value of the Hubble Constant with  $1 \text{ km s}^{-1} \text{ Mpc}^{-1}$  Uncertainty from the Hubble Space Telescope and the SH0ES Team*
- Ripepi V., Molinaro R., Musella I., Marconi M., Leccia S., Eyer L., 2019, *A&A*, 625, A14, *Reclassification of Cepheids in the Gaia Data Release 2. Period-luminosity and period-Wesenheit relations in the Gaia passbands*



- Ripepi V., et al., 2023, *A&A*, 674, A17, *Gaia Data Release 3. Specific processing and validation of all sky RR Lyrae and Cepheid stars: The Cepheid sample*
- Runnoe J. C., et al., 2015, *The Astrophysical Journal Supplement Series*, 221, 7, *A large systematic search for close supermassive binary and rapidly recoiling black holes. ii. continued spectroscopic monitoring and optical flux variability*
- Runnoe J. C., et al., 2017, *MNRAS*, 468, 1683, *A large systematic search for close supermassive binary and rapidly recoiling black holes - III. Radial velocity variations*
- Saio H., Wood P. R., Takayama M., Ita Y., 2015, *MNRAS*, 452, 3863, *Oscillatory convective modes in red giants: a possible explanation of the long secondary periods*
- Sakamoto T., Matsunaga N., Hasegawa T., Nakada Y., 2012, in Aoki W., Ishigaki M., Suda T., Tsujimoto T., Arimoto N., eds, *Astronomical Society of the Pacific Conference Series Vol. 458, Galactic Archaeology: Near-Field Cosmology and the Formation of the Milky Way*. p. 245
- Samus N. N., Kazarovets E. V., Durlevich O. V., Kireeva N. N., Pastukhova E. N., 2017, *Astronomy Reports*, 61, 80, *General catalogue of variable stars: Version GCVS 5.1*
- Sanders J. L., 2023, *Monthly Notices of the Royal Astronomical Society*, 523, 2369, *The period–luminosity relation for Mira variables in the Milky Way using Gaia DR3: a further distance anchor for H0*
- Scargle J. D., 1982, *ApJ*, 263, 835, *Studies in astronomical time series analysis. II. Statistical aspects of spectral analysis of unevenly spaced data.*
- Schmidt M., 1963, *Nature*, 197, 1040, *3c 273: A star-like object with large red-shift*
- Sesar B., et al., 2007, *AJ*, 134, 2236, *Exploring the Variable Sky with the Sloan Digital Sky Survey*
- Seyfert C. K., 1943, *ApJ*, 97, 28, *Nuclear Emission in Spiral Nebulae.*
- Shankar F., et al., 2019, *MNRAS*, 485, 1278, *Black hole scaling relations of active and quiescent galaxies: Addressing selection effects and constraining virial factors*
- Shapovalova A. I., et al., 2016, *The Astrophysical Journal Supplement Series*, 222, 25, *First long-term optical spectral monitoring of a binary black hole candidate e1821+643. i. variability of spectral lines and continuum*
- Skrutskie M. F., et al., 2006, *AJ*, 131, 1163, *The Two Micron All Sky Survey (2MASS)*
- Soszyński I., et al., 2005, *Acta Astron.*, 55, 331, *The Optical Gravitational Lensing Experiment. Miras and Semiregular Variables in the Large Magellanic Cloud*
- Soszynski I., et al., 2009a, *Acta Astronomica*, 59, *The optical gravitational lensing experiment. the ogle-iii catalog of variable stars. iv. long-period variables in the large magellanic cloud*
- Soszyński I., et al., 2009b, *Acta Astron.*, 59, 239, *The Optical Gravitational Lensing Experiment. The OGLE-III Catalog of Variable Stars. IV. Long-Period Variables in the Large Magellanic Cloud*
- Soszyński I., et al., 2010, *Acta Astron.*, 60, 17, *The Optical Gravitational Lensing Experiment. The OGLE-III Catalog of Variable Stars. VII. Classical Cepheids in the Small Magellanic Cloud*
- Soszyński I., et al., 2011, *Acta Astron.*, 61, 217, *The Optical Gravitational Lensing Experiment. The OGLE-III Catalog of Variable Stars. XIII. Long-Period Variables in the Small Magellanic Cloud*
- Soszyński I., et al., 2013, *Acta Astron.*, 63, 21, *The Optical Gravitational Lensing Experiment. The OGLE-III Catalog of Variable Stars. XV. Long-Period Variables in the Galactic Bulge*
- Stokes G. H., Evans J. B., Vighh H. E. M., Shelly F. C., Pearce E. C., 2000, *Icarus*, 148, 21, *Lincoln Near-Earth Asteroid Program (LINEAR)*
- Sun Y., Zhang J., Zhang B., Xu S., Mai X., Ding H., Chen W., Wen S., 2023, *Frontiers in Astronomy and Space Sciences*, 10, *Miras as a distance indicator in the csst, jwst, and gaia era*
- Tabur V., Bedding T. R., Kiss L. L., Giles T., Derekas A., Moon T. T., 2010, *Monthly Notices of the Royal Astronomical Society*, 409, 777, *Period–luminosity relations of pulsating M giants in the solar neighbourhood and the Magellanic Clouds*
- Thanjavur K., Ivezić Ž., Allam S. S., Tucker D. L., Smith J. A., Gwyn S., 2021, *MNRAS*, 505, 5941, *Photometric cross-calibration of the SDSS Stripe 82 Standard Stars catalogue with Gaia EDR3, and comparison with Pan-STARRS1, DES, CFIS, and GALEX catalogues*

- Trahin B., Breuval L., Kervella P., Mérand A., Nardetto N., Gallenne A., Hocdé V., Gieren W., 2021, *A&A*, 656, A102, *Inspecting the Cepheid parallax of pulsation using Gaia EDR3 parallaxes. Projection factor and period-luminosity and period-radius relations*
- Tremaine S., Davis S. W., 2014, *MNRAS*, 441, 1408, *Dynamics of warped accretion discs*
- Udalski A., 2003, *Acta Astron.*, 53, 291, *The Optical Gravitational Lensing Experiment. Real Time Data Analysis Systems in the OGLE-III Survey*
- Udalski A., Kubiak M., Szymanski M., 1997, *Acta Astron.*, 47, 319, *Optical Gravitational Lensing Experiment. OGLE-2 – the Second Phase of the OGLE Project*
- Urry C., Padovani P., 1995, *Publications of the Astronomical Society of the Pacific*, 107, 803, *Unified schemes for radio-loud active galactic nuclei*
- Valtonen M. J., et al., 2008, *Nature*, 452, 851, *A massive binary black-hole system in OJ287 and a test of general relativity*
- VanderPlas J. T., 2018, *The Astrophysical Journal Supplement Series*, 236, 16, *Understanding the lomb–scargle periodogram*
- VanderPlas J. T., Željko Ivezić 2015, *The Astrophysical Journal*, 812, 18, *Periodograms for multiband astronomical time series*
- Verde L., Treu T., Riess A. G., 2019, *Nature Astronomy*, 3, 891, *Tensions between the early and late Universe*
- Vestergaard M., Peterson B. M., 2006, *ApJ*, 641, 689, *Determining Central Black Hole Masses in Distant Active Galaxies and Quasars. II. Improved Optical and UV Scaling Relationships*
- Wambsganss J., Paczynski B., Schneider P., 1990, *ApJ*, 358, L33, *Interpretation of the Microlensing Event in QSO 2237+0305*
- Wang J.-M., Bon E., 2020, *A&A*, 643, L9, *Changing-look active galactic nuclei: close binaries of supermassive black holes in action*
- Wang J.-G., et al., 2009, *The Astrophysical Journal*, 707, 1334, *Estimating black hole masses in active galactic nuclei using the mg ii lambda 2800 emission line*
- Wiescher M., 2009, *Physics Online Journal*, 2, 69, *Cosmic alchemy in the laboratory*
- Woo J.-H., Le H. A. N., Karouzos M., Park D., Park D., Malkan M. A., Treu T., Bennert V. N., 2018, *The Astrophysical Journal*, 859, 138, *Calibration and limitations of the mg ii line-based black hole masses*
- Wood P. R., Nicholls C. P., 2009, *ApJ*, 707, 573, *Evidence for Mass Ejection Associated with Long Secondary Periods in Red Giants*
- Wood P. R., Sebo K. M., 1996a, *Monthly Notices of the Royal Astronomical Society*, 282, 958, *On the pulsation mode of Mira variables: evidence from the Large Magellanic Cloud*
- Wood P. R., Sebo K. M., 1996b, *MNRAS*, 282, 958, *On the pulsation mode of Mira variables: evidence from the Large Magellanic Cloud*
- Wood P. R., et al., 1999, in Le Bertre T., Lebre A., Waelkens C., eds, <series information> Vol. 191, *Asymptotic Giant Branch Stars*. p. 151
- Woosley S. E., Weaver T. A., 1986, *ARA&A*, 24, 205, *The physics of supernova explosions*.
- Wray J. J., Eyer L., Paczyński B., 2004, *MNRAS*, 349, 1059, *OGLE small-amplitude variables in the Galactic bar*
- Xin C., Haiman Z., 2021, *MNRAS*, 506, 2408, *Ultra-short-period massive black hole binary candidates in LSST as LISA 'verification binaries'*
- Yoachim P., et al., 2023, *lsst/rubin\_sim: v1.3.1*, doi:10.5281/zenodo.8388546, <https://doi.org/10.5281/zenodo.8388546>
- Yuan W., He S., Macri L. M., Long J., Huang J. Z., 2017a, *AJ*, 153, 170, *The M33 Synoptic Stellar Survey. II. Mira Variables*
- Yuan W., Macri L. M., He S., Huang J. Z., Kanbur S. M., Ngeow C.-C., 2017b, *The Astronomical Journal*, 154, 149, *Large magellanic cloud near-infrared synoptic survey. v. period–luminosity relations of miras*
- Yuan W., Macri L. M., Javadi A., Lin Z., Huang J. Z., 2018a, *AJ*, 156, 112, *Near-infrared Mira Period-Luminosity Relations in M33*

- Yuan W., Macri L. M., Javadi A., Lin Z., Huang J. Z., 2018b, *The Astronomical Journal*, 156, 112, *Near-infrared mira period–luminosity relations in m33*
- de Grijs R., Courbin F., Martínez-Vázquez C. E., Monelli M., Oguri M., Suyu S. H., 2017, *Space Sci. Rev.*, 212, 1743, *Toward an Internally Consistent Astronomical Distance Scale*

# Curriculum vitae

Marta Fatović was born on August 19, 1995, in Zadar, Croatia. She obtained her Master's degree in Physics in 2019 from the Faculty of Science, University of Zagreb, under Prof. Amon Ilakovac, focusing on renormalization group equations and amplitudes at the two-loop level.

During her studies, Marta worked on building a Scanning Tunneling Microscope at the University of Zagreb and studied the Large Magellanic Cloud at the Ruđer Bošković Institute. She attended the Petnica Summer Institute for courses in Cosmology and High Energy Physics.

In 2019, Marta began her PhD in Astrophysics at the University of Zagreb, under the supervision of Dr. Lovro Palaversa, focusing on variable sources in large optical sky surveys. Since 2020, she has been a research associate at the Ruđer Bošković Institute, working in the Laboratory for Astroparticle Physics and Astrophysics. She is involved in the Gaia and LSST collaborations.

Marta's international experience includes training at Hawaii's Gemini Observatory (2022) and research at the University of Belgrade (2023). She has presented at conferences like the European Astronomical Society Annual Meetings, Young Scientist Festival, and Transient Sky with Gaia. Marta has also served on Local Organizing Committees, including for LSST @Europe 5 in 2023.

Marta is active in outreach, writing for "Hunting for the Cosmic Beasts" on social media as astroMarta, and participating in open days at the Institute for Physics and Ruđer Bošković Institute. She is a member of the Croatian Astronomical Society and a former member of the Croatian Physical Society. Marta received a City of Zadar scholarship from 2014 to 2019. She has authored seven papers, including one as the first author, with another paper in preparation where she is also the first author.